STUDIES OF CHARGE ACCUMULATION IN THE KATRIN MAIN SPECTROMETER

Kevin J. Wierman

A dissertation submitted to the faculty of the University of North Carolina at Chapel Hill in partial fulfillment of the requirements for the degree of Doctor of Philosophy in the Department of Physics and Astronomy.

Chapel Hill
2016

Approved by:

John Wilkerson

Reyco Henning

Joaquín Drut

Gerald Cecil

Christian Iliadis

ABSTRACT

Kevin J. Wierman: Studies of Charge Accumulation In The KATRIN Main Spectrometer.
(Under the direction of John Wilkerson.)

Experiments in recent years have shown neutrinos have non-zero rest mass. The Karlsruhe Tritium Neutrino experiment (KATRIN) will directly probe the electron anti-neutrino mass using tritium beta decay. KATRIN's main spectrometer aims to provide a 0.2 eV sensitivity to the neutrino mass, an order of magnitude improvement over the previous generation of experiments. During KATRIN's most recent commissioning phase, a mono-energetic electron source was used to probe transmission properties and study associated potential systematic errors in the main spectrometer. Charge accumulation from this source is identified as a potential source for systematic error and the impact on the neutrino mass measurement is estimated.

ACKNOWLEDGMENTS

Funding provided by the DOE Office of Science under grant numbers: # DE-FG02-97ER41020/A000, # DE-FG02-97ER41041 and # DE-FG02-97ER41033.

TABLE OF CONTENTS

List of Figures . . . . . **xi**

List of Tables . . . . . **xii**

List of Abbreviations and Symbols . . . . . **xiii**

1 Neutrino Mass **1**

1.1 Current Description 1

1.1.1 Dirac Description 2

1.1.2 The Standard Model 2

1.1.3 Oscillation Experiments 3

1.1.4 Majorana Neutrinos 5

1.2 Neutrino Mass Measurements 6

1.2.1 Cosmological Measurements 6

1.3 Neutrinoless Double Beta Decay 7

1.4 Kinematic Neutrino Mass 8

1.4.1 Tritium Beta Decay Measurements 9

1.4.2 Other Direct Neutrino Mass Measurements 12

1.5 Impact of Neutrino Mass Measurements 13

2 Magnetic Adiabatic Collimation and Electrostatic Filtering **15**

2.1 Introduction 15

2.2 Methodology 15

2.3 Resolution 17

2.4 Transmission Function 18

2.5 Angular Acceptance 19

2.6 Design 20

2.7 Charge Trapping in MAC-E Experiments 20

2.8 Introducing a Dipole Field . . . 22
2.8.1 Regular Motion without the Dipole Electrode . . . 23
2.8.2 Motion With a Dipole Electrode . . . 26
2.8.3 Trap Emptying by Dipole Electrode . . . 28
2.9 Application . . . 29

3 KATRIN . . . 30
3.1 Experimental Goal . . . 30
3.2 Apparatus . . . 30
3.2.1 Windowless Gaseous Tritium Source . . . 31
3.2.2 Differential And Cryogenic Pumping Sections . . . 32
3.2.3 Spectrometers . . . 33
3.2.4 Detector . . . 35
3.2.5 Detector Wafer and Electronics . . . 37
3.2.6 Data Acquisition Electronics . . . 38
3.2.7 Cosmic Ray Veto . . . 41

4 Spectrometer and Detector Section Commissioning . . . 43
4.1 Goals . . . 43
4.2 Commissioning Apparatus . . . 44
4.2.1 The Electron Gun . . . 44
4.2.2 Method of Measuring Transmission Functions . . . 48
4.3 EGun Evaluation . . . 49
4.4 KATRIN Software . . . 50
4.4.1 Geometry . . . 50
4.4.2 KEMField . . . 52
4.4.3 Kassiopeia . . . 53
4.4.4 Preliminary Simulation Results . . . 54
4.5 EGun Simulation Applications . . . 54

5 Charge Accumulation . . . 56
5.1 Initial Indications of Charge Accumulation . . . 56
5.2 Analytic Model of Hysteresis in Transmission Function . . . 58

5.2.1 Dipole Electrode Effect . . . 62
5.2.2 Analytic Model Evaluation . . . 64
5.3 Measurement of Charge Accumulation . . . 69
5.3.1 Method . . . 69
5.3.2 Rate Acquisition . . . 70
5.3.3 Measured Transmission Function . . . 73
5.3.4 Residual Rate Calculation . . . 74
5.3.5 Fitting Rate Excess . . . 75
5.4 Simulation of Trapped Particles . . . 78
5.4.1 Simulation Construction . . . 79
5.4.2 Results of Simulations . . . 81
5.5 Comparison of Simulations and Analysis Results . . . 86
5.6 Dipole Electrode Model Analysis . . . 89
5.7 Null Hypothesis Testing . . . 90
5.8 Neutrino Mass Impact . . . 91

6 Conclusion . . . 94
6.1 Summary of Results . . . 94
6.1.1 Dipole Electrode Model . . . 94
6.1.2 Electron Gun Simulation . . . 94
6.1.3 Charge Accumulation Model . . . 95
6.1.4 Neutrino Mass Impact . . . 95
6.2 Moving Forward . . . 95
6.3 Outlook . . . 96

Appendix A Thorough Derivation of MAC-E filtering . . . 97

Appendix B Correlation Checking the Data against Slow Controls Values . . . 102
B.1 Correlation Searches . . . 102
B.1.1 Binning . . . 102
B.1.2 Correlation Strategies . . . 102
B.1.3 Correlation Testing . . . 103
B.1.4 Testing Algorithm . . . 104

B.1.5 Correlation Difference 104

Appendix C The FPD Cosmic Ray Veto 108

Bibliography 122

LIST OF FIGURES

1.1 Neutrino mass hierarchy 5

1.2 Tritium beta decay spectrum 9

1.3 Tritium final state modification energies 11

1.4 Neutrino mass impact 13

2.1 Design of a MAC-E filter 17

2.2 Transmission function for an isotropic and monoenergetic source of electrons 19

2.3 A simplified Penning Trap 21

2.4 Electron motion with dipole shift 23

2.5 Simple cyclotron motion 25

2.6 Cyclotron motion with magnetron drift 27

3.1 The KATRIN apparatus 31

3.2 The windowless gaseous tritium source 32

3.3 The cryogenic and differential pumping systems 33

3.4 The prespectrometer 34

3.5 The KATRIN main spectrometer 35

3.6 The KATRIN focal plane detector 36

3.7 The assembled KATRIN detector system 37

3.8 The effect of the KATRIN post acceleration electrode 38

3.9 The KATRIN detector wafer 39

3.10 The detector feedthrough flange 39

3.11 The detector front-end electronics 40

3.12 ORCA readout of the KATRIN detector 41

3.13 FPD Signal through the Mark IV trapezoidal filter 42

3.14 Example data collection at detector 42

4.1 The SDS commissioning apparatus 43

4.2 Schematic of the commissioning electron gun 44

4.3 External views of the commissioning electron gun 45

4.4 The interior of the electron gun . . . 46
4.5 The EGun photoelectric surface . . . 47
4.6 EGun high voltage schematic . . . 47
4.7 Example transmission function measurement . . . 49
4.8 Simulated main spectrometer . . . 50
4.9 Simulated EGun geometry . . . 51
4.10 EGun electrostatic potential map . . . 52
4.11 Particle tracks in the EGun . . . 53
4.12 Example simulated transmission function . . . 54
5.1 Hysteresis in the transmission function . . . 57
5.2 Simulated dipole geometry . . . 58
5.3 KATRIN commissioning potential map . . . 59
5.4 Maximum transmission angle as a function of initial energy . . . 60
5.5 Trapping probability as a function of position . . . 61
5.6 Analytic transmission function with charge accumulation . . . 65
5.7 Analytic transmission function excess . . . 66
5.8 Mean rate impact on electron rate excess fits . . . 67
5.9 Energy distribution impact on excess fits . . . 68
5.10 Region of interest adjustment . . . 72
5.11 Region of interest adjustment . . . 73
5.12 Measured transmission function . . . 74
5.13 Dipole measurement residuals . . . 75
5.14 Individual Measured Transmission Function Residuals . . . 76
5.15 Dipole measurement residual fits . . . 77
5.16 Initial Distributions of electrons in simulation . . . 79
5.17 Simulated number of trapped electrons . . . 81
5.18 Simulated dipole effect on transmission function . . . 82
5.19 Simulated transmission function with charge accumulation . . . 83
5.20 Simulated transmission function residuals with charge accumulation . . . 84

5.21 Individual Simulated Transmission Function Residuals 85
5.22 EGun width broadening from dipole electrode 87
5.23 Event Lifetime as a function of dipole potential 88
5.24 Number of turns spent in the main spectrometer 89
5.25 Dipole reduction constant comparison 91
5.26 Neutrino mass impact 93
C.1 Schematic drawing of the KATRIN veto 108
C.2 The St. Gobain fibers used to read out the scintillator panels. 108
C.3 MPPCs 109
C.4 Veto panels 110
C.5 Fiber end closeup 111
C.6 Veto biasing electronics 112
C.7 New veto enclosure design 112
C.8 Assembled veto panels 113
C.9 MPPC sample output 114
C.10 Digitized veto signal 115
C.11 Veto digitization comparison 116
C.12 FPGA triggering rates for veto 117
C.13 Veto peak peak finding 118
C.14 Veto spectral stability 119
C.15 Veto hodoscope measurement 120
C.16 Veto efficiency plot 121

LIST OF TABLES

1.1 Results of oscillation experiments 4

1.2 Neutrino mass results from cosmology 6

1.3 Neutrino mass results from neutrinoless double beta decay. 8

1.4 Limits on neutrino mass from Tritium Beta Decay Experiments 10

4.1 Nominal Electrode Potentials 49

4.2 Measured EGun Properties 50

5.1 Run Numbers 70

5.2 Backplate Voltages Used in Study 71

5.3 Fit results for measured data 78

5.4 Fit results for simulated data 86

5.5 Dipole Effect on Transmission Width 87

6.1 Summary of KATRIN Systematics 96

B.1 Linear Correlation With Slow Controls parameters 105

B.2 Correlation Residuals 105

B.3 Correlation coefficients for background runs 106

C.1 Veto Panel Efficiencies 118

LIST OF ABBREVIATIONS AND SYMBOLS

ν_e, ν_μ, ν_τ	Neutrino Flavor Eigenstates
ν_1, ν_2, ν_3	Neutrino Mass Eigenstates
m_1, m_2, m_3	Neutrino Mass Eigenvalues
m_β	Kinematic Neutrino Mass
$m_{\beta\beta}$	Effective Majorana Mass
m_{cosm}	Cosmological Neutrino Mass
T	Transmission Ratio
U_0	Analyzing Potential
E_e	Electron Energy
θ_{pch}	Pitch Angle
B_S	Source Magnetic Field
B_A	Analyzing Magnetic Field
B_{min}	Minimum Magnetic Field
B_{max}	Maximum Magnetic Field
KATRIN	Karlsruhe Tritium Neutrino Mass Experiment
MAC-E	Magnetic Adiabatic Collimation and Electrostatic filtering
WGTS	Windowless Gaseous Tritium Source
DPS	Differential Pumping System
CPS	Cryogenic Pumping System
FPD	Focal Plane Detector
SDS	Spectrometer and Detector Systems
EGun	Electron Gun
TF	Transmission Function
ROI	Region of Interest
HV	High Voltage
kcps	kilo counts per second

CHAPTER 1: NEUTRINO MASS

The goal of this dissertation is to aid the measurement of the mass of the electron anti-neutrino. This chapter discusses the physics of neutrino mass and absolute mass measurements.

1.1 Current Description

One of the most abundant particles in the universe, the neutrino, is the focus of a field of study with broad impacts across physics. In cosmology, neutrinos parameterize mass density in the epoch immediately following the Big Bang. Astrophysics utilizes neutrinos to describe nuclear reactions in solar models and observations of supernovae neutrinos are used in nuclear astrophysics to describe core collapse. Nuclear and particle physics experimentally probes the origins of mass with neutrino observations to improve the Standard Model of particle physics. However, several properties of neutrinos described in this chapter have not yet been measured and their measurement will provide insights to the fields impacted by neutrinos.

The existence of neutrinos was postulated due to the continuity of the beta decay energy spectrum and the associated spin statistics [1]. In beta decay, a continuous electron energy spectra implies that a third particle must participate in the interaction [2]. Equation 1.1.1, represents the decay from a parent nucleus, ${}^{A}_{Z}X$ to the child nucleus, ${}^{A}_{Z+1}X$, and an electron, e^{-}, and this third body, $\overline{\nu}_{\mathrm{e}}$, the *electron anti-neutrino*.

$$ {}^{A}_{Z}X \rightarrow {}^{A}_{Z+1}X + e^{-} + \overline{\nu}_{\mathrm{e}} \tag{1.1.1} $$

From the process in Equation 1.1.1, one can infer that to conserve angular momentum and electronic charge, neutrinos must be charge neutral fermions. In addition, similar to other charged fermions, neutrinos come in three interaction flavors. In this case, these are electron neutrinos (ν_{e}), muon neutrinos (ν_{μ}), and tau neutrinos (ν_{τ}) [3–5]. We now know that this process (and the inverse process) are explained by the weak interaction [6, 7]. Currently this interaction is the only known process by which neutrinos are created or consumed. The eigenstates for this process correspond to the interaction flavors mentioned above and their anti-particle states.

1.1.1 Dirac Description

In the Dirac description of particle physics, fermions are described by four components; particle and anti-particle states and two spin projections. These four component *spinors* obey the Dirac equation in Equation 1.1.2. In this equation, the particle wavefunction, ψ is operated on by the 4-gradient, $\partial\!\!\!/$, which mixes spin projections, and the scalar mass term, m, which does not mix spin projections. A particle whose wavefunction obeys the Dirac equation must then have both spin projections or be massless. Therefore, if neutrinos are massive and if neutrinos are described by the Dirac equation, then neutrinos must exist in both spin projections or *helicities*.

$$(i\partial\!\!\!/ - m)\psi = 0 \tag{1.1.2}$$

However, neutrinos are observed to be produced only in a single helicity. Polarized beta decay experiments have shown that electrons produced in beta decay can only be produced with spin in the same direction as their momenta, or positive helicity [8, 9]. Due to angular momentum conservation, neutrinos are then only produced with negative helicity, and anti-neutrinos with positive helicity. This also shows that weak interactions are parity violating.

1.1.2 The Standard Model

The standard model of particle physics describes fundamental interactions as gauge bosons and the participating particles as fermionic fields[7]. As weak interactions are parity violating, an alternative description known as *chirality* is used to describe particle field operators. Here, the chirality of a particle is analogous to the helicity and in fact is identical for massless particles. Like with helicity, neutrinos only appear in chirality with left-handed particle states and right-handed anti-particle states.

In the standard model, particles are initially required to be massless to guarantee gauge invariance. The Higgs mechanism necessitates additional terms in the Lagrangian which include particle mass [7]. In this mechanism, fermion masses show up as the vacuum expectation value, v of the Higgs doublet, ϕ_0. This doublet is included in the Yukawa coupling terms of the standard model Lagrangian. For the case of neutrinos, the Yukawa term of the Lagrangian density for electrons is shown in Equation 1.1.3 where the Higgs doublet couples to the left handed fermion doublet, (ν_{eL}, e_L) and right handed singlet, (e_R). The constants are absorbed into c_e.

$$\mathscr{L}_{yuk} = -c_e \left[\bar{e}_R \phi_0^\dagger \begin{pmatrix} \nu_{eL} \\ \\ e_L \end{pmatrix} + (\bar{\nu}_{eL}, \bar{e}_L)\phi_0 e_R \right] \tag{1.1.3}$$

$$\phi_0 = \frac{1}{\sqrt{2}} \begin{pmatrix} 0 \\ \\ v \end{pmatrix} \tag{1.1.4}$$

From this description, the mass of electrons is generated. However, for neutrinos, mass is required to be zero due to the right handed singlet terms having no neutrino term with which to couple. This is a result of requiring both handed-states to couple to the Higgs doublet, but as only one handed-ness is observed, the mass term is zero.

1.1.3 Oscillation Experiments

Neutrinos have been shown to have non-zero masses due to the phenomena known as *neutrino oscillations*. Suppose that the neutrino flavors from Section 1.1.1 are not singularly associated to their mass eigenstates, ν_1, ν_2, ν_3 with eigenvalues m_1, m_2, m_3. Instead, a rotation, $U_{\alpha,i}$ forms a general relation between the flavor and mass states as shown in Equation 1.1.5.

$$\nu_\alpha = \sum_i U_{\alpha,i} \nu_i \tag{1.1.5}$$

This formalism can be inserted into the propagator for particles in vacuum to calculate the probability of detecting a neutrino in state ν_α that was originally produced in state ν_β. This is detailed in Equation 1.1.6 where t is time, $\delta_{\alpha\beta}$ is the Dirac delta, L is length from source, and E is the initial energy of the particles. The mass squared difference, Δm^2_{ij} is the difference in mass eigenvalues, m_i and m_j squared. Thus, a non-zero mass squared difference and off-diagonal elements in the mixing matrix require at least one massive eigenstate.

$$P(\nu_\alpha \to \nu_\beta) = \left| \langle \nu_\beta | \nu_\alpha(t) \rangle \right|^2 = \left| \delta_{\alpha\beta} + \sum_{i \neq j} U_{\beta i} e^{-\frac{i \Delta m^2_{ij} L}{2E}} U^*_{\alpha j} \right|^2 \tag{1.1.6}$$

Experimentally, the mixing matrix is probed by observing the flux of neutrinos from solar sources, atmospheric sources, reactors and accelerators. At different energies and length scales, this allows the mixing matrix to be broken into pieces as in Equation 1.1.7. The mass eigenstate differences are

sensitive to energies where $\Delta m^2_{ij} L/2E \approx \pm 1$, and so it is useful to utilize subscripts which indicate the source of the neutrinos instead of the mass eigenstate indices.

In Equation 1.1.7, the parameters, δ, α_1, and α_2 parameterize the probability of *CP phase violation*. This occurs when the probability of a particle oscillating into a flavor is not identical to the anti-particle case. This violates the symmetry of the C and P operators. The charge conjugate operator, C transforms a particle state into an anti-particle state and the parity operator P performs a spatial inversion of one ordinate. For the case of the terms denoted, *Majorana* in Equation 1.1.7, these require that neutrinos are their own antiparticle and will be discussed in Section 1.1.4.

The current results of oscillation experiments are detailed in Table 1.1.3. Current efforts are being made to improve measurements of these results [10–12]. Since the mass difference squared values are observed to be non-zero, one deduces that neutrinos are massive. In addition, by setting the lightest mass eigenstate to zero, one may set a lower limit on the neutrino masses using the mass squared differences.

$$U = \underbrace{\begin{pmatrix} 1 & 0 & 0 \\ 0 & c_{23} & s_{23} \\ 0 & -s_{23} & c_{23} \end{pmatrix}}_{(Solar)} \underbrace{\begin{pmatrix} c_{13} & 0 & s_{13}e^{-i\delta} \\ 0 & 1 & 0 \\ -s_{13}e^{i\delta} & 0 & c_{13} \end{pmatrix}}_{(Reactor)} \underbrace{\begin{pmatrix} c_{12} & s_{12} & 0 \\ -s_{12} & c_{12} & 0 \\ 0 & 0 & 1 \end{pmatrix}}_{(Atmospheric)} \underbrace{\begin{pmatrix} e^{i\alpha_1} & 0 & 0 \\ 0 & e^{i\alpha_2} & 0 \\ 0 & 0 & 1 \end{pmatrix}}_{(Majorana)} \tag{1.1.7}$$

Parameter	best fit($\pm 1\sigma$)	3σ
$\Delta m^2_{solar}[10^{-5} eV^2]$	$7.58^{+0.22}_{-0.26}$	$6.99 - 8.18$
$\Delta m^2_{atm}[10^{-3} eV^2]$	$2.35^{+0.12}_{-0.09}$	$2.06 - 2.67$
$\sin^2\theta_{12}$	$0.306(0.312)^{+0.018}_{-0.015}$	$0.259(0.265) - 0.359(0.364)$
$\sin^2\theta_{23}$	$0.42^{+0.08}_{-0.03}$	$0.34 - 0.64$
$\sin^2\theta_{13}$	$0.021(0.025)^{+0.007}_{-0.008}$	$0.001(0.015) - 0.044(0.036)$

Table 1.1: Results of oscillation experiments. These recent findings were summarized by the Particle Data Group in Table 14.7 [13].

While these experiments show neutrino mass exists, the mass term in Equation 1.1.6 is only sensitive to mass squared differences. The sign of the difference can be found by using matter effects [14]. Currently, this is done for atmospheric neutrinos and solar neutrino measurements are underway. This allows for two possible mass eigenstate orderings or *hierarchies*, as illustrated in Figure 1.1.

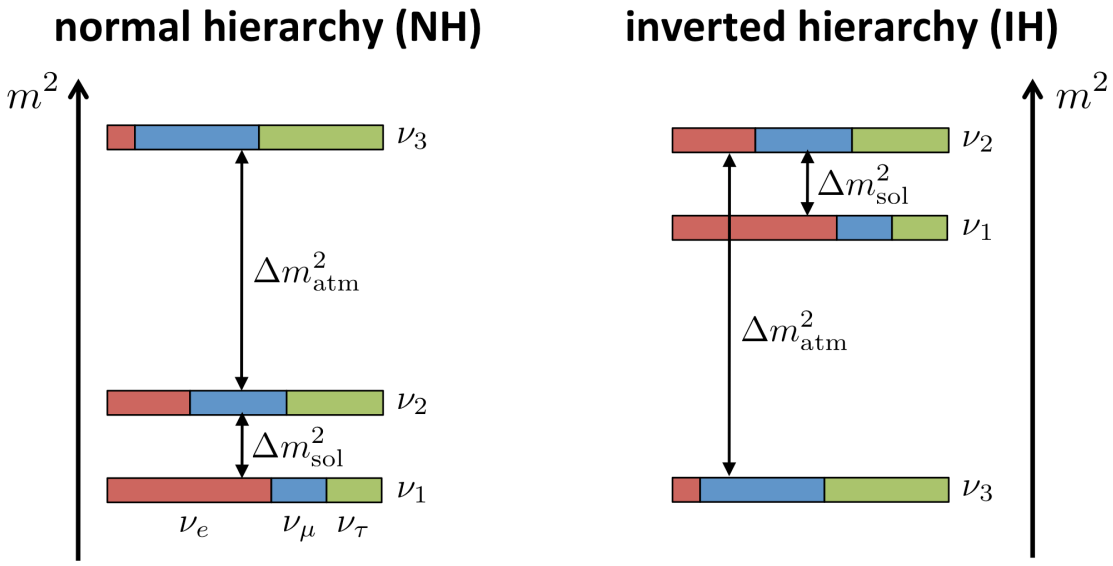

Figure 1.1: The possible hierarchies of neutrino masses and the associated flavor mixing in each flavor eigenstate. Image sourced from: [15].

Massive neutrinos show that the description used in the standard model is either incomplete or incorrect.

1.1.4 Majorana Neutrinos

An alternative to the Dirac description of particles is the Majorana description [16]. In comparison to the Dirac equation, the Majorana equation as shown in Equation 1.1.8 shows no distinction between particles and anti-particles and their associated helicities. Instead, this equation now mixes the particle states with their charge conjugates, ψ_c.

$$i\partial\!\!\!/\psi_c + m\psi = 0 \tag{1.1.8}$$

As neutrinos are charge neutral, they are candidates for being used in the Majorana equation [16]. In this description, neutrinos and anti-neutrinos would be the same particle with different handedness. The Majorana equation therefore provides an alternative description for neutrinos, which may be used to amend the standard model to account for neutrino mass. However, this requires that neutrinos are their own anti-particle. This will be discussed in further detail in Section 1.3.

1.2 Neutrino Mass Measurements

In addition to neutrino oscillation experiments, several different techniques can be used to probe neutrino mass. These include cosmological measurements, neutrinoless double beta decay and single beta decay kinematics measurements. The measurements provide complimentary information on neutrino mass and the other remaining unmeasured neutrino parameters.

1.2.1 Cosmological Measurements

In analogy to the standard model of subatomic physics, ΛCDM, or dark energy, the λ model with cold dark matter, CDM, is the analytical model against which to compare cosmological observations [17]. This model describes the evolution of the universe starting from a hot dense state to today's universe. Observables in this model include large scale structures and anisotropies in the cosmic microwave background[18].

The ΛCDM model predicts a relic neutrino background distributed throughout the universe. These neutrinos originate from electroweak freeze out just after the big bang, and therefore their expected energy should be in the region of the Q-value for neutron decay, namely in the sub-meV region. While this low threshold makes relic neutrinos difficult to impossible to detect, the connection between neutrinos and ΛCDM makes neutrino mass a parameter in the model. The energy density of neutrinos, Ω_ν can be compared to the energy density of the universe as a whole, Ω_{tot} and can be computed as

$$\Omega_\nu = \frac{\sum_i m_i}{93.14\, h^3 eV/c^2} \tag{1.2.1}$$

Where h is the dimensionless Hubble parameter[19].

For comparison, a 2 eV neutrino mass here results in a fractional energy density comparable to that of baryonic matter. Measuring this parameter is achieved by fitting a number of parameters to cosmological data sets. Recently the Planck collaboration has released an analysis which is shown in Table 1.2.

Upper Limit	Confidence Limit
$m_i < 0.230\, eV/c^2$	95%

Table 1.2: Neutrino mass results from cosmology. Result sources from: [18].

This limit was achieved by combing data sets from Planck with data sets from the Wilkinson Microwave Anisotropy Probe and gravitational lensing. As this limit on neutrino mass is acquired

by fitting the data to the ΛCDM model, this represents a model dependent measurement. In addition, multiple correlated fit parameters are used in the fits. Therefore, if a separate neutrino mass measurement is performed, then these models can be constrained by neutrino mass rather than utilizing it as a fit parameter.

1.3 Neutrinoless Double Beta Decay

Observations of neutrinoless double beta decay can provide another means of obtaining a neutrino mass measurement. Two neutrino double beta decay is a rare process in which two beta decays simultaneously occur, and is found in nuclei where normal beta decay is energetically forbidden[20]. This process is characterized in Equation 1.3.1 where the nucleus decays to the daughter nucleus plus two electrons and neutrinos.

$$ {}^{A}_{Z}X \rightarrow {}^{A}_{Z+2}X + 2e^{-} + 2\overline{\nu}_{e} \tag{1.3.1} $$

If neutrinos can be described by the Majorana equation in Section1.1.4, then it is possible that instead of emitting two neutrinos, none are emitted as in Equation 1.3.2. While multiple processes can explain the internal mechanism for this decay, the simplest model involves the exchange of a virtual Majorana neutrino between nucleons [21]. Since the weak interaction requires emission in one helicity and absorption in another, the spin of the virtual neutrino must flip.

$$ {}^{A}_{Z}X \rightarrow {}^{A}_{Z+2}X + 2e^{-} \tag{1.3.2} $$

Neutrino mass in neutrinoless double beta decay is related to the probability of this change of helicity. The half life of this process is effected by the virtual Majorana neutrino exchange. This is related to an effective "Majorana mass" of neutrinos, $\langle m_{\beta\beta} \rangle$ in Equation 1.3.3. The mass term, $\langle m_{\beta\beta} \rangle^2$ is expressed in terms of fundamental quantities in Equation 1.3.4. This also depends on the phase factor for two electrons, $G_{0\nu}$, the weak coupling constant, g_A and the transition matrix element, $M^{(0\nu)}$.

$$ \left(T^{0\nu}_{1/2}\right)^{-1} = G_{0\nu} g_A^4 \left| M^{(0\nu)} \right|^2 \langle m_{\beta\beta} \rangle^2 \tag{1.3.3} $$

$$ \langle m_{\beta\beta} \rangle^2 = \left| \sum_i U_{ei}^2 m_i \right|^2 \tag{1.3.4} $$

Currently, several experiments are utilizing neutrinoless double beta decay for neutrino mass. Notably among these, EXO-200 [22], Gerda [23], Kamland-Zen [24] have set upper limits on the effective Majorana mass detailed in Table 1.3. This limit is valid only if neutrinos can be described by the Majorana equation. If neutrinos are Dirac particles, then no such sensitivity can be obtained. Therefore, the measurement of the effective Majorana mass is dependent on the Majorana neutrino model.

Upper Limit	Confidence Limit
$\langle m_{\beta\beta} \rangle < 0.2 - 0.4\, eV/c^2$	95%

Table 1.3: Neutrino mass results from neutrinoless double beta decay.

Measuring the neutrino mass in this method provides additional information on the Majorana vs Dirac nature of the neutrino. However, this method is limited by uncertainties in the weak coupling constant and the choice of nucleus and therefore nuclear matrix element[25]. This can be complimented by a direct measurement of the neutrino mass which has no dependency on these values.

1.4 Kinematic Neutrino Mass

Of the methods for measuring neutrino mass, using the kinematics of beta decay is the most direct and is model independent. Following the Fermi theory of beta decay, the rate of electrons produced with energy E and momentum p is given by Equation 1.4.1 [26].

$$\frac{dN}{dE} = C|M|^2 F(Z,E) p(E+m_e)(Q_0-E) \sum_j U_{ej} \sqrt{(Q_0-E)^2 - m_j^2}\, \Theta(Q_0-E-m_\beta) \tag{1.4.1}$$

$$C = \frac{G_F^2 m_e^5}{2\pi^3} cos^2(\theta_C) \tag{1.4.2}$$

$$\sum_j U_{je} \sqrt{(Q_0-E)^2 - m_j^2} \approx \sqrt{(Q_0-E)^2 - m_\beta^2} \tag{1.4.3}$$

$$m_\beta^2 = \sum_i |U_{je}|^2 |m_j|^2 \tag{1.4.4}$$

Here, the endpoint energy, Q_0 is the maximum electron energy corresponding to a massless neutrino model. The Heaviside step function, Θ, ensures conservation of energy. The leading coefficient, C contains G_F, the Fermi constant, θ_C, the Cabibbo angle, and m_e, the electron mass. Nuclear wavefunction overlap is included in the nuclear matrix element, M. The Fermi function term, $F(Z,E)$, takes into account radiative corrections to the electron energy spectrum.

Equations 1.4.3 and 1.4.4 show an approximation commonly used in the context of neutrino mass. Currently, the experimental sensitivity to term is insufficient to determine the mass eigenstates, m_j. Therefore, the sum over the PMNS matrix terms are absorbed into the square root to form the term, m_β, sometimes referred to as the kinematic neutrino mass.

As none of these values in Equation 1.4.1 are model dependent and this observation relies on no assumptions regarding neutrinos, this is a direct method to determine neutrino mass. Commonly this is referred to as *absolute neutrino mass*.

Neutrino mass is measured by fitting the shape of the observed electron energy spectrum to Equation 1.4.1. The energy spectrum is most sensitive to neutrino mass in the region where $E \approx Q_0 - m_\beta$. It is therefore desirable to utilize a beta emitter with a low Q-value. The common experimental method is to then observe the electron energy spectrum coming from beta decay and fit the endpoint region spectral shape to the neutrino mass in Equation 1.4.4.

1.4.1 Tritium Beta Decay Measurements

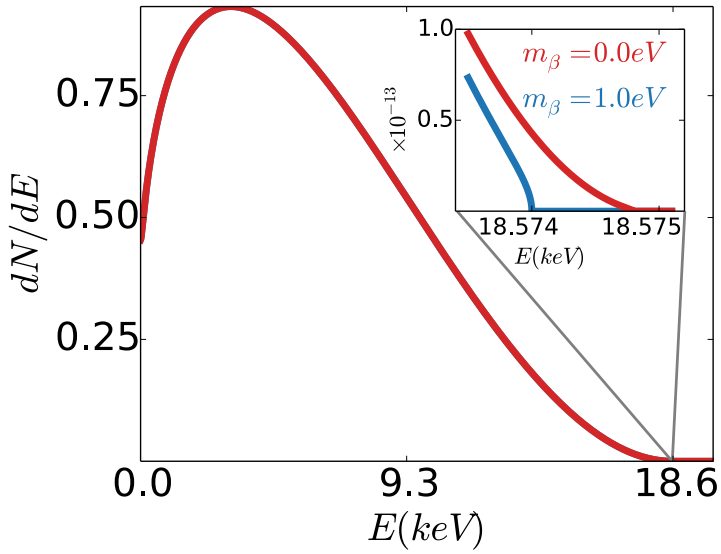

Figure 1.2: Tritium beta decay spectral shape for atomic tritium without final state effects. The embedded plot is the spectrum near the endpoint region. The red and blue lines show the spectral shape with a 0.0 eV and a 1.0 eV neutrino mass, respectively.

Tritium is a commonly used source in kinematic neutrino mass measurements. This is due to tritium's low endpoint energy (18.6 keV), super-allowed decay, simple nuclear properties and simple atomic structure. Equation 1.4.5 shows the decay process for tritium. Currently, the best limits on neutrino mass have been set by the tritium beta decay experiments[27, 28] as detailed in Table 1.4.1.

$$T \rightarrow {}^3He + e^- + \bar{\nu}_e + Q_0 \tag{1.4.5}$$

Using the current best limits on neutrino mass to set the region of interest, the number of electrons in the 2 eV range below the endpoint account for 1 in 10^{13} electrons emitted in beta decay. Figure 1.2 shows the expected spectral shape for this case. The inset figure shows the portion of the spectrum with sensitivity to a 1 eV neutrino mass, and thus illustrates the need to utilize as many electrons as possible without modifying the spectral shape. A high precision experiment therefore needs good resolution in this region, low backgrounds and high acceptance for electrons produced by a highly luminous source.

Experiment	Result	C.L.
Mainz[28]	2.3 eV	95%
Troitsk[27]	2.2 eV	95%

Table 1.4: Limits on neutrino mass from Tritium Beta Decay Experiments

The next generation of neutrino mass experiments will need to incorporate the previously mentioned requirements if the sensitivity to neutrino mass is to be increased. In addition, potential systematic errors which effect a lower neutrino mass sensitivity must be addressed.

Final States in Tritium Beta Decay

A potential systematic error in the neutrino mass measurement arises in the energy lost due to atomic and molecular final states of the decay source.

Using molecular tritium as a decay source is the most sensitive technique to probe the neutrino mass via the beta decay spectrum. This is due to the well understood and minimal systematic errors from scattering in the source itself [26]. One modification of the spectrum that must be accounted for is associated with the excitations formed in the daughter molecule of the decay.

Molecular tritium, T_2 decays according to Equation 1.4.6, where the daughter molecule, ${}^3HeT^+$, can be an excited state. Excitations arise from rotational and vibrational modes of the bound molecular state and electronic excitations in the molecular ion [30, 31].

$$T_2 \rightarrow {}^3 HeT^+ + e^- + \overline{\nu}_e + Q_0 \tag{1.4.6}$$

The tritium spectrum endpoint region is modified by the energy lost to excitations. Equation 1.4.7 shows the modified spectrum where the energy lost, E_i occurs with branching ratio, w_i.

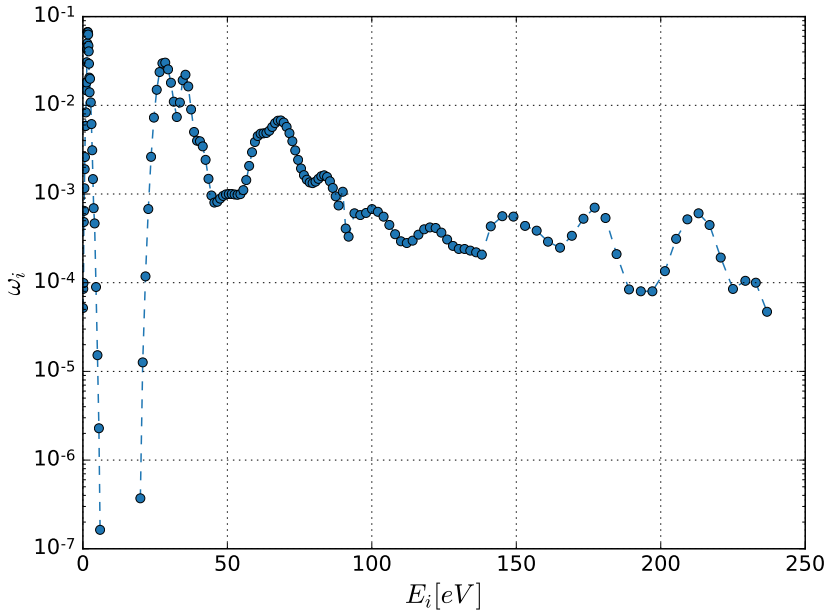

Figure 1.3: Tritium final state energy distribution. The x axis shows the energy lost in each final state branch which occurs with probability w_i. Data sourced from [29].

In contrast to the unmodified spectrum in Equation 1.4.1, each branching ratio modifies the spectral shape similar to produce a systematic error if left unaccounted for.

$$\frac{dN}{dE} = C|M|^2 F(Z,E) p(E+m_e) \sum_{i,j} w_i (Q_0 - E_i - E) U_{ej} \sqrt{(Q_0 - E_i - E)^2 - m_j^2}\, \Theta(Q_0 - E_i - E - m_\beta) \tag{1.4.7}$$

These effects are currently being measured to a higher precision by the TRIMS experiment at the University of Washington [32]. Figure 1.3 shows the distribution of energies which are clearly dominated by the electronic states in the region $> 10\,eV$. Not shown in this plot are the nuclear final state distributions that are from impurities in the source. Naturally occurring tritiated hydrogen isotopologues, DT and HT have reduced masses and therefore different excitation spectra. Before the next generation of tritium neutrino mass experiments move forward, each of these spectra will be quantitatively analyzed by the TRIMS experiment.

The neutrino mass sensitivity can be limited by the systematic uncertainty quantified by these measurements. For instance, a 1% uncertainty in the width of the distribution of molecular final states would correspond to a standard deviation on the order of $10^{-3}\ eV^2$ in the measurement of the square of the neutrino mass. Therefore, moving forward requires knowledge of the final state distribution once the sensitivity to the neutrino mass reaches this level.

1.4.2 Other Direct Neutrino Mass Measurements

In addition to the neutrino mass measurement that is the focus of this thesis, several other measurements aim to make a directly probe the kinematic neutrino mass.

Project 8

Cyclotron radiation emission spectroscopy is the method of measuring the power of the radiation produced by electrons undergoing cyclotron motion in strong magnetic fields. The Project 8 collaboration[33] is utilizing this concept to obtain a neutrino mass measurement from tritium placed in high magnetic fields. The cyclotron radiation emitted by these electrons is described in Equation 1.4.8 where the frequency, ω is a related to the kinetic energy, E_e through the Lorentz factor, γ.

$$\omega = \frac{eB}{\gamma m_e} = \frac{\omega_c}{1 + E_e/(m_e c^2)} \tag{1.4.8}$$

Measuring the cyclotron frequency is a non-destructive measurement and therefore allows the electrons to be used with other detectors for gating purposes. At a 1 T magnetic field, the Q-value of the tritium spectrum produces a 26 GHz signal. Radiofrequency waveguides placed around the volume pick up the radiation whose power is modified by the Larmor formula in Equation 1.4.9.

$$P(\beta, \theta) \propto \frac{2}{3} \frac{q^2 \omega_c^2 p_\perp^2}{m_e^2 c^3} \tag{1.4.9}$$

Higher power signals are favorable due to increasing the signal to noise ratio. By design, those with high pitch angle provide a higher measurement time and will be easiest to detect.

Project 8 presents another measurement of the neutrino mass which can be used to test KATRIN's findings. Multiple measurements are favorable in order to compare systematic uncertainties.

Electron Capture

Currently the other popular measurement method in direct neutrino mass determination is electron capture on ^{163}Ho. The kinematics of electron capture are nearly identical to that of beta decay with the notable exception that the energy is modified by excitations in the daughter nucleus. This is shown in Equation 1.4.10 where the excitations are modeled as Bright-Wigner peaks at energy E_i, width, Γ_i and weighting factor C_i[34, 35].

$$\frac{dN}{dE} = C|M|^2 F(Z,E) p(E+m_e)(Q_0-E)\sqrt{(Q_0-E)^2-m_\beta^2}\sum_i C_i \frac{\Gamma_i}{2\pi((E-E_i)+\Gamma_i^2/4)} \quad (1.4.10)$$

This calculation is made in the sudden approximation of the overlap of the two electron wave functions of holmium and the captured electron and multi-hole dysprosium excitation states. Currently, excitations with up to 3 electron holes have been calculated using the Dirac-Hartree-Fock method. However, higher order calculations have been shown to be necessary for neutrino mass determination. In addition, the measurements of the Q-Value of this process do not agree well. Future measurements will need to reconcile these differences.

1.5 Impact of Neutrino Mass Measurements

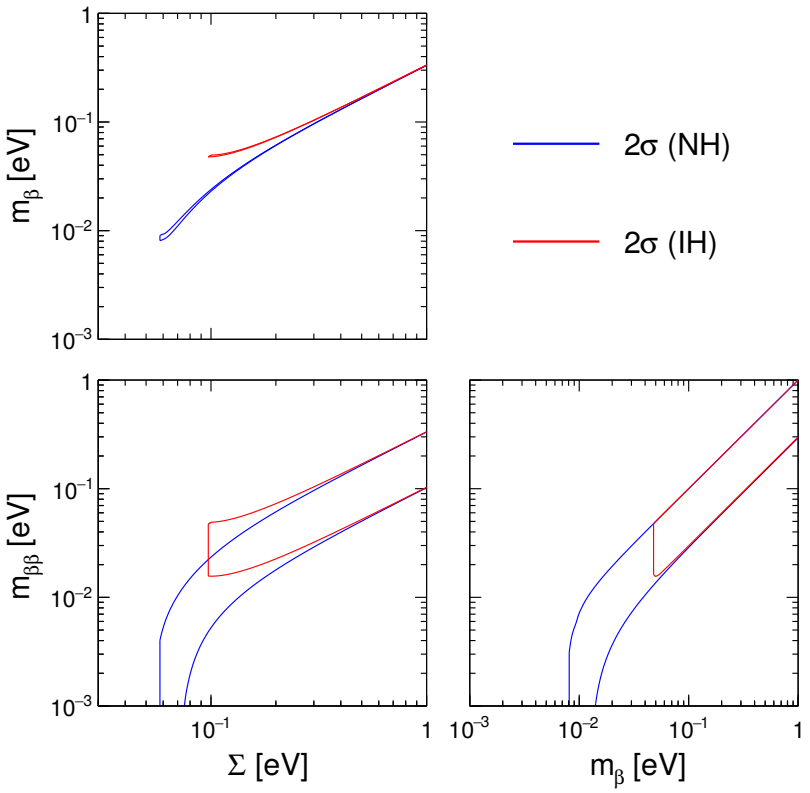

Figure 1.4: Possible neutrino mass solutions [36]. The exclusion regions are given by bounds from global fits using cosmological and oscillations data. The blue and red zones are dependent on the normal and inverted hierarchy respectively.

Given the information presented in previous sections, the unknowns in neutrino physics can be broken down into the following questions:

- What is the absolute scale of neutrino mass?
- Are neutrinos their own antiparticle?
- Why are neutrino masses much smaller than the mass of other fundamental particles?
- Which possible ordering applies itself to neutrino mass?

Absolute neutrino mass is related to the other unknowns in physics. Figure 1.4 shows the impact of each of the mass terms detailed above for both of the mass hierarchies allowed by neutrino oscillation experiments. For instance, one may rule out the inverted hierarchy if the absolute neutrino mass is low enough. The other open questions can be addressed similarly.

Whether or not neutrinos are their own anti-particle is determined by the observation of a neutrinoless double beta decay mode as shown in Section 1.1.4. Figure 1.4 shows that if neutrinos fall into the inverted hierarchy and kinematic neutrino mass is measured below the allowed range and neutrinoless double beta decay is not observed below the allowed range for the inverted hierarchy, then one may rule out the possibility of Majorana neutrinos.

This dissertation is focused on kinematic neutrino mass through tritium beta decay. The following chapter will discus the most sensitive experimental method for beta decay searches and the inherent systematic errors associated with this method.

CHAPTER 2: MAGNETIC ADIABATIC COLLIMATION AND ELECTROSTATIC FILTERING

This chapter discusses a spectrometer technology known as magnetic adiabatic collimation and electrostatic filtering. This technology is used in the measurement of the tritium spectrum endpoint region. The experimental focus of this thesis involves the usage of this method and particle trapping effects inherent to the apparatus.

2.1 Introduction

As discussed in Section 1.4.1, measuring the neutrino mass to sub-eV sensitivity requires obtaining the energy spectrum from tritium beta decay to high precision in the endpoint region. This level of precision requires:

- Low background in the endpoint region
- High angular acceptance from source
- A highly luminous source
- High resolving power in the endpoint region

These requirements are addressed by a technology known as magnetic adiabatic collimation and electrostatic (MAC-E) filtering. This was the technique used by the Mainz and Troitsk experiments to set the best direct limits on the electron anti-neutrino mass. While MAC-E filters were not originally created for the purpose of analyzing tritium beta decay[37], MAC-E filters have historically featured high acceptance and luminosity with high resolution [38].

2.2 Methodology

The basic framework of MAC-E filters is a series of superconducting solenoidial magnets producing magnetic field lines that connect the source to a detector. Electrons in a magnetic field undergo cyclotron motion due to the Lorentz force with a guiding center along the magnetic field line. In a cylindrically symmetrical system, up to half of the electrons produced in beta decay transmit toward the detector resulting in high acceptance.

With a magnetic field guiding electrons from source to detector, spectroscopy is performed by introducing an electrostatic potential normal to the magnetic field lines. The goal of using the electrostatic potential is to precisely reflect electrons below a set potential, U_0. From an isotropic source such as tritium, electrons are created with a range of pitch angles, θ_{pch} between their momenta and the magnetic field. The symmetry of the system allows the energy to be expressed as a sum of the perpendicular and longitudinal energies as follows, for an electron produced with energy, E_e and mass, m.

$$E_{\parallel} = \frac{(p * sin(\theta_{pch}))^2}{2m} \tag{2.2.1}$$

$$E_{\perp} = \frac{(p * cos(\theta_{pch}))^2}{2m} \tag{2.2.2}$$

$$E_e = E_{\parallel} + E_{\perp} \tag{2.2.3}$$

Therefore, the electrostatic potential will reflect electrons with energy with $E_{\parallel} < U_0$. As electrons with different pitch angles but identical longitudinal energy have different total energy, the spectrometer will filter electrons of different energies equally. Since the purpose of the spectrometer is filter electrons based on total energy, the filter width of the spectrometer is defined by this quality. Therefore, precision of the spectrometer is limited by the range of θ_{pch} electrons are allowed to take for a given total energy and allowed to transmit. Measuring the neutrino mass requires high acceptance and therefore collimation is not a viable option to differentiate between electrons of different pitch angles. However, re-aligning the electron momenta to the axis of symmetry would be a preferable method to increase sensitivity.

In order to collimate electrons from the source, the magnetic field is slowly relaxed from the maximum, B_{max} to a minimum, B_{min} where the electric potential is at it's maximum, as shown in Figure 2.2. In order to ensure adiabatic transfer and therefore minimize the loss in precision, the first adiabatic invariant in Equation 2.2.4 must be conserved along the electron trajectory. In this equation, γ is the relativistic Lorentz factor, and μ is the magnetic moment of the electron's cyclotron motion.

$$\gamma\mu = \frac{\gamma + 1}{2}\frac{E_{\perp}}{B} = \frac{\gamma + 1}{2}\frac{E_e - E_{\parallel}}{B} \tag{2.2.4}$$

A reduction in the magnetic field strength, B induces minimization of the perpendicular component of kinetic energy, $E_{\perp}$, and an increase in the parallel component, $E_{\parallel}$. In other words, the

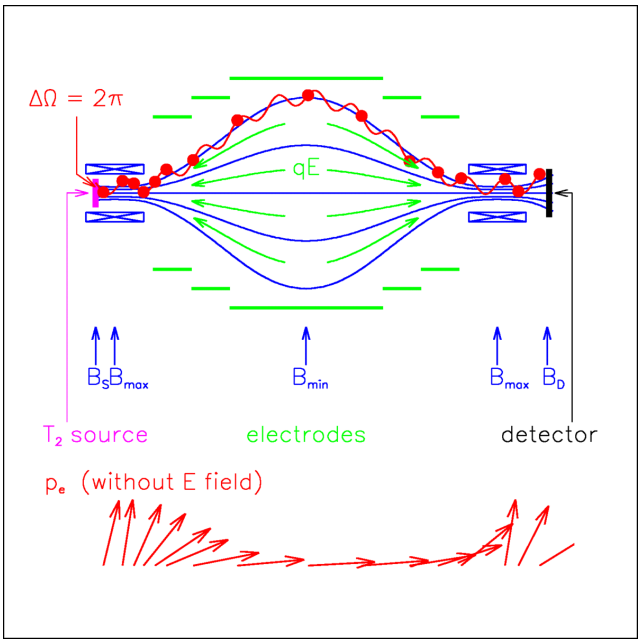

Figure 2.1: Design of the MAC-E apparatus and momentum transformation. Image sourced from [39].

relaxation of the magnetic field realigns the momentum to the axis of symmetry. With the electrostatic potential, U_0, applied at this magnetostatic minimum, the precision of the filter is increased. The plane of symmetry for the electrostatic field is known as the *analyzing plane* and is defined as the plane where electrons with energy $E_{\parallel} = U_0$ reflect.

2.3 Resolution

In general the momentum of an electron will not completely align with the beamline axis during collimation. To show how this is possible, consider two cases. In the first case, an electron is produced maximally aligned to the beamline, $E_{\perp} = 0$ with longitudinal energy $E_{\parallel} = E_e$. At the analyzing plane, this electron still has $E_{\parallel} = E_e$. For the second case, an electron is produced with longitudinal energy, $E_{\parallel} = (1 - \frac{B_{max}}{B_{min}})E_e$. Then, at the analyzing plane, the electron has longitudinal energy $E_{\parallel} = E_e$. For both cases, the electrons are filtered by an electrostatic potential, U_0 for energies $E_e < U_0$, and therefore to the spectrometer are identical. The latter case corresponds to an electron with $sin(\theta_{pch}) = \sqrt{B_{min}/B_{max}}$, the maximum angle for transmitting electrons. The adiabatic invariant for these two cases produces Equation 2.3.1.

$$\frac{E_e}{B_{max}} = \frac{\Delta E}{B_{min}} \tag{2.3.1}$$

Where B_{max} and B_{min} correspond to the maximum and minimum magnetic field strengths respectively. The energy difference, ΔE is the difference in total energy between the maximally aligned case and minimally aligned case. One can then express the resolution in terms of the magnetic fields as in Equation 2.3.2.

$$\frac{\Delta E}{E} = \frac{B_{min}}{B_{max}} \tag{2.3.2}$$

2.4 Transmission Function

While electrons with energy higher than the analyzing potential plus the resolution of the spectrometer will always transmit, and electrons below the analyzing potential always reflect, the situation where an electron is produced with energy within the resolution of the spectrometer is more complex. The description of the ratio of the number of electrons transmitting to the number of electrons produced at a given energy is referred to as the *transmission function* or $T(E)$.

Following the definition in Stefan Groh's thesis[40], the transmission function for an initial probability density function of electrons $f(\theta_{pch}, E_e)$ is computed as an integral over the allowed angles and energies. Equation 2.4.1 shows a simplified version of the transmission function which neglects relativistic effects for simplicity.. This is valid due to low Lorentz invariant in the Tritium decay region.

$$T(E, U_0) = \int_{U_0}^{\infty} \int_{0}^{\theta_{max}} f(\theta_{pch}, E_e) d\theta_{pch} dE_e \tag{2.4.1}$$

$$\theta_{max} = arcsin\left(\sqrt{(E_e - qU_0)/E_e \frac{B_{min}}{B_{max}}}\right) \tag{2.4.2}$$

The integral over the pitch angle is performed first due to the maximum allowed angular dependence on the initial energy of electrons. The maximum angle, θ_{max} is a function of the initial electron energy and relative field strengths.

For the simple case of a source distributed isotropically in the maximum magnetic field with Gaussian distributed energies, the resulting transmission function is shown in Equation 2.4.3. Appendix A shows the full calculation used to produce this. Graphically, this is displayed in Figure 2.2 where the transmission function has been shifted relative to the analyzing potential, U_0. The x-axis value, $E_e - U_0$, is known in the context of MAC-E filters as *electron excess energy.*

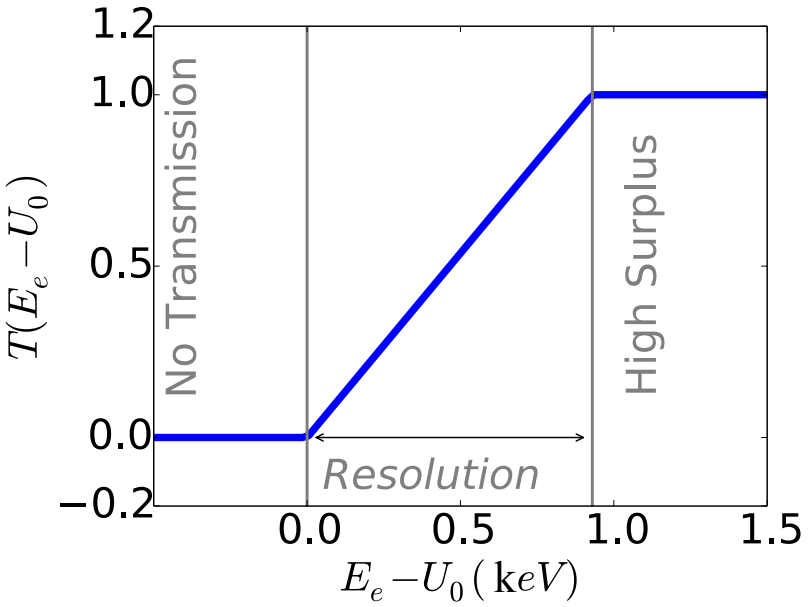

Figure 2.2: Transmission function for an isotropic and monoenergetic source of electrons

$$T(E) = \begin{cases} 0 & E \leq qU_0 \\ 1 - \sqrt{1 - \frac{E-qU}{E}\frac{B_{min}}{B_{max}}} & qU_0 \leq E \leq qU_0 \frac{B_{min}}{B_{max}} \\ 1 & qU_0 \frac{B_{min}}{B_{max}} \leq E \end{cases} \tag{2.4.3}$$

The transmission function is an observable that can be used to obtain the resolution of a spectrometer experimentally. For a monoenergetic source with isotropic angular distribution, the resolution as shown in Figure 2.2 is the width of the transmission function. More complex electron sources may also be used to probe the transmission function if the source spectral shape is known.

The basic workflow of using a MAC-E spectrometer is therefore to count the number of electron transmitting from a tritium source for a number of analyzing potentials. This measures an integrated spectrum where each point is the integral of the spectrum in Equation 1.4.5 from U_0 to the Q-value of the decay convolved with the transmission function.

2.5 Angular Acceptance

In general, the source of electrons is not required to be in the highest magnetic field strength. Due to technical limitations, the maximum field strength is determined by the design of the superconducting magnets. To increase luminosity and decrease scattering within the source itself,

ideally one would increase the radius at the source and the corresponding magnetic flux. However, the increase in magnetic field strength from source to magnet results in the magnetic reflection of electrons with high pitch angle.

Angular acceptance in MAC-E filters is determined by magnetic reflection. Rearranging Equation 2.2.4 in terms of the source magnetic field, B_{src} results in Equation 2.5.1. The critical angle, θ_c defines the maximum pitch angle with which electrons can be produced and not be magnetically reflected. Therefore, angular acceptance is defined by $\theta_{pch} < \theta_c$ for all azimuthal angles.

$$\frac{B_{src}}{B_{max}} = sin^2\theta_c \tag{2.5.1}$$

2.6 Design

Neutrino mass sensitivity in MAC-E filters is related through Monte Carlo simulation[41] to luminosity, background rate, measurement time and spectrometer resolution. Of these parameters, resolution is immutable to the apparatus.

As resolution increases with the ratio of field strengths, either the maximum field needs to be increased or the minimum decreased. Increasing the maximum field strength is problematic because technological limitations force the bore of the magnets to be smaller, decreasing luminosity[42]. Therefore, the minimum field strength must be decreased.

Since the adiabatic requirement must be met, the invariant in Equation 2.2.4 can be used to calculate the size of the spectrometer. The adiabatic invariant is linearly related to the magnetic flux through the helical orbit of electrons in cyclotron motion in Equation A.0.4. Therefore, to increase the resolution of a MAC-E spectrometer and therefore it's sensitivity to neutrino mass the radius of the spectrometer must also be increased.

2.7 Charge Trapping in MAC-E Experiments

In previous experiments utilizing MAC-E filter technology, a common issue has arisen with particles trapped in magnetic bottles and electrostatic minima [43–50]. Commonly, these areas of charge accumulation are referred to as Penning Traps[41, 51] (or Penning-Malmberg traps depending on the geometry), and a simplified drawing of one is given in Figure 2.7, whereby a strong magnetic field confines a particle radially and the electrostatic quadrupole confines the particle axially.

In MAC-E filters, Penning traps occur due to electrostatic and magnetostatic confinement. The two biggest sources of confinement are the analyzing potentials and any potential that is connected

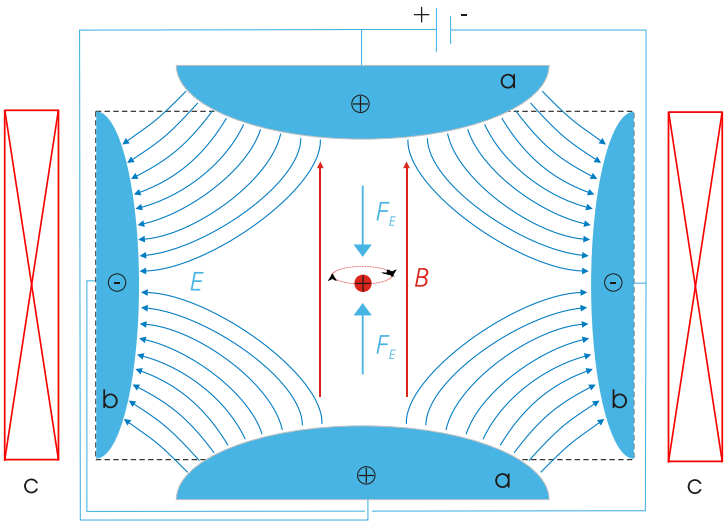

Figure 2.3: A simplified Penning Trap. The red boxes indicate the solonoid inducing the magnetic field. Blue electrodes are configured in an electrostatic quadropole. The particle depicted in the center experiences a confining axial electrostatic force and a radially confining cyclotron motion. Image sourced from: [52].

to the analyzing potential by a magnetic field line. If the electron produced at the source does not meet the requirement for transmission, then the electron is confined by the analyzing potential and the source potential. Therefore, the probability of trapping for charged sources is the same as reflection or,

$$P_{trap}(E) = 1 - T(E) \tag{2.7.1}$$

Where $T(E)$ is the transmission function for source at energy, E.

The consequences of Penning traps in these spectrometers are twofold.

1. Electrons exiting the trap may create unwanted background
2. If the field sourced by trapped electrons becomes competitive with the analyzing potential, then the electrons see a flat potential and all exit at once.

Penning traps can lead to the production of non-signal electrons due to signal electrons scattering off residual gas. The gas ionizes and is accelerated towards the detector. This rate has been measured in previous MAC-E Filters [41, 43].

The second item mentioned above is known as *Penning Discharge*. The number of electrons needed to start a discharge is identical to the number required to produce a spatial potential to compete with the existing applied potential. In other words, for a single test charges, the combined

fields of the surrounding electrons and confining potential must cancel. By definition, the electron density for the spatial confinement of charges where the applied electrostatic potential is equal to the average potential sourced by the charges themselves is [53],

$$\rho_{discharge} = 4\pi\epsilon_0 \frac{qU_{trap}}{a^2} \tag{2.7.2}$$

Where the trapping potential, U_{trap} and the characteristic distance, a are determined by the geometric constraints of the trap. Sources of electrons may be induced by field emission or spallation sources from cosmic rays.

Once the trap is full, then secondary ionization can create a catastrophic number of ions accelerated towards the detector. The maximum number of which can be calculated as in[54],

$$N_{max} = \rho_{discharge} 2^{\frac{qU_{trap}}{E_{ion}}} - 1 \tag{2.7.3}$$

Where the ionization energy is E_{ion}. This phenomenon is also known to be endemic to MAC-E filters. Due to the geometric scaling factor in the critical electron density, a higher resolution spectrometer is expected to induce larger Penning discharges.

2.8 Introducing a Dipole Field

Charged particles can be emptied from Penning traps utilizing a dipole electrode. In the past, an electrode that induces a dipole potential perpendicular to the beamline has been used to induce motion in the $\vec{E} \times \vec{B}$ direction [45, 55, 56]. Qualitatively, this motion has been understood to be a magnetron drift towards the outer radius of the beamline. Graphically, this is shown in Figure 2.4. To show exactly how this mechanism is expected to behave, the equations of motion will be derived below.

The Lorentz Equation in Einstein form defined for charge q, mass m and Lorentz factor γ, electrostatic field E_i, magnetic field, B_i and momentum p_i is,

$$\dot{p_i} = q(E_i + \frac{1}{\gamma m}\epsilon_{ijk} p_j B_k) \tag{2.8.1}$$

Where ϵ_{ijk} is the totally anti-symmetric tensor.

For the fields in consideration, the electric field can be described as,

$$\vec{E} = E_y\hat{y} + E_z\hat{z} \tag{2.8.2}$$

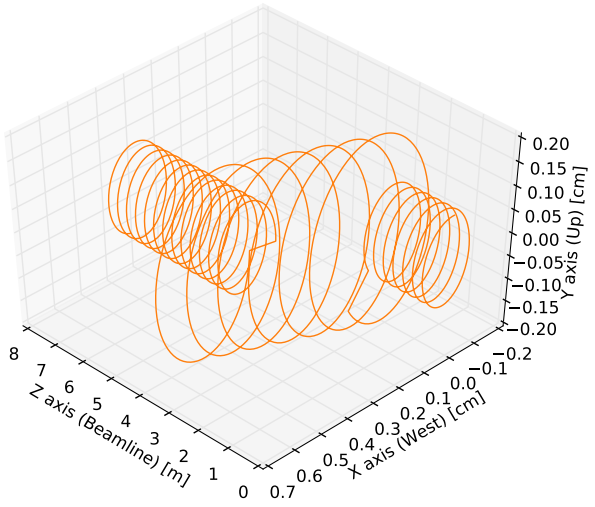

Figure 2.4: Electron motion with dipole shift. Electrons are initially placed in an electrostatic potential energy of $18.6keV$ with a minimum of $0keV$ located at $z = 0$. The electron initial kinetic energy is close to $0eV$ with a slight amount of transverse kinetic energy introduced to create motion. A magnetic field of $6T$ is applied to produce cyclotron motion. Between $z = 2$ and $z = 4$ a dipole field is applied to create the magnetron shift.

This equation describes the potential difference between the MAC-E potentials, E_z, plus the addition of the dipole electrode, E_y, using standard beamline coordinates.

For a simple uniform magnetic field in the direction of the beamline, one may express this field as,

$$\vec{B} = B_z \hat{z} \tag{2.8.3}$$

The approximation here is that the field is very strong and concentrated primarily in the beamline direction. In reality, there should also be a radial component, B_r.

2.8.1 Regular Motion without the Dipole Electrode

To derive the equations of motion, the simple case of cyclotron motion will be derived first. In the case of dynamics without the dipole electrode, the electric field reduces down to,

$$\vec{E} = E_z \hat{z} \tag{2.8.4}$$

In the beamline direction, the magnetic field component vanishes, leaving,

$$\dot{p_z} = qE_z \tag{2.8.5}$$

In the approximation that the electrostatic potential can be evaluated as periodic, then the axial dependence is the simple harmonic solution.

$$\dot{p_z} = q\nabla_z\Phi = q\nabla_z U_0 e^{-iz/d} \tag{2.8.6}$$

$$\ddot{z} = \frac{qU_0}{md^2}e^{-iz/d} \tag{2.8.7}$$

This would imply oscillation on the axis with periodicity of,

$$\omega_z = \sqrt{\frac{qU_0}{md^2}} \tag{2.8.8}$$

Similarly, in the transverse directions

$$\dot{p}_x = \frac{q}{\gamma m}p_y B_z \tag{2.8.9}$$

$$\dot{p}_y = -\frac{q}{\gamma m}p_x B_z \tag{2.8.10}$$

Taking the derivative with respect to time,

$$\ddot{p}_x = q\frac{1}{\gamma m}\dot{p}_y B_z = q\frac{1}{\gamma m}(-q\frac{1}{\gamma m}p_x B_z)B_z \tag{2.8.11}$$

$$\ddot{p}_y = -q\frac{1}{\gamma m}\dot{p}_x B_z = -q\frac{1}{\gamma m}\dot{(}q\frac{1}{\gamma m}p_y B_z)B_z \tag{2.8.12}$$

This implies a coupled oscillatory motion with eigenfrequency,

$$\omega_c = \frac{qB}{\gamma m} \tag{2.8.13}$$

Which, means the equations of motion in momentum space are:

$$p_x = p_x(0)cos(\omega_c t) + p_y(0)sin(\omega_c t) \tag{2.8.14}$$

$$p_y = p_y(0)cos(\omega_c t) - p_x(0)sin(\omega_c t) \tag{2.8.15}$$

Where the initial momentum in the transverse directions, $p_x(0)$ and $p_y(0)$ can also be expressed in terms of the pitch angle and initial azimuthal angle,

$$p_x = |p|cos(\theta_{pch})(cos(\phi_{azi})cos(\omega_c t) + sin(\phi_{azi})sin(\omega_c t)) \tag{2.8.16}$$

$$p_y = |p|cos(\theta_{pch})(cos(\phi_{azi})cos(\omega_c t) - sin(\phi_{azi})sin(\omega_c t)) \tag{2.8.17}$$

In position, space, this can also be expressed as,

$$x = \frac{|p|cos(\theta_{pch})}{m\omega_c}(cos(\phi_{azi})sin(\omega_c t) - sin(\phi_{azi})cos(\omega_c t)) + x_0 \tag{2.8.18}$$

$$y = \frac{|p|cos(\theta_{pch})}{m\omega_c}(cos(\phi_{azi})sin(\omega_c t) + sin(\phi_{azi})cos(\omega_c t)) + y_0 \tag{2.8.19}$$

$$z = z_0 e^{-i\omega_z t + \phi_z} \tag{2.8.20}$$

This motion is displayed in Figure 2.5 where the electron path is shown as a function of position. For the case of no dipole field, motion is just simple cyclotron motion with a confining field in the axial direction.

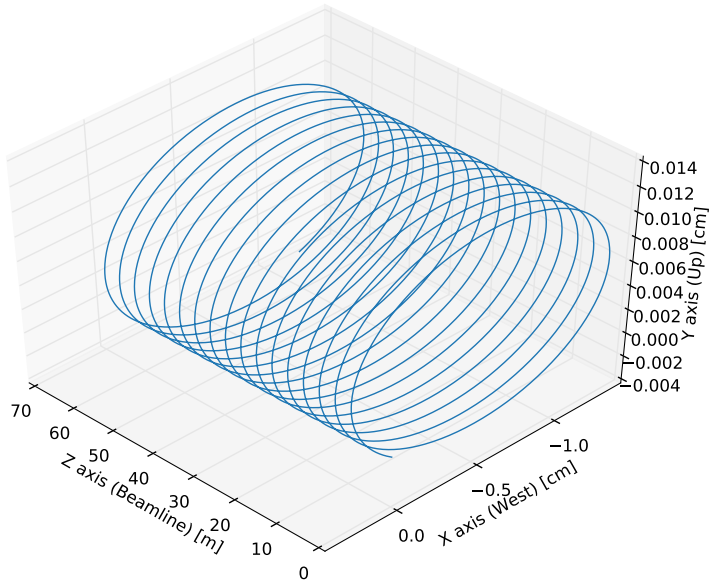

Figure 2.5: Simple Cyclotron Motion. The blue path is aligned to the beamline axis with sample parameters for the motion to create a 1cm radius.

From this derivation the Larmor radius is calculated as a consequence of the second order

equations of motion,

$$r_c^2 = (p_x^2(0) + p_y^2(0))/(m^2\omega_c^2) \tag{2.8.21}$$

2.8.2 Motion With a Dipole Electrode

The dipole field added together with the previous electric field can be expressed as,

$$\vec{E} = E_y\hat{y} + E_z\hat{z} \tag{2.8.22}$$

Obviously, this doesn't change the axial component, but modifies the coupled equations in the transverse directions,

$$\dot{p}_x = \frac{q}{\gamma m}p_y B_z \tag{2.8.23}$$

$$\dot{p}_y = E_y - \frac{q}{\gamma m}p_x B_z \tag{2.8.24}$$

Plugging the field values back in again,

$$\ddot{p}_x = q\frac{1}{\gamma m}(qE_y - q\frac{1}{\gamma m}p_x B_z)B_z \tag{2.8.25}$$

$$\ddot{p}_y = q\frac{1}{\gamma m}\dot{(}q\frac{1}{\gamma m}p_y B_z)B_z \tag{2.8.26}$$

This now describes coupled drift in the cyclotron center.

A more familiar description of this motion can be taken be reverting to the usual vector notation, and making use of null components to complete the cross products:

$$\ddot{\vec{p}} = \frac{q}{\gamma m}\vec{E}\times\vec{B} - \left(\frac{q}{\gamma m}\right)^2 \vec{p}\times\vec{B}\left|\vec{B}\right| \tag{2.8.27}$$

This describes a superposition of 2 motions in momentum space. The $\vec{p}\times\vec{B}$ term describes the usual cyclotron motion. The $\vec{E}\times\vec{B}$ term describes a constant drift in the $\hat{y}$ direction, and the

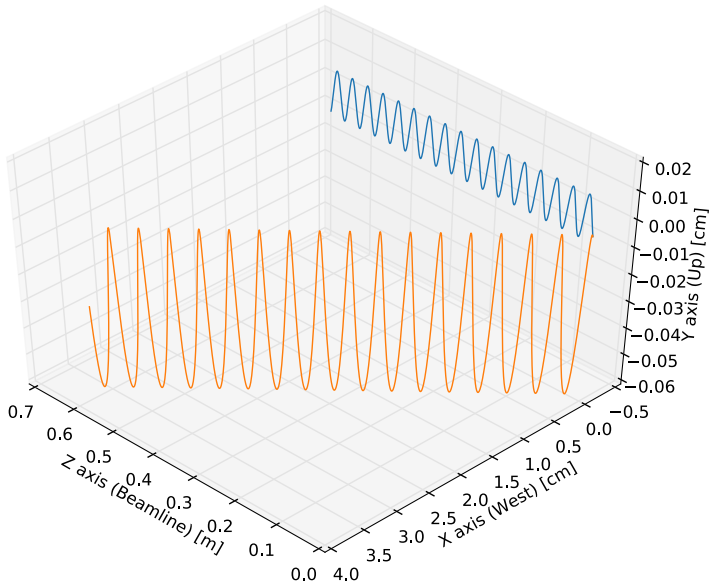

Figure 2.6: Simple Cyclotron Motion with magnetron drift added in. The blue track is the simple cyclotron motion. Orange is the dipole-induced magnetron motion with cyclotron motion.

corresponding coupling between the magnetic field and the momentum vector inducing work in the $\vec{E}\times\vec{B}$ direction, which in this case is the $\hat{x}$ direction. This is a separate motion that can be described as a drift of the center of motion in this direction.

The equations of motion in momentum space is therefore,

$$p_x = |p|cos(\theta_{pch})(cos(\phi_{azi})cos(\omega_c t) + sin(\phi_{azi})sin(\omega_c t)) + \frac{qE_d}{\gamma m B} \tag{2.8.28}$$

$$p_y = |p|cos(\theta_{pch})(cos(\phi_{azi})cos(\omega_c t) - sin(\phi_{azi})sin(\omega_c t)) \tag{2.8.29}$$

And likewise, in position space,

$$x = \frac{|p|cos(\theta_{pch})}{m\omega_c}(cos(\phi_{azi})sin(\omega_c t) - sin(\phi_{azi})cos(\omega_c t)) + x_0 + \frac{qE_d}{\gamma B}t \tag{2.8.30}$$

$$y = \frac{|p|cos(\theta_{pch})}{m\omega_c}(cos(\phi_{azi})sin(\omega_c t) + sin(\phi_{azi})cos(\omega_c t)) + y_0 \tag{2.8.31}$$

$$z = z_0 e^{-i\omega_z t + \phi_z} \tag{2.8.32}$$

Figure 2.6 displays this drift in orange and the original cyclotron motion in blue.

Using the above equation of motion, the change in energy can be described as,

$$\dot{E} = \int_z dz' \left[\frac{q}{\gamma m} |\vec{E} \times \vec{B}| - \left(\frac{q}{\gamma m} \right)^2 |\vec{p} \times \vec{B}| \left| \vec{B} \right| \right] \tag{2.8.33}$$

Or, for net energy gain or loss, this can be expressed as a double integral:

$$E = \int_t \int_z dz' dt' \left[\frac{q}{\gamma m} |\vec{E} \times \vec{B}| - \left(\frac{q}{\gamma m} \right)^2 |\vec{p} \times \vec{B}| \left| \vec{B} \right| \right] \tag{2.8.34}$$

Taking a calculus of variations approach, minor deviations in the integral along the beamline can be expressed as:

$$\delta_z E = \int_t \int_z dz' dt' \left[\frac{q}{\gamma m} \delta_z |\vec{E} \times \vec{B}| - \left(\frac{q}{\gamma m} \right)^2 \delta_z |\vec{p} \times \vec{B}| \left| \vec{B} \right| \right] \tag{2.8.35}$$

As there is no z-component in the $\vec{p} \times \vec{B}$ contribution, variations in the beamline direction must come from the $\vec{E} \times \vec{B}$ component, which can be reduced to $E_d B$. Similarly, for small variations, the integral condenses down to $\int dz' \to \delta_z z$

Without any further z-dependence, this change is symmetric about z, so for one full cycle over a length δz, and time $\delta t = \delta z / v_{\|}$, the change in energy is (Averaging out periodic momentum)

$$\delta_z E = \frac{q \delta_z z |\delta_z z|}{\gamma m v_{\|}} E_d B \tag{2.8.36}$$

However, the opposite is true over a path in the opposite direction as the integration over z changes sign, but the integration over t does not.

2.8.3 Trap Emptying by Dipole Electrode

Suppose that a system is running with period potentials, U_0 and magnetic field, B, with dipole field, U_d. With a bore of radius r, the average amount of time it takes for an electron generated in the center of the beamline to intersect the side of the beamline can be calculated using the equations of motion.

Suppose that the uncertainty in measuring the amount of time in the trap is accounted for the in the cyclotron motion, then the average amount of time spent in the trap is can calculated by

inverting Equation 2.8.30 and solving for t. The total displacement is set to r, or the radius of the beamline at which point the electrons intersect the surface, and the sinusoidal function are averaged out to solve for,

$$t = \frac{r^2 B cos(\theta)}{\gamma(U_d(x_f) - U_d(x_i))} \tag{2.8.37}$$

Where any inhomogeneities in the dipole field is absorbed by the dipole voltage difference, $U_d(x_f) - U_d(x_i)$ over the length of the electron path. Here, the cyclotron motion on average will produce no net motion for $r > r_c$, and therefore this should be treated as the average amount of time it takes for an electron to intersect the edge of the beamline. In other words, the average time spent in the trap is:

$$\tau = x_0^2 \frac{B}{\gamma U_0} + \frac{B}{\gamma} \cdot \frac{r^2 cos(\theta)}{U_d(x_f) - U_d(x_i)} \tag{2.8.38}$$

And the estimated uncertainty is:

$$\sigma_\tau^2 = \left(p_\perp \frac{B}{\gamma m} \right)^2 + \left(\frac{B}{\gamma m} \cdot \frac{\Delta x cos(\theta)}{\sigma_{U_d}} \right)^2 \tag{2.8.39}$$

Thus, for a MAC-E spectrometer, a dipole electrode presents a possibility of reducing the amount of charge trapped in the spectrometer.

2.9 Application

The following chapter will discuss the next generation tritium neutrino mass experiment. A MAC-E spectrometer is used in this experiment. During recent studies with the KATRIN spectrometer, effects from Penning traps were observed and a dipole electrode was used to reduce these effects [45, 55, 56]. In the neutrino mass measurement, a similar dipole electrode will be used to empty a Penning trap formed by two sequentially employed spectrometers. This thesis will quantify these effects and utilize the description of the dipole electrode here to discuss the best settings for the dipole electrode and subsequently the effect on the neutrino mass measurement.

CHAPTER 3: KATRIN

This chapter discusses the KATRIN experiment. KATRIN is the Karlsruhe Tritium Neutrino mass experiment based in Karlsruhe, Germany, and is the experimental focus of this dissertation. In particular, contributions to the development of the KATRIN detector system, and the associated cosmic ray veto comprises part of the body work of this dissertation.

3.1 Experimental Goal

The next generation neutrino mass measurement, KATRIN was established to measure the mass of the electron anti-neutrino with a sensitivity of $0.2\,eV$ [39]. This provides an order of magnitude improvement over the previous generation of experiments.

The objective of the KATRIN experiment is to either provide a measurement or establish an upper limit on the neutrino mass. A neutrino mass of $0.5\,eV$ can be established as a 5σ result after 5 years of data taking. Likewise, a $0.35\,eV$ neutrino mass can be established as a 3σ result. For neutrino mass below this limit, KATRIN is designed to establish an upper limit. In either case of measurement or limit, the result provided by KATRIN will be a direct, model independent measure of neutrino mass.

Due to the requirements set in Section 2.6, the spectrometer vessel is required to be $10\,m$ in diameter to meet the $0.2\,eV$ goal. This is the largest ultra high vacuum vessel in the world and represents the efforts of over a dozen institutions in several countries.

3.2 Apparatus

The KATRIN Apparatus, as shown in Figure 3.1, is composed of several distinct sections:

(A) An extended gaseous tritium source is housed in the Windowless Gaseous Tritium Source, (WGTS) which includes solenoidal magnetic fields along the z-axis to radially constrain the motion of electrons emitted from β-decay.

(B) Electrons from the source are magnetically guided through a differential pumping section (DPS) and cryopumping section (CPS). The CPS and DPS serve to isolate the spectrometer and detector sections from the tritium gas.

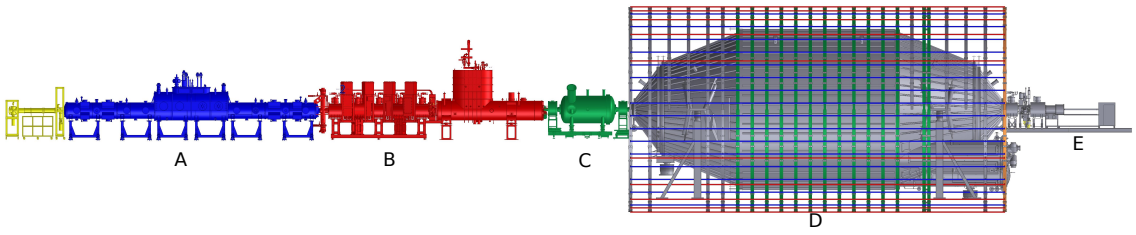

Figure 3.1: The KATRIN apparatus. The labels in the figure correspond to the itemized list in Section 3.2. The unlabeled section in yellow is the rear section of source which will be discussed in minor detail later. This is left unlabeled as this section has not been constructed at the time this thesis was written. Image courtesy of [57].

(C) A pre-spectrometer provides a first stage MAC-E filter and isolates the main spectrometer from contaminates introduced from the upstream side of the spectrometer such as residual tritium.

(D) The main spectrometer performs the MAC-E Filtering

(E) Electrons that transmit across the spectrometer are counted at the detector.

Each of these sections are described in detail below. The phrases "downstream" and "upstream" will be used to indicate towards and away from the detector section respectively.

3.2.1 Windowless Gaseous Tritium Source

The WGTS, pictured in Figure 3.2 is designed to provide a high luminosity source of electrons from tritium beta decay without a solid retainer for the tritium gas. Instead of a traditional massive window to separate the gas from the rest of the apparatus, differential pumps at either end of the source section pump tritium gas back into the center of the WGTS. Without a window, the only scattering centers for electrons are the tritium molecules present in the source itself.

By design, the source resides in a 3.6 T magnetic field and provides a $10^{11}\,Bq$ of source electrons. To provide this luminosity, the source gas is injected at $10^{-3}\,mbar$, and to isolate the downstream components differential pumps recycle that gas to a reduction factor of 10^{2} at the outlet of the source. In order to reduce scattering, the column density is kept at a density of $\rho_d = 5 \times 10^{17}\,cm^{-2}$ and cooled to $30K \pm 0.03\,K$. The full dimensions of this system are 16m in length with a beamline width of $90\,mm$ [59].

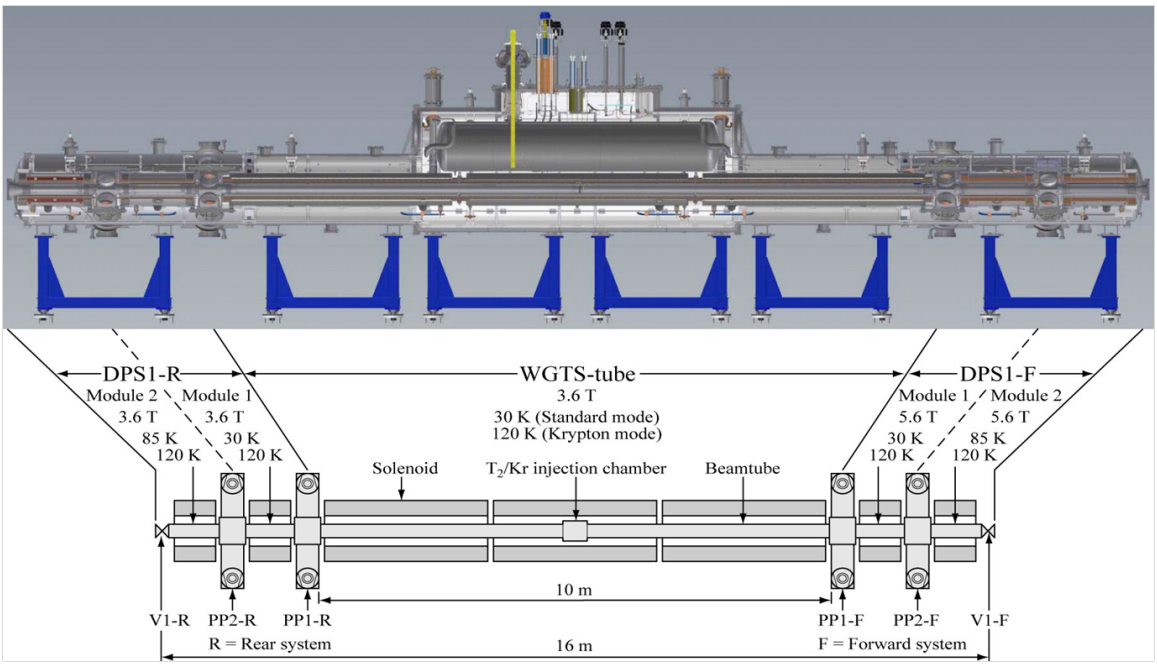

Figure 3.2: The windowless gaseous tritium source[58]. The WGTS tube in the center retains the gaseous volume while the differential pumping sections, DPS1-F and DPS1-R provide the retention. Image courtesy of [59].

Rear Section

To monitor the source, a section will be deployed upstream of the WGTS, known as the rear section. As Section 2.2 showed, half of electrons produced are guided to the spectrometer for analysis. The other half will transmit to the rear section, which is designed to count these electrons for normalizing total activity.

In the rear section, the design goal is to deploy an electron gun for monitoring scattering in the source and measuring transmission properties in the beamline. One goal of this thesis was to use another temporary electron gun during the commissioning phase of the main spectrometer to both characterize the main spectrometer and motivate design improvements for the rear section electron gun. Currently, the rear section is under design and this thesis will assist in guiding the design process.

3.2.2 Differential And Cryogenic Pumping Sections

Downstream of the WGTS, the tritium gas pressure is further reduced by the differential pumping section, DPS, as shown in Figure 3.3. The goal of this apparatus is to reduce the pressure by a factor of 10^5 while guiding electrons via a $5.6\,T$ magnetic field [60]. In addition 5 separate 20° bends in

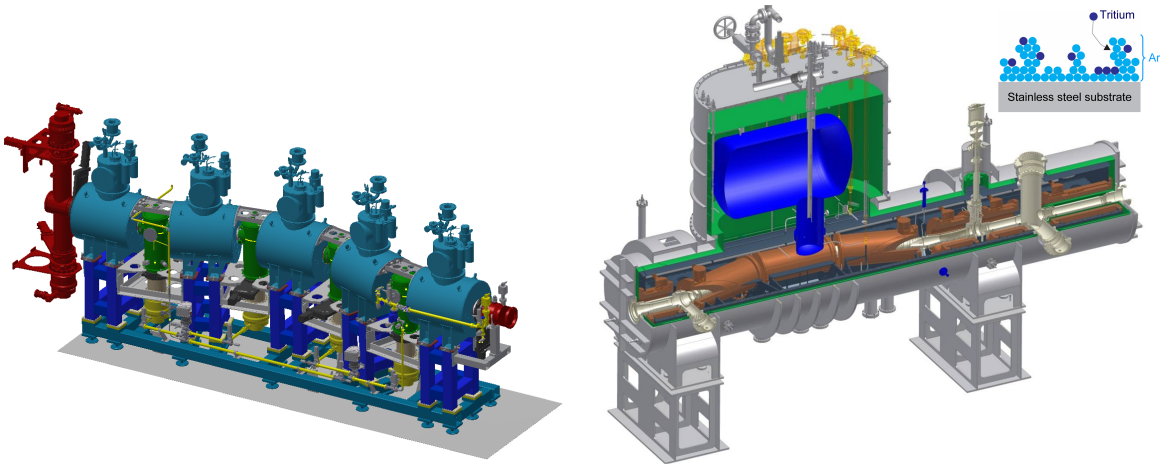

(A) (B)

Figure 3.3: (A) The differential pumping system. On the left hand side, electrons are guided by magnetic fields into a line-of-sight blocking curve. This aids in rejecting backgrounds from the source. The magnets are shown in blue with cold traps between the magnets in green for trapping tritium gas from the source. In yellow, turbo molecular pumps back the cold traps to improve the pressure reduction. Figure courtesy of: [60] (B) The cryogenic pumping system. The liquid helium dewar in blue cools the beamline in orange. The surface of which is coated in cooled Argon frost. The vacuum jacketing in green isolates the system thermally. Figure courtesy of: [61]

the pipeline are designed to deny line of sight to any energetic neutral particles.

Any remaining tritium that passes through the DPS is designed to be trapped in a secondary cryogenic pumping system, CPS. A layer of 3 K cooled Argon frost frozen to a liduid helium cooled system forms the trapping surface on the interior of the beamtube in Figure 3.3. Much like the DPS, Thus, the gaseous pressure is reduced by additional 4 to 5 orders of magnitude[61]. After 3 months of continuous operation, the CPS is expected to be saturated to the 1% level.

3.2.3 Spectrometers

As stated in Chapter 2, analysis of the tritium spectrum is performed by MAC-E filters. KATRIN utilizes two such spectrometers. A 0.85 m radius pre-spectrometer is used as an initial filter and to provide further protection against the tritium source. The 10 m radius main spectrometer is the apparatus that performs the precision filtering of electrons coming from the source.

Pre-Spectrometer

The pre-spectrometer (prespec) provides an initial filter for electrons exiting the transport sections. To provide resolution comparable to the previous generation of experiments, the radius of the spectrometer is 1.7 m, with a length of 3.4 m. Nominally, this spectrometer is expected to run at

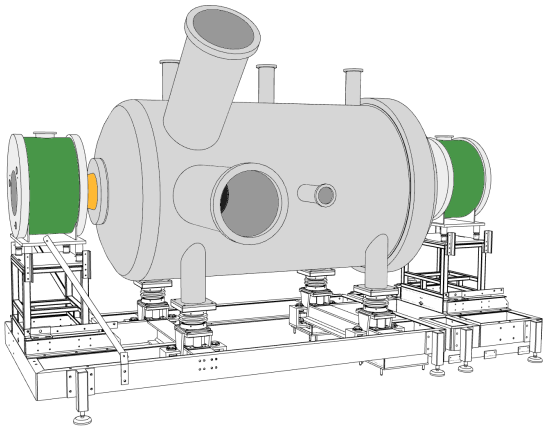

Figure 3.4: The prespectrometer. The green cyllinders on either side are the superconducting magnets which produce the field for this MAC-E filter. The large ports are for pumping with smaller ports for high voltage feedthrough. Figure courtesy of [62].

18.3 kV, with an intrinsic resolution of 70 eV. The expected reduction in electron rate is 7 orders of magnitude which is the primary purpose of the pre-spectrometer in terms of the main KATRIN measurements.

Many of the technologies utilized in the main spectrometer were developed in the prespectrometer as a test stand.

Main Spectrometer

At a length of 23.3m and a diameter of 10m, KATRIN's defining apparatus in neutrino sensitivity is the main spectrometer. This volume accounts for 1240 m^3 in which the electrostatic potential is established by setting up 18.6 kV to the spectrometer vessel. The design magnetic field values for the main spectrometer are 4.5 T at the entrance and 6 T at detector side. The vessel of the spectrometer is the main electrode for producing the analyzing potential. A nearly massless wire electrode array provides modifications to the field which allow for fine tuning of the electrostatic potential in the interior of the spectrometer. In addition, the wire electrodes provide electrostatic shielding from electrons produced on the spectrometer hull.

As the primary apparatus in MAC-E filtering, the main spectrometer provides the means for achieving several goals towards probing the neutrino mass. In Section 2.3, it was shown that the resolution of MAC-E Filters depends on the size of the spectrometer. The center of the main spectrometer has a radius of 4.5 m. Here, the field reaches a minimum of 1.2 G at the analyzing plane. In conjunction with the high fields produced by the superconducting magnets, this provides the resolution for KATRIN.

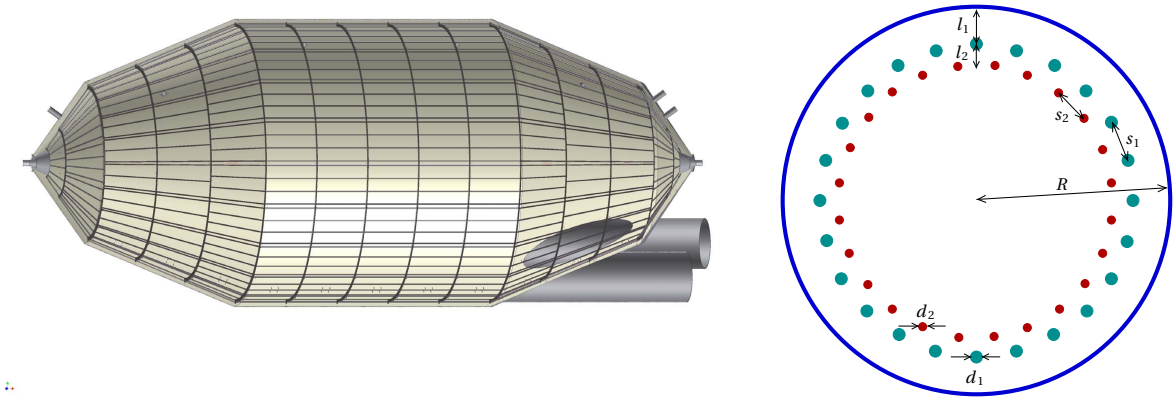

(A) (B)

Figure 3.5: The KATRIN Main Spectrometer. (A) A schematic drawing the main spectrometer as seen from the exterior of the spectrometer. The grid outlines the placement of the inner wire electrodes. The two cylinders on the underside are the getter pumps. (B) Schematic drawing the placement of the inner wire electrode system. The radius, R, is $4.5m$ with radial distances between wires of $l_1 = 150mm$ and $l_2 = 50mm$. The angular distances are $s_1 = 25.0mm$ and $s_2 = 24.73mm$. Wire diameters are $d_1 = 0.5mm$ and $d_2 = 0.15mm$. Figures from K. Valerius' thesis [41].

To reduce the pressure in the main spectrometer, three $1.7\,m$ diameter Non-evaporable getter (NEG) pumps are located underneath the detector. To shield the spectrometer from potential activity in the getter material, Liquid nitrogen cooled baffles are employed at the entrance of the pumps to deny line of sight and provide an adsorption surface. With the wire electrode array, the baffles help to reduce the background necessary for the neutrino mass measurement [63].

3.2.4 Detector

Electrons transmitting through the main spectrometer are counted at the detector system. Tandem $6\,T$ magnets guide electrons adiabatically to a 148-pixel PIN diode array located at the focal plane of the magnetic fields. This detector is known as the Focal Plane Detector or FPD. The FPD, pictured in Figure 3.6 is a collaborative work between the U.S. institutions in KATRIN and the Karlsruhe Institute for Technology. The detector system was commissioned in Seattle in 2011 and again in Karlsruhe in 2013 for usage with the main spectrometer. Figure 3.7 shows the fully assembled system with the main spectrometer.

After filtering in the main spectrometer, the expected rate of electrons at the detector is on the order of $10\,mcps$ in the $4\,keV$ region of interest centered at $18.6\,keV$ [65]. Similar to the requirements for the experiment, this requires the following:

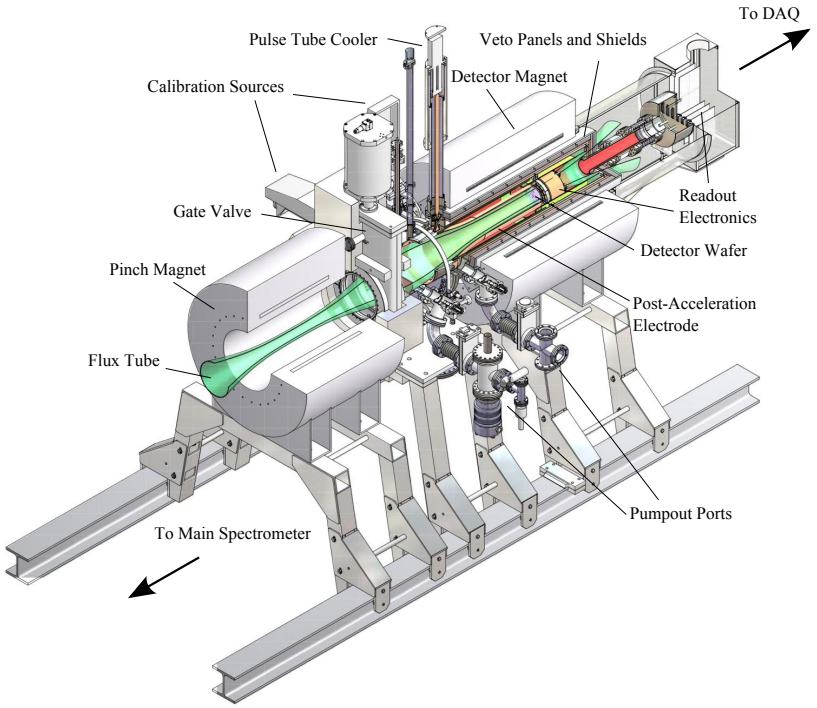

Figure 3.6: The KATRIN Focal Plane Detector (FPD)[64]. Each of the detector subsystems are labeled.The magnetic flux tube that connects to the outer ring of the detector is shown in green.

- High detection efficiency
- Low intrinsic background
- High resolving power at the tritium endpoint, 18.6 keV

The high efficiency and fine resolution is set by the choice of a silicon monolithic PIN diode array described later in this chapter. The background goal is achieved by choice of components, system cooling and the usage of shielding, also described later in this chapter.

Unlike the other components of the KATRIN apparatus, the KATRIN detector system is divided into two high vacuum regions. The beamline, and therefore the detector face is at the same pressure as the main spectrometer, 10^{-11} $mbar$. Meanwhile, since electronics are expected to out-gas, the exterior of the detector and electrode system are kept at 10^{-9} $mbar$ to reduce backgrounds[66].

Magnetic Fields

The magnetic field at the FPD is sourced by two magnets, the pinch magnet closest to the main spectrometer and the detector magnet. The field settings for these magnets are 6T at the pinch magnet to provide the field for the main spectrometer and 3.6 T at the detector magnet to provide favorable imaging at the detector face [64].

Figure 3.7: The assembled KATRIN FPD system. To the left is the KATRIN main spectrometer. The Faraday cage on the right houses the detector electronics and protects users from the high voltage area of the experiment. Image courtesy of [64]

Post Acceleration Electrode

Attached to the detector face is a copper electrode horn designed to adjust the potential at the detector which effectively shifts the electron energies as detected. By accelerating electrons towards the detector face, the energies are moved into a higher energy region with lower backgrounds. This improves the signal to noise ratio as seen in Figure 3.8. In addition, the post acceleration electrode increases detection resolution by decreasing backscatter in the detector due to high pitch angles [65].

3.2.5 Detector Wafer and Electronics

The focal plane detector itself is a 148 pixel PIN diode array. PIN diodes are three layer devices with P-type and N-type doped layers on either side of an undoped or intrinsic layer. The high efficiency requirement is met by PIN diode technology on the order of $10\,keV$. In addition, the detector geometry was chosen due to the ease in manufacturing process for PIN diodes on monolithic silicon layers at the size of the KATRIN beamline, $10\,cm$ in radius.

The detector is pixellated to provide spatial information in addition to energy and timing provided by a PIN diode and support electronics. Pixels are arranged on the detector by an innermost "bullseye" of 4 pixels surrounded by 12 rings of 12 pixels. This accounts for the total of 148 pixels, each with an area of $44.1\,mm^2$. Equal area at a uniform magnetic field means that each pixel covers

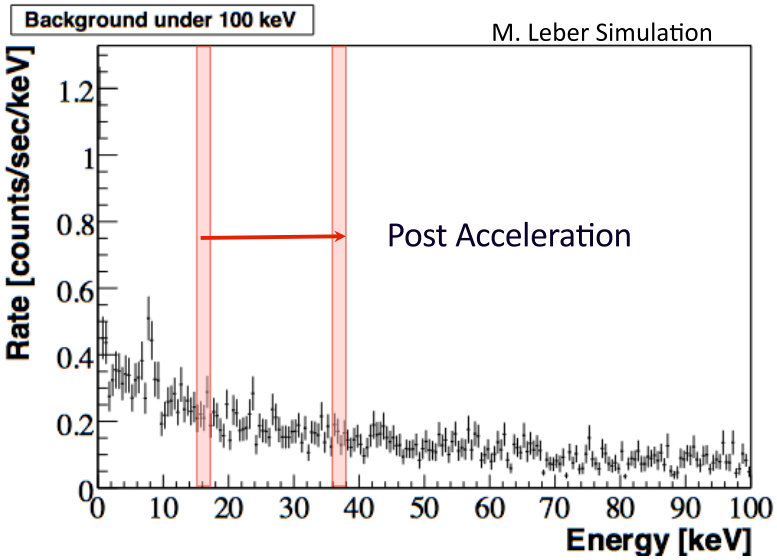

Figure 3.8: The effect of the KATRIN post acceleration electrode[66]. The black points give the background rate at the detector as a function of energy. The red regions are the unshifted and shifted regions of interest. The post acceleration electrode can be used to shift between the two by accelerating electrons from the main spectrometer to higher energies.

an equal amount of flux in the beamline in addition to having similar capacitance and therefore similar noise characteristics.

To connect the detector to the readout electronics in a separate vacuum space, a custom feedthrough flange was employed as pictured in Figure 3.10. These 184 sapphire insulated feedthrough pins provide the electrical connection from one side of the vacuum space to the other.

Electronic bias and readout are preformed by custom electronics built by the Information Processing Electronics group at the Karslruhe Institute for Technology. The front-end electronics are mounted as close to the detector as possible to reduce noise generated between the wafer and a first stage preamplifier. A carousel of 24 modules comprises the preamplifers as pictured n Figure 3.11. A characteristic signal from the preamplifiers has a rise time of roughly 250ns and fall time of 1 ms.

As the detector is held at the same voltage as the post acceleration, boards transfer the signal optically to the digitization crate.

3.2.6 Data Acquisition Electronics

Data acquisition is performed by custom hardware, designed by the Information Processing Electronics (IPE) group at KIT. This consists of a custom digitization and filtering crate, designated the Mark IV crate. Groups of 24 channels are digitized in parallel on one of 20 cards. Per card,

Figure 3.9: The face of the KATRIN FPD wafer. The wafer in this picture is layed out in a laminar flow hood for protection. Pixel boundaries can bee seen in the center of the wafer along with the biasing ring on the outside. Figure courtesy of [65].

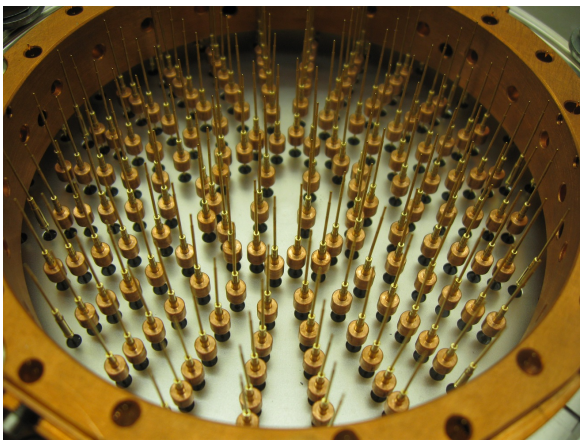

Figure 3.10: The FPD feedthrough flange. The pogo pins that provide electrical contacts are the needle structures. The copper ring around the outside is where the wafer mounts to the electronics.

3 field programmable date arrays (FPGAs) allow online customization of the filtering parameters. The Mark IV crate digitizes signals from both the FPD and the cosmic ray veto, the later of which will be discussed in Section 3.2.7

The Mark IV crate is controlled by the Object Oriented Real Time Control and Acquisition (ORCA) system developed at UNC. ORCA allows users to control experimental parameters from the same interface which controls data acquisition[67–69].

Trapezoidal Filtering

Filtering in the Mark IV crate is a multi-stage process. Each channel is passed through a series of band pass filters and a programmable amplifier. The output is then digitized at 20 MHz by a 12-bit ADC. A trapezoidal filter is used in the standard operating mode to process the ADC output.

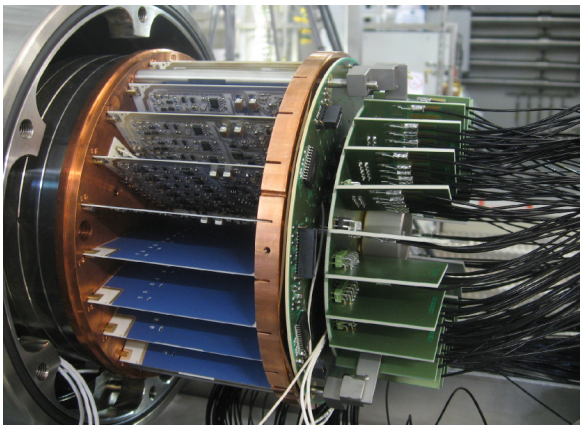

Figure 3.11: The FPD front-end Electronics. Each of the 7-8 channel preamplifier cards are shown arranged in the same symmetry as the detector face. Mounted on the left are optical sender boards for sending the signal outside of the high voltage area.

The trapezoidal filter, as pictured in Figure 3.13, uses two parameters, gap length, G and integration Length, L. Energy at a given point in time is determined by Equation 3.2.1, where $f1_i$ is the energy at time bin i for input ADC value v_i, and $v_j = v_{i+2L+G}$. Using the difference in integration windows of length L allows for filtering of noise with characteristic time less than $50ns * L$. The gap length, G rejects out signals with falling time less than $50\,ns * G$. Fine tuning of these parameters allows for more efficient signal detection and greater background reduction from electronics noise.

$$f^1(t_{adc}) = \sum_{i=t_{adc}-(L+G)}^{t_{adc}-G} v(i) - \sum_{j=t_{adc}+G}^{t_{adc}+(L+G)} v(j) \tag{3.2.1}$$

The second stage filter in Figure 3.13 establishes timing. A trapezoidal filter with a gap length of 0 or, "triangle filter" as it is commonly referred to, takes the differential of the first stage filter. This is shown in Equation 3.2.2. Utilizing the same integration length, L, allows the second filter to acquire the same noise rejection characteristics of the first stage filter.

$$f^2(t_{adc}) = \sum_{i=t_{adc}-L/2}^{t_{adc}} f^1(i) - \sum_{j=t_{adc}}^{t_{adc}+L/2} f^1(j) \tag{3.2.2}$$

Triggering occurs when the energy is above a programmable threshold value. When a trigger occurs, timing is established as the time bin, t_{adc} where $f^2(t_{adc}) = 0$. The energy value of the signal is defined as the first stage filter output at this time bin. Prior to running this filter, the user also has the option to acquire full trace information or just the timing and energy values. For either mode of operation, channel mapping information is included with the trigger output or "event data".

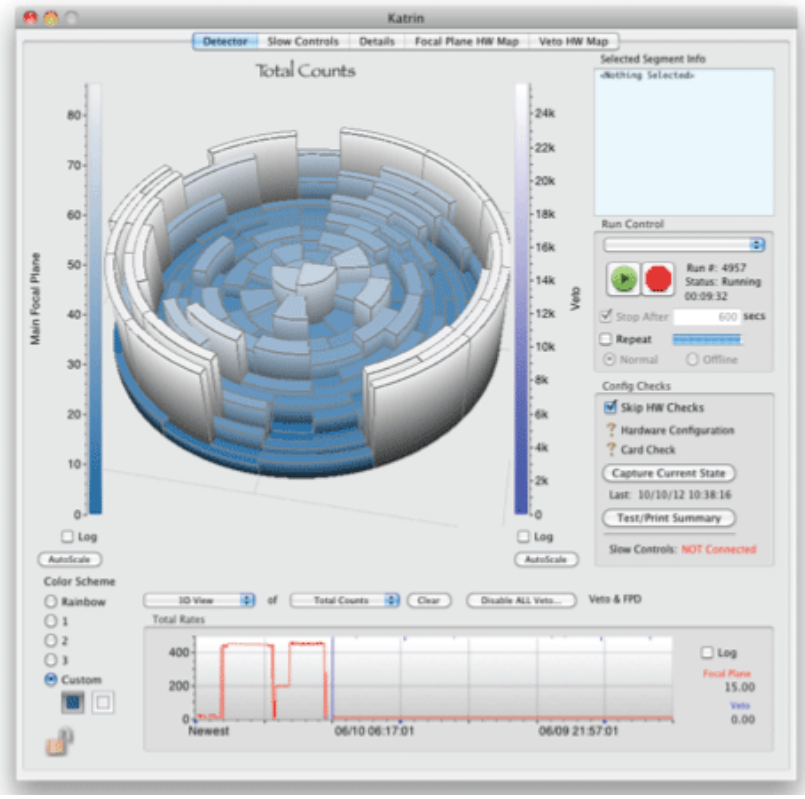

Figure 3.12: ORCA Readout of the KATRIN FPD. Data rate on the pixels is displayed as a 3D histogram. Lighter colors and "higher" pixels correspond to higher rates on the detector. The other available controls for the KATRIN FPD are shown in the same pane.

Data output can be seen in Figure 3.14. The information included here is the event rate at the detector. Each pixel is colored by the rate value.

3.2.7 Cosmic Ray Veto

To achieve the low background goal, the FPD is shielded by the veto system. This system is detailed in Appendix C.

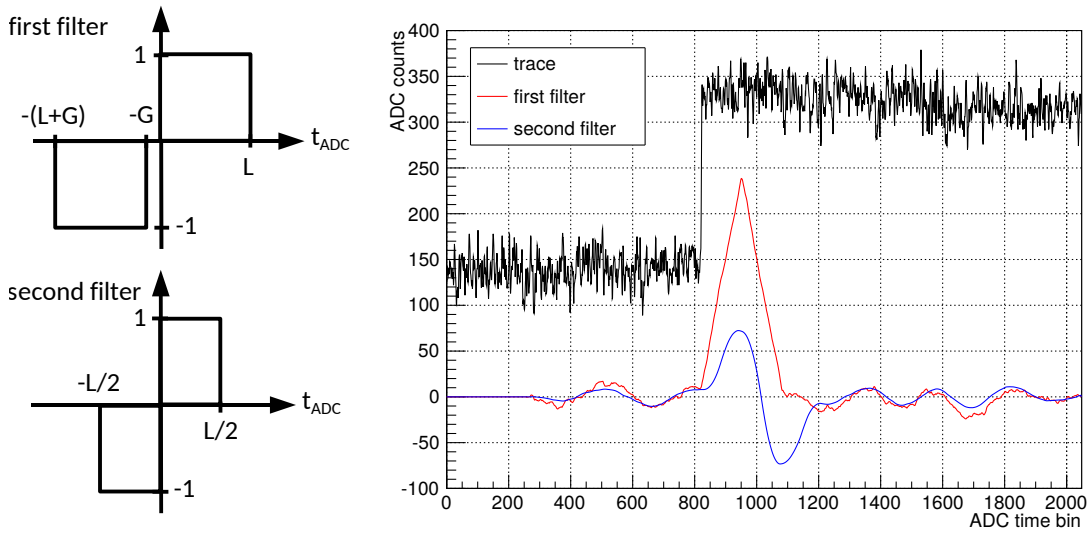

Figure 3.13: FPD Signal through the Mark IV trapezoidal filter. On the left is the trapezoidal filter geometry. Each of the windows sums over the ADC bins, and the directionality shows the sign of the contribution to the filter value. On the right is the raw readout in black, the first stage filter in red and second stage filter in blue. Figure courtesy of [70]

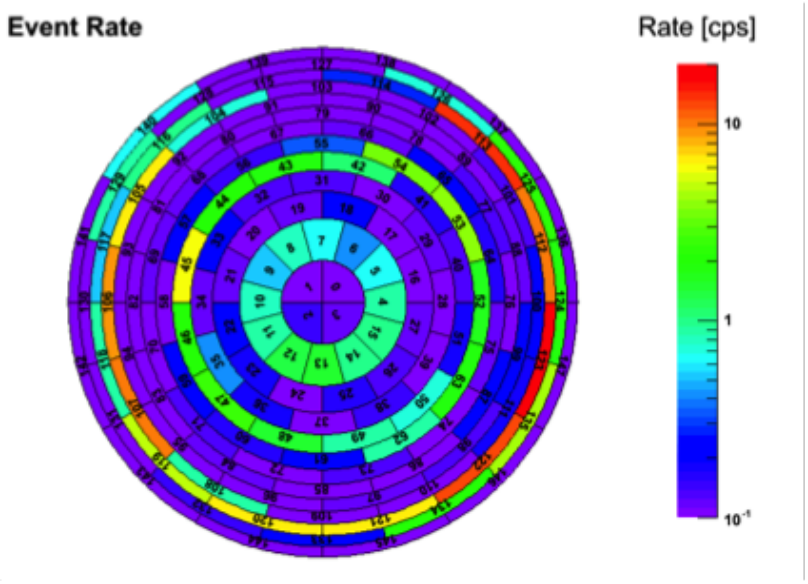

Figure 3.14: An example of data collected at the detector. Each channel is readout and the rate of triggering or "Event Rate" is shown at each pixel. Data for this figure was taken during the "First Light" runs in the commissioning process from Chapter 4 and imaged using the internal KATRIN software[71].

CHAPTER 4: SPECTROMETER AND DETECTOR SECTION COMMISSIONING

This chapter discusses the recent efforts to commission the KATRIN Spectrometer and Detector Sections. The measurements described in this dissertation are part of the commissioning efforts.

4.1 Goals

Starting in July 2013, the KATRIN experiment began the Spectrometer and Detector Section (SDS) commissioning phase. The goals of this phase were to measure the transmission properties mentioned in Section 2.4, provide accurate estimates on background processes in the experiment and explore potential systematics inherent to the apparatus. In short, commissioning these sections evaluates KATRIN's ability to reach the goals listed in Section 3.1.

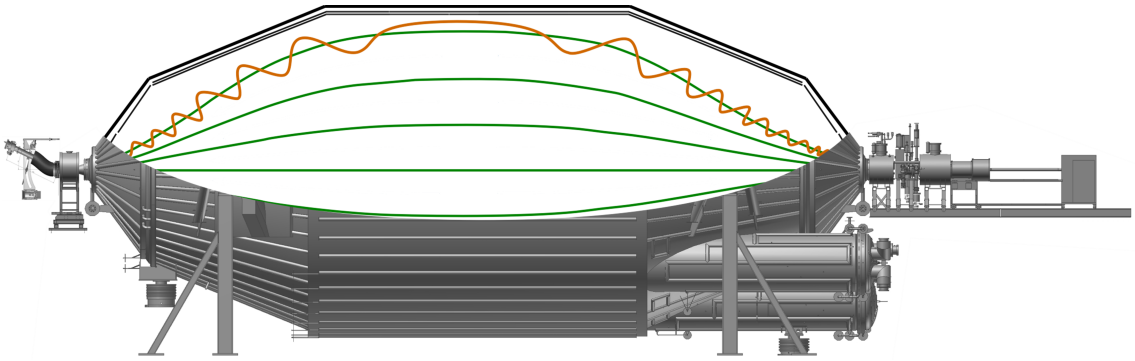

Figure 4.1: The SDS Commissioning Apparatus. At the right is the focal plane detector. To the left is the commissioning EGun. A single electron track in yellow is shown transmitting across the main spectrometer and guided by one of the magnetic field lines in green.[55].

A phased approach was taken during the SDS commissioning process. The first phase, *SDS Phase-I*, was undertaken during July 2013 through November 2013. Improvements were then made to the system due to the findings of the Phase-I commissioning. The second commissioning phase, *SDS Phase-II* was undertaken during September 2014 to July of 2015. While this dissertation work focuses on the second commissioning phases, a third commissioning phase was undertaken from July 2015 through to January of 2016 to identify previously unknown backgrounds. KATRIN will continue the overall commissioning process with the source and transport sections in late 2016.

4.2 Commissioning Apparatus

The SDS commissioning apparatus as depicted in Figure 4.1 differs from the main experimental apparatus by the addition of an electron gun, or *EGun*, where the pre-spectrometer is usually coupled to the main spectrometer. In addition to the EGun, the main spectrometer and detector system make up the rest of the commissioning apparatus. The EGun will be used to probe the transmission function. Together with precise knowledge of the source properties, the response function of the apparatus can be used to describe the resolution in the endpoint region of tritium beta decay and the experiment's sensitivity to neutrino mass.

4.2.1 The Electron Gun

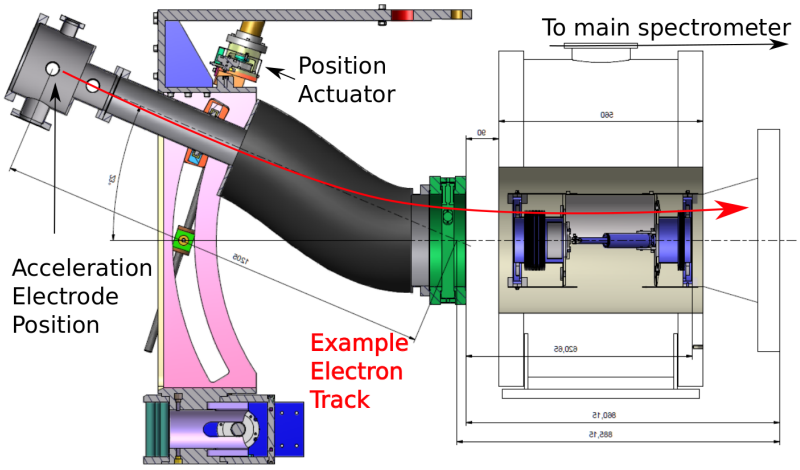

Figure 4.2: Schematic of the Commissioning Electron Gun. The right side is connected to the main spectrometer as illustrated in Figure 4.1. Electrons are produced in region near to the acceleration electrode. These electrons then follow the magnetic fields lines through the manipulator, then through the magnet and into the spectrometer. Figure from [72].

The University of Muenster designed and built the EGun [72] specifically for the commissioning measurements. In addition, several improvements were made over the course of the commissioning phase. As detailed later in this chapter, a dipole electrode was introduced to reduce the effects of Penning traps. The geometry of the electrode system was improved over several iterations to improve angular and energy resolutions. For the latest set of improvements, the University of North Carolina participated in the development cycle.

The electron gun is designed to probe the transmission function by providing monoenergetic and angularly resolved electrons. By providing single energy and angular values for the transmission function in Equation 2.4.3 and measuring the transmission ratio, the electrostatic and magnetostatic

field strengths can be evaluated. Schematically, the EGun system is shown in Figure 4.2.

To probe the full volume of the main spectrometer, the EGun vacuum system is mounted on a 2-axis manipulator. By rotating a manipulator arm around the beamline axis, the EGun can be maneuvered into different portions of the flux tube. This gives the EGun the ability to select which positions in the main spectrometer to probe. By design, the maximum angle the manipulator arm can achieve is 23°, which corresponds to the outside region of the flux tube that connects to the outer active region of the detector wafer, thus achieving full flux tube coverage.

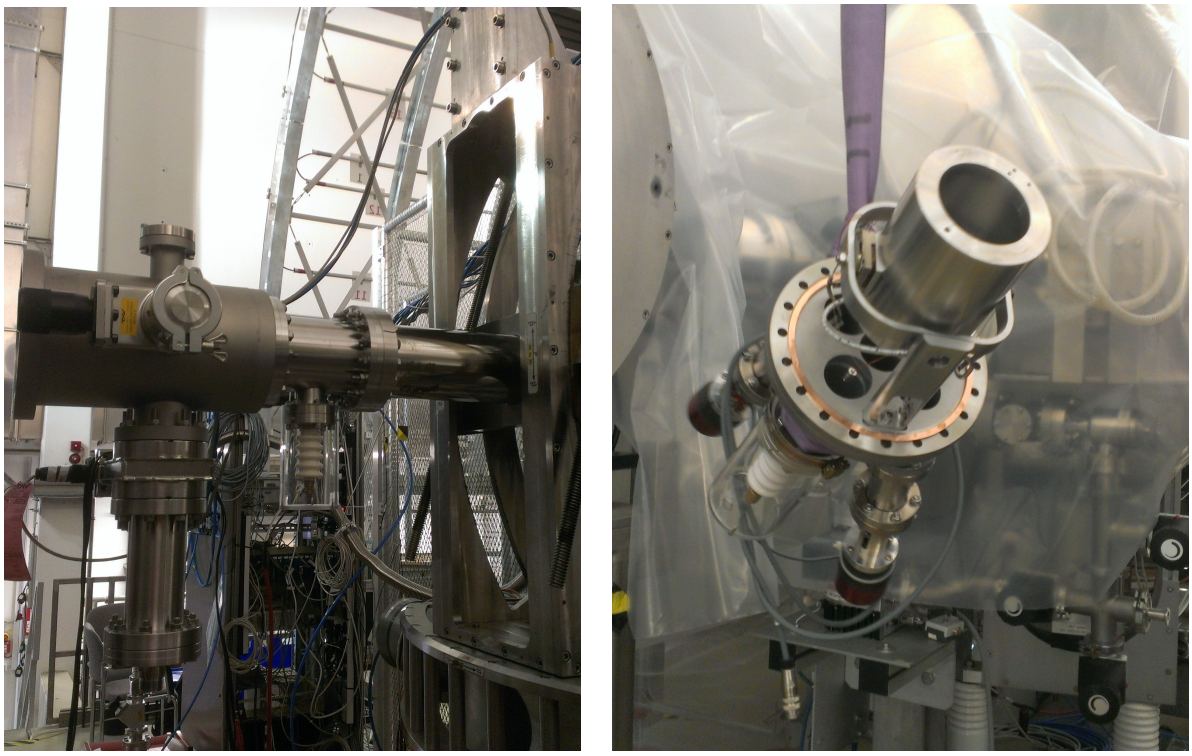

(A) (B)

Figure 4.3: (A) External view of the commissioning EGun. To the right is the main spectrometer. On the left is where electrons are generated. The vertical manipulator is on the left hand side. In the lower left hand corner is the horizontal manipulator. Please note that this photo was reflected in order to maintain the "left to right" orientation of figures in this section. (B) The EGun angular manipulator. The main chamber is mounted to a flange for ease of access. The 2-axis angular gimble system is shown supporting the "can" where electrons are generated.

In the interior of the Egun, a second manipulator, pictured in Figure 4.3 is designed to allow users to select angles by aiming the EGun relative to the magnetic field. The maximum angle in any direction that this system is designed to achieve is 17° on the far side of the prespectrometer magnet. Electrons coming from the tritium source in the production system are produced without angular preference. However, due to the angular acceptance mentioned in Section 2.5, KATRIN is

designed around an angular acceptance of 50.77° at the source beamtube [39]. Therefore, the EGun only covers a portion of the production source phase space, but this should be sufficient for probing transmission properties.

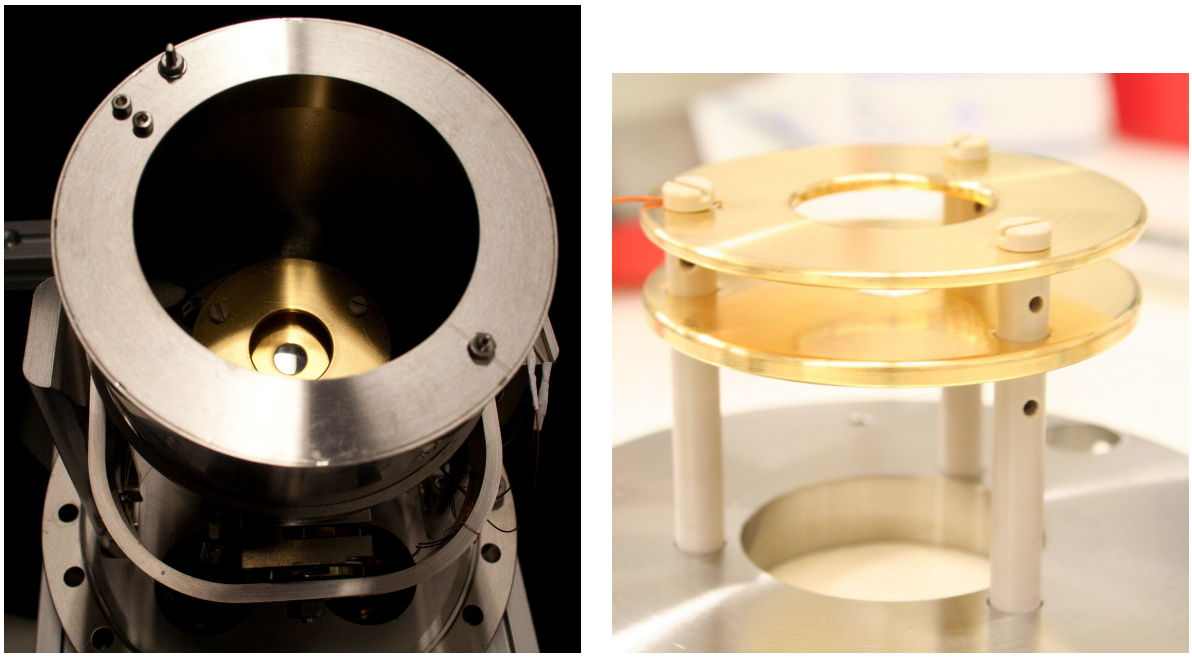

(A) (B)

Figure 4.4: The interior of the electron gun. The parallel plate electrodes are coated in gold to match the workfunction of the photoelectric surface. (A) The exterior of the EGun electrode "can" is shown with the acceleration electrodes in the center. (B) The gold acceleration electrodes are shown separated from the main apparatus. The bottom electrode is the backplate and the top plate is the acceleration electrode. Pictures from [72]

Photoelectrons are produced by shining UV through a wavelength shifting fiber onto a gold evaporated surface shown in Figure 4.5. An annular acceleration electrode guides the electrons away from the photoelectric surface. These electrodes are shown in Figure 4.4. Electrons produced in this manner are created with energy equal to the potential the backplate is set plus an adjustment factor. This adjustment factor accounts for energy loss in the workfunction and the initial energy due to the photon energy.

The light that is used to produce electrons is sourced through a wavelength shifting fiber on a $200\mu\, m$ diameter, $40\, nm$ thick photoelectric surface[62]. The light source itself is an InnoLas Holding UV laser operating at $266\, nm$. This laser is pulsed in bunches of $20\, ns$ at a frequency of $20\, kHz$ to $100\, kHz$ which allows for data acquisition synchronization with the detector. In addition, a monochromator is used to fine tune the light from the laser to achieve a total rate of a few kcps. If the monochromator is operated close to the energy threshold defined by the work function of the

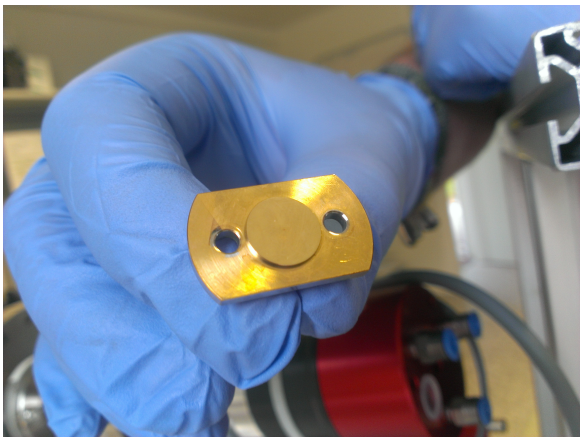

Figure 4.5: The EGun photoelectric surface. This flange is plugged into the backplate to achieve the bias potential. A WLS is inserted in the back to create photoelectrons.

gold electrode, then the expected energy distribution of electrons is small compared to the analyzing potential, in the regime of 0.5 eV.

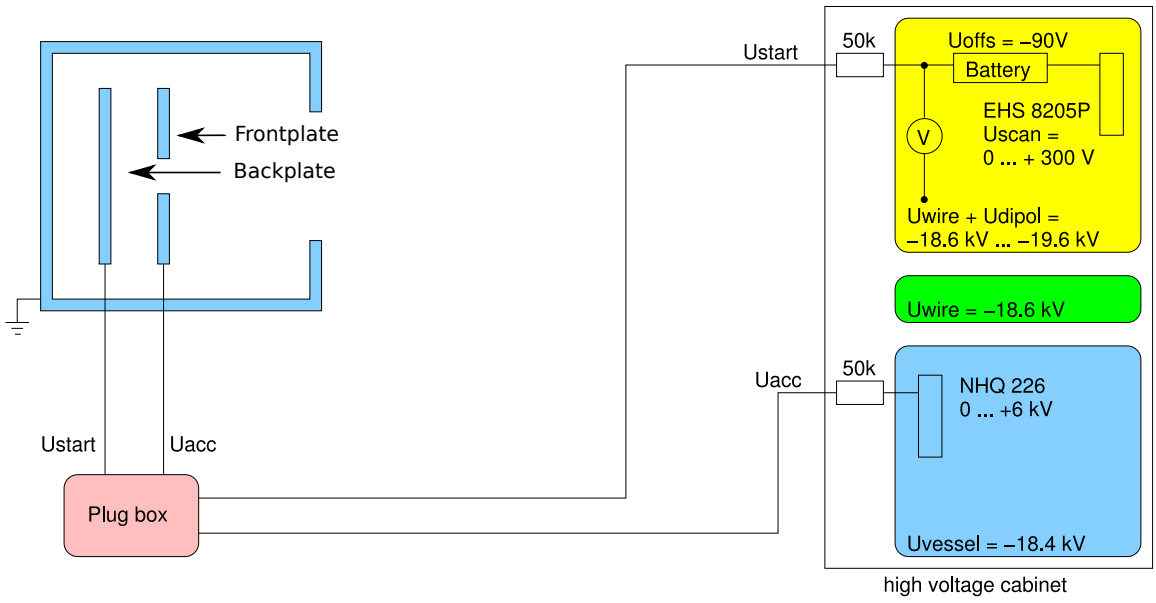

Figure 4.6: EGun High Voltage Schematic. For the commissioning data taking runs, ground in this scheme can be considers to be U_{wire}. Figure from [72]

To measure the transmission function, the energy of electrons must span an energy range that is close to the analyzing potential. The potential difference between the parallel plates is kept at a constant nominal value, usually 5 kV. In order to produce electrons with energies close to the analyzing potential, the backplate electrode power supply uses the analyzing electrodes as a local ground. Increasing the electron energy relative to the analyzing potential is then a matter

of applying an offset voltage, U_{scan} to the backplate power supply. To achieve energies below the analyzing potential, a battery is connected between the power supply and the backplate electrode which provides a constant voltage of $U_{off} = -90\,V$. The EGun backplate potential is therefore:

$$U_{start} = U_{wire} - 90V + U_{scan} \tag{4.2.1}$$

Where U_{start} is the starting potential of electrons, and U_0 the analyzing potential. This voltage difference is measured to the $5\,mV$ level using a 7.5 digit NI-PXI DMM 4071 multimeter[73]. Electrons are accelerated away from the backplate using an annular frontplate electrode with a potential, U_{acc} applied relative to the vessel voltage, U_{vessel}. This acceleration potential is kept static as this potential has no appreciable effect on the electrons after they've left the EGun system. This setup is detailed in Figure 4.6.

4.2.2 Method of Measuring Transmission Functions

Given the current model for the transmission function in Equation 2.4.1, measuring the transmission function requires scanning the initial phase space spanned by E_e and θ_{pch}. As tritium is an isotropic source, a common simplification is to remove angular dependency as in Equation 2.4.3, which reduces the transmission function down to a function of the energy. Therefore, obtaining a transmission function requires a user to scan the EGun backplate potential relative to the analyzing potential and count the number of electrons that impact the detector.

For considering effects in the EGun itself, this approximation no longer holds as electrons generated at the EGun surface have an initial E_e and θ_{pch} distribution of their own. The EGun electrons have initial energy given by Equation 4.2.1. The spread in the initial electron energy must also be considered. Therefore, the model used in many of the SDS commissioning studies is a gaussian source. For the angular distribution, a cosine distribution is used as surface effects in the photoelectric surface should be "smeared" by macroscopic imperfections in the evaporated surface. For all other parameters in this system, the nominal values are listed in Table 4.1.

An example transmission function is shown in Figure 4.7. Immediately, the shift in the lower edge due to the work function is visible along with the width change due to the EGun spread. The transmission here is calculated as the number of electrons detected at each backplate voltage normalized by the number of electrons detected at the highest potential.

Since the analytic models do not account for 3D geometry or imperfections in the field, Monte Carlo simulations can be used to compare against measured transmission qualities.

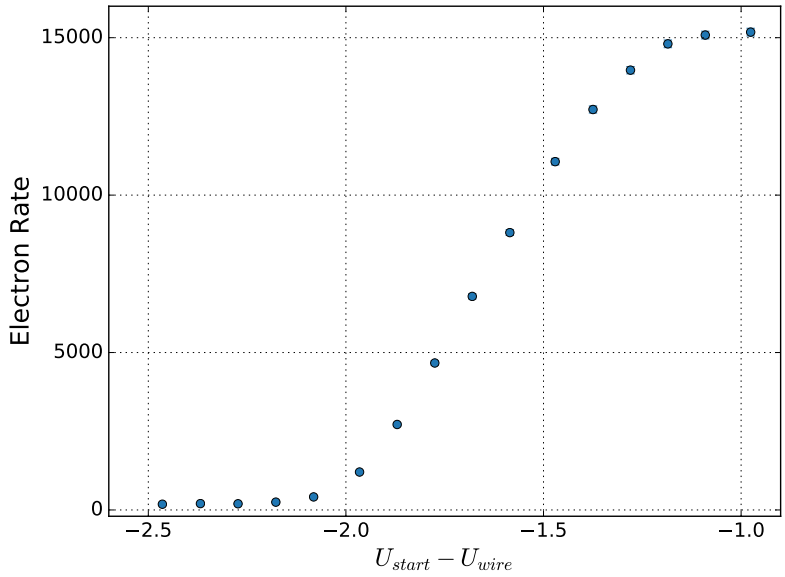

Figure 4.7: An example transmission function measured with the egun and nominal field values.

Physical Variable	Theoretical Value	Physical Apparatus Potential	Nominal Value
U_{start}	E_e	EGun Backplate	$-18600\,V$
U_{acc}	N/A	EGun Acceleration plate	$5000\,V$
U_{scan}	$E_e - U_0 + 90$	EGun Backplate Power Supply	$0\,V$
U_{dip}	U_{dip}	Dipole	$4000\,V$
U_{gnd}	0	Absolute Ground	$0\,V$
U_{vessel}	$U_0 - 200$	Main Spectrometer Hull	$-18400\,V$
U_{wire}	U_0	Main Spectrometer Wire	$-18600\,V$

Table 4.1: Nominal electrode potentials for transmission function runs. The EGun backplate potential is usually the control value for transmission functions, but for background runs and other types of runs, this is held at the nominal voltage above. All other values are held at these static variables for transmission function runs.

4.3 EGun Evaluation

Commissioning the KATRIN spectrometer and detector sections required the development of an electron gun, or EGun, to probe the transmission properties of the spectrometer. The EGun developed by the University of Muenster delivers electrons with well defined energy and momenta distributions. In addition, the EGun provides the ability to select average energy, momentum relative to the magnetic field and position in the flux tube. The resolutions of the EGun were measured *in situ* during the commissioning process. The EGun's ability to select position and angle were observed during the initial testing of the EGun. The maximum electron rate at the detector was observed during testing by grounding the vessel and wire electrodes and zero-ing the EGun angles

to observe unobstructed rate at the detector. These values are detailed in Table 4.2.

Property	Value
Energy Resolution	$0.15\,eV$
Angular Resolution	4.3°
Position Selection	$\pm 23^{\circ}$
Angular Selection	$\pm 17^{\circ}$
Maximum Electron Rate	$< 100\,kcps$

Table 4.2: Measured EGun Values[73]. These values were recorded using the SDS apparatus. The properties marked as "Selection" show the allowed ranges for the parameters.

4.4 KATRIN Software

KATRIN utilizes a C++ package, Kasper, to perform Monte Carlo style simulations[74]. This package is composed of three parts. Experiment geometry is expressed in a package known as KGeoBag. Electromagnetic field simulations are performed in a package known as KEMField. Finally, particle tracking is performed in a package known as Kassiopeia.

To compare data against simulation, the Kasper package was used to simulate the transmission function measurements. This simulation was built in conjunction with the University of Muenster on top of components built by KIT and the Massachusetts Institute for Technology.

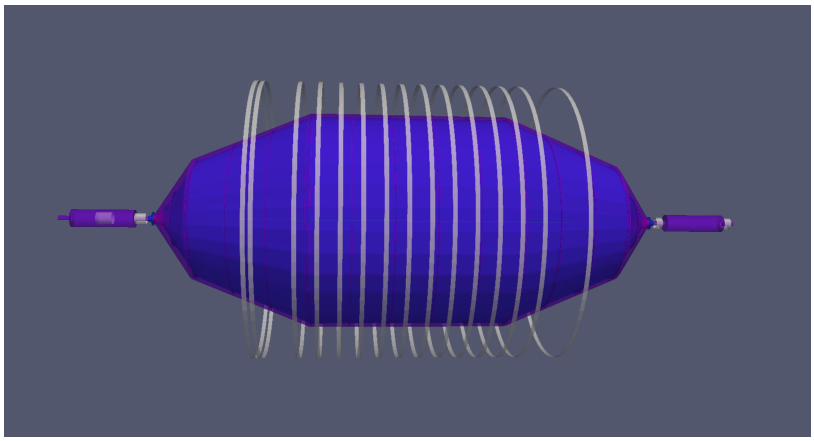

Figure 4.8: The modelled main spectrometer. Electrodes are displayed in purple with magnets in grey.

4.4.1 Geometry

To describe generic 3D models for physics simulations, the geometry package, KGeoBag was created for use in KATRIN. KGeoBag is designed to be extensively used in both the electromagnetic

field calculations and particle tracking software interchangeable. Geometries are described in XML which binds to object oriented models of shapes built into the library.

An option for viewing these geometries is the Visualization Toolkit (VTK). For example, the KATRIN main spectrometer is pictured in Figure 4.8.

For use in the commissioning measurements, the EGun geometry was created to accurately portray the electrodes in the experiment. Since electrons traversing the simulation see only electromagnetic fields, the requirement for designing this geometry is therefore to create accurate electromagnetic fields. Special attention then had to be paid to edges and regions where electron might closely approach the electrodes. These are the areas where numerical accuracy is most likely to drop. The planned rear section EGun discussed in Section 3.2.1 will have a geometry that will be use a similar design to the commissioning EGun, but optimized for robustness. Similarities in the geometry therefore motivate re-using pieces of the simulation geometry between the two EGuns.

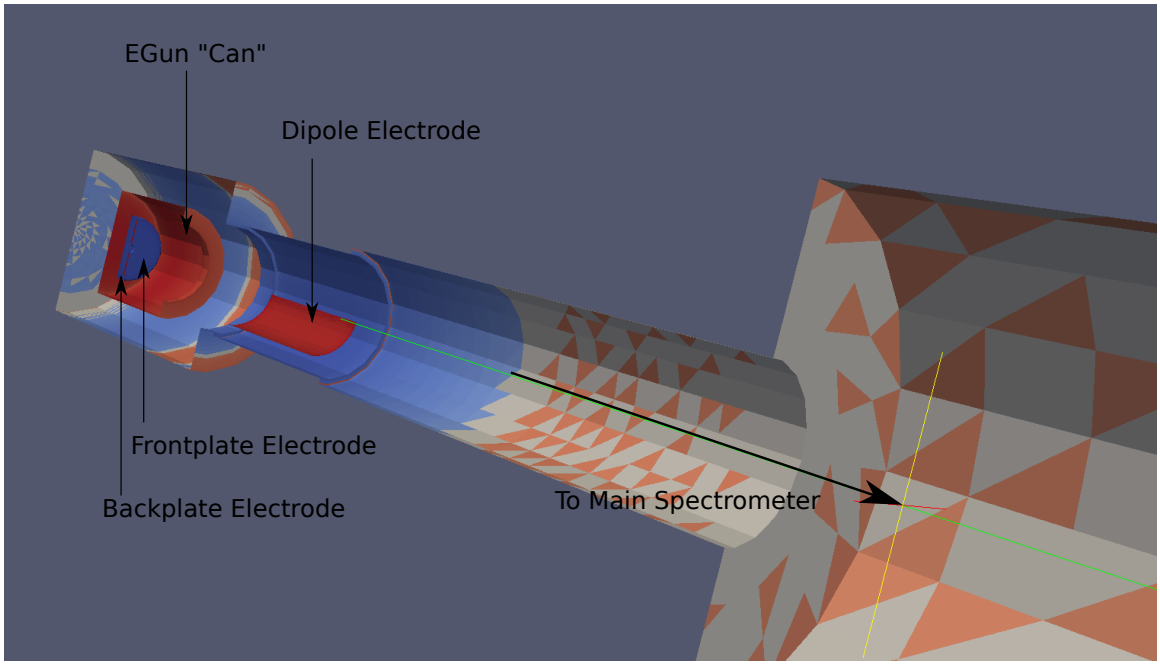

Figure 4.9: Simulated EGun geometry. The physical surfaces are displayed here, colored as a function of surface charge density at nominal field settings. Blue represents more negative electric charge with red representing positive. The shapes on the surface represent the discretization at each surface. The large shapes on the beamline correspond to coarsely discretized regions where the charge between adjacent elements is required to be different to satisfy boundary conditions.

4.4.2 KEMField

Full 3D electromagnetic field calculations are done in the package, KEMField[75]. This is a toolkit written in C++ for efficient calculation in highly parallelized computational frameworks. Similar to KGeoBag, the configuration of KEMField components in KATRIN simulations is handled by XML bindings set by the user.

For the EGun simulation, accuracy limits had to be placed on the geometry described in the KGeoBag framework. The controlling factor in accuracy is in surface discretization or "meshing". KEMField calculates charge density at each discretized point as a function of potentials applied to electrodes. Therefore, the finer the discretization, the more accurate the calculation, but also the longer it takes to compute the charge densities. The meshing for the EGun section was computed as the distance between mesh points as a function of the closest approach distance by electrons in the simulation. The rule of thumb is that to achieve the desired accuracy, the inter-mesh distance is required to be one order of magnitude below the closest approach distance by an electron. The resulting field calculation is shown in Figure 4.10.

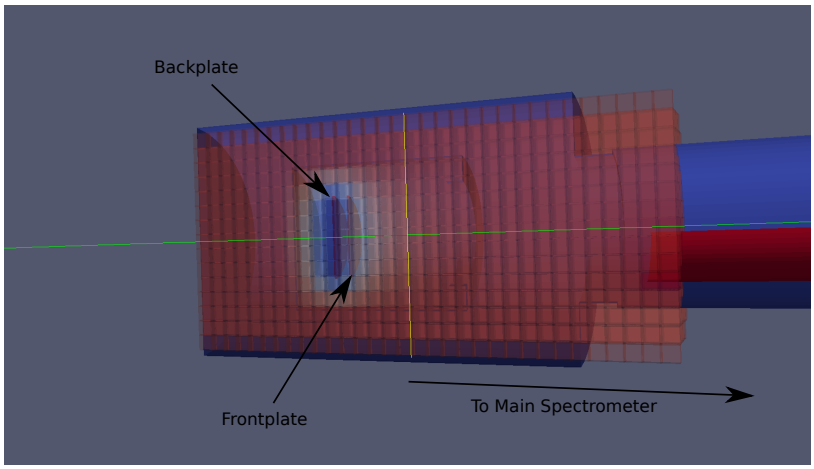

Figure 4.10: The squares superimposed on the simulated EGun geometry map the potential at the center of each square. Blue is more electrostatically negative and red positive. This figure shows the regions where the electric field is least uniform and therefore requires higher accuracy when calculated.

Once again, this work can be recycled for the rear section EGun. Calculating the inter-mesh distance is a time consuming process due to the time it takes to calculate the field, then check the electron tracks against the mesh distance, which repeats.

4.4.3 Kassiopeia

Particle tracking is performed in framework known as Kassiopeia. Like the other components in Kasper, Kassiopeia was created specifically for the KATRIN experiment, though it has found applications outside of KATRIN. Kassiopeia is designed to efficiently and accurately track electrons through complex 3D geometries.

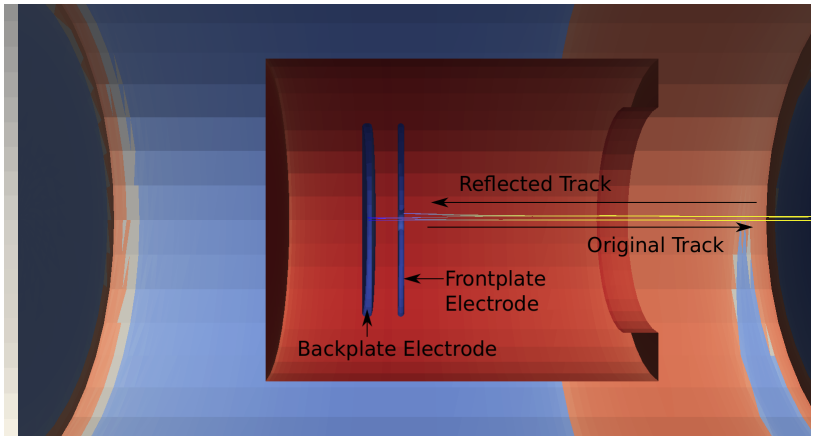

Figure 4.11: Side view of a particle track in the simulated EGun.Here, a track is started at the photoelectric surface and terminated at the frontplate electrode. The electrodes are once again painted with charge density and the track is painted by kinetic energy.

Particles are created in Kassiopeia using generators which create particles either on surfaces or in volumes. At each point in a particle's trajectory, Kassiopeia samples the electromagnetic fields, and uses pre-defined integrators to calculate the next step in the trajectory. In addition, at each point, the geometry is sampled for terminating surfaces in the geometry. Particle tracks are killed either when a terminator is specified or the particle leaves the top-level KGeoBag geometry, or the "world".

For the commissioning EGun, Kassiopeia is configured to create tracks at the photoelectric surface. Users can specify one of a number of generator types. For instance, debugging the simulation is best done using a delta function generator to produce particles with a well defined energy and momentum.

Several different tracking mechanisms are used in the KATRIN EGun simulation. Close to the electrodes, an exact calculation is used in order to achieve precise control over the starting energy of electrons. Far from the electrodes, an adiabatic approximation is used to decrease the amount of time spent in simulation. An example track in the simulated EGun is shown in Figure 4.11.

Special care is taken when treating reflected electrons for use in studying trapped particles due to the importance of trapped electrons in Chapter 5.

The full EGun simulation was created for this dissertation in concert with the University of Muenster. As demonstrated, this simulation will be used in future studies in the KATRIN experiment, namely for simulating the rear section EGun.

4.4.4 Preliminary Simulation Results

A simulation of the EGun was developed using the software suite specifically designed for KATRIN's needs. The simulated geometry creates an analogue to the physical EGun apparatus. Electromagnetic fields are calculated to an accuracy of 10^{-6} for the available electron tracking positions. Electron tracking is also calculated to an accuracy of 10^{-15} in the simulation.

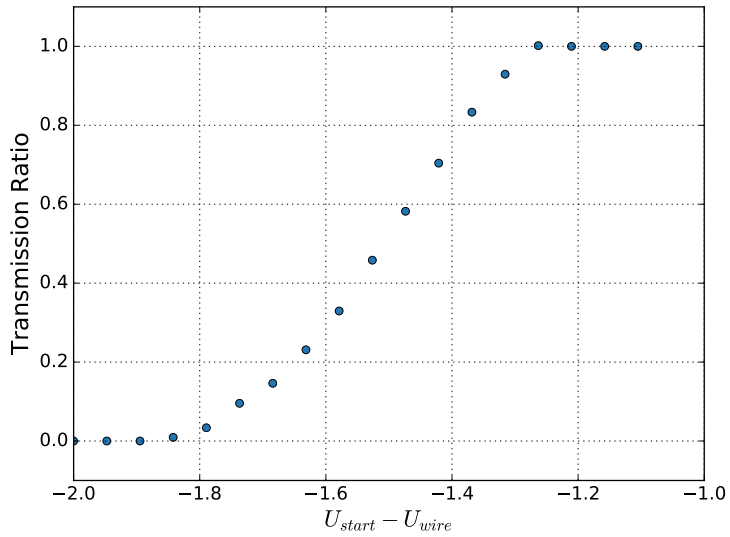

Figure 4.12: An example simulated transmission function. In this case, the raw fraction of electrons detected vs those produced in 10,000 events are shown. The x-axis is the difference in potential between the EGun backplate and the analyzing potential.

Figure 4.12 shows a transmission function observed from the simulation. The potential on the backplate is changed at each point. Therefore, for each point, the simulation recalculates the electrostatic potential, then tracks 10,000 electrons. The transmission ratio is calculated as the number of electrons crossing the detector face divided by 10,000. The similarity between Figure 4.12 and Figure 4.7 shows that the simulations can model the data to a basic extent.

4.5 EGun Simulation Applications

The EGun simulations are being compared to physical measurements to quantify any inaccuracies in the construction of the simulation. In addition to probing the model of the EGun, the

simulations can provide information that measurements are not designed to provide. For instance, in the physical apparatus, the initial and final states of electrons can be measured using the current meter on the EGun and the rate at the detector. This can be replicated in simulation by controlling the number of electrons produced and measuring the number of electrons incident on the detector face. However, the simulations can also provide information on the particle trajectories which may lead to the accumulation of charge in main spectrometer. The next chapter will explore this idea by comparing the simulated effect with a measurement using the EGun.

CHAPTER 5: CHARGE ACCUMULATION

This chapter will focus on the simulations and measurements of charge accumulation in the KATRIN main spectrometer. Charge accumulation can introduce a systematic error in transmission function measurements and thus the neutrino mass measurement. This chapter presents a simple model of charge accumulation, a measurement of the effect on the transmission function, a comparison against simulation and finally the simulated effect on the neutrino mass sensitivity.

5.1 Initial Indications of Charge Accumulation

Transmission functions are measured by manipulating the initial energy, E_e of electrons via the EGun backplate potential. It should be noted that this is one of two orthogonal ways of measuring the transmission function, the other method is to change the analyzing potential. The choice to manipulate the backplate potential was made due to the time it takes to stabilize the high voltage apparatus. For a standard data set, the absolute backplate potential is set to roughly 2 eV lower than the analyzing potential, U_0, thus producing electrons with mean starting energy 2 eV below transmission. The rate of electrons transmitting across the main spectrometer is measured as the average number of electrons detected in 1 second intervals over a period of 10 s. At the starting potential, the electron rate at the detector should be close to 0 cps.

In increments on the order of 100 meV, the backplate potential is increased and the rate at the detector is measured. This process is repeated until the initial electron energy is well above the transmission edge where the detected rate should be identical to the rate emitted by the EGun, which is roughly 15 $kcps$ for SDS Phase-I, or 6 $kcps$ for SDS Phase-II. The detected rate as a function of the electron initial potential energy in excess of the analyzing potential, or $E_e - U_0$ is referred to as a measured transmission function.

Alternatively, the EGun backplate potential can be scanned in the opposing direction by setting the backplate potential to a potential energy above transmission. At this potential, the detector should register the full rate of electrons emitted by the EGun. The backplate potential is then decreased until the potential is below transmission or 0 cps on the detector. For simplicity, increasing the backplate potential and therefore the electron energy will be referred to as measuring a

transmission function "up" and likewise decreasing the backplate potential will be referred to as measuring the transmission function "down". Performing a measurement either way in ideal conditions theoretically produces identical results. However, during the initial commissioning phase, the transmission function in Figure 5.1 was measured, indicating non-ideal conditions.

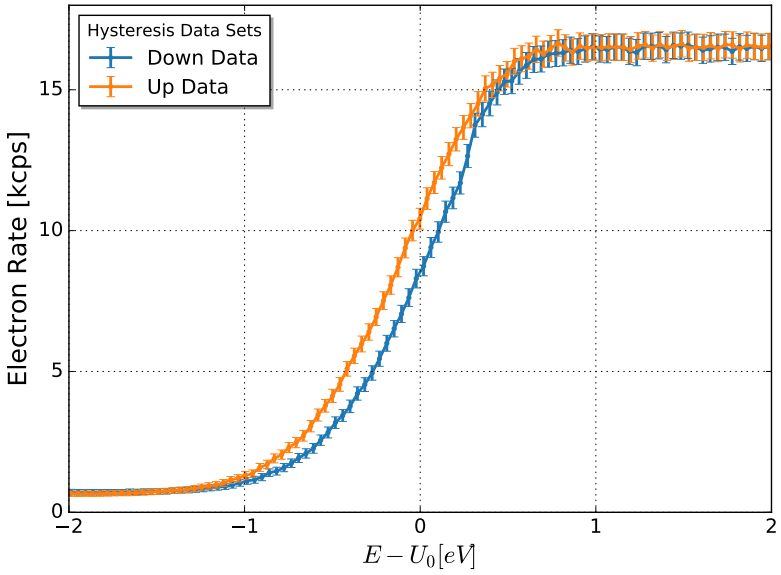

Figure 5.1: Hysteresis in the transmission function. Blue indicates data taken in the "down" direction and orange in the "up" direction. In this case, this is the absolute rate measured at the detector instead of the transmission ratio. Data sourced from SDS Phase-I measurements taken by Jan Behrens.

The observed difference between up and down measurements is referred to as hysteresis. This thesis will develop a simple model to explain why this deficit occurs. In addition to this measurement, several large discharges were detected in the initial commissioning phase. These are suspected to have originated from Penning traps. Collectively, the discharges and hysteresis effects have been qualitatively theorized to be the results of Penning-trapped particles in the main spectrometer.

A dipole electrode as described in Section 2.8 was added to the commissioning apparatus to combat the Penning discharges observed during SDS Phase-I. Figure 5.2 shows the dipole electrode between the EGun and main spectrometer. The electrode spans 10 cm down the beamline and is contoured to fit along the beamline tube by roughly 40° of the inner radius. As will be discussed in Section 5.2.1, using the dipole electrode reduces the rate differences between taking data in up mode and down mode.

Investigating and understanding the dipole electrode and related effects will be of further use to KATRIN as an identical dipole electrode will be deployed between the pre-spectrometer and

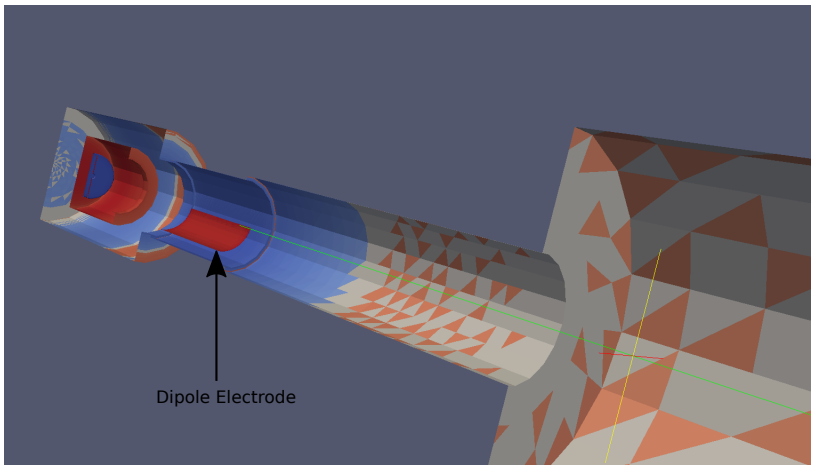

Figure 5.2: Simulated EGun geometry with dipole electrode. The section of beamline pointed at in this figure was added in between commissioning phases to reduce the effect of Penning Discharge. This cutaway shows the EGun electrodes to the left and entrance to the main spectrometer to the right.

main spectrometer during neutrino mass measurements in order to eliminate potential trapping of electrons in this region. Therefore, an analytic model of charge accumulation and thus the hysteresis effect on the transmission function should prove valuable for the eventual tritium measurements.

5.2 Analytic Model of Hysteresis in Transmission Function

As stated above, one possible source of hysteresis in the transmission function is the release of trapped electrons from the previous "step" in the transmission function measurement. For any given point in the measurement, reflected electrons can be trapped between the EGun backplate potential and the analyzing potential. Over sufficiently long measurement times the number of electrons in the trap reaches equilibrium. Adjusting the trapping potential by changing to a new backplate potential causes electrons from the previous setting (measurement) to exit the trap. Therefore, at each point in the transmission function, the number of observed electrons can contain a fraction from the previous point which generates hysteresis.

The trap in the commissioning measurements is formed by the EGun backplate and the analyzing electrodes. Figure 5.3 shows the electrostatic potential along the center of the beamline. Electrons created at the EGun backplate thus have energy close to the analyzing potential. Assuming that the fields are sufficiently symmetric, then for a given potential setting, the number of electrons entering the trap is equal to the amount reflected. Calculating the rate of electrons entering and exiting the trap and thus the rate that contributes to hysteresis would then be a quantifiable method of evaluating the hysteresis and the impact of the dipole electrode on reducing the trapped electrons.

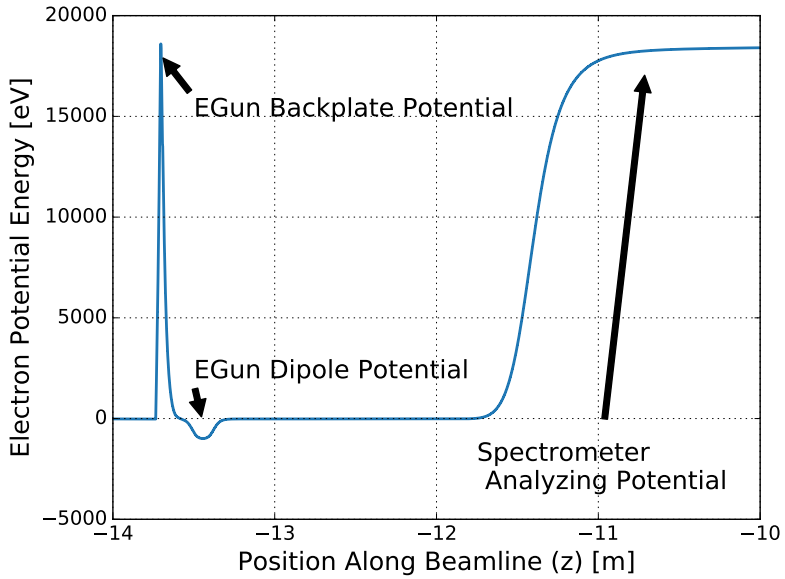

Figure 5.3: KATRIN commissioning potential map calculated using KEMField. The electrostatic potential here is given as a function of beamline position along the axis of symmetry, $r = 0$. The analyzing plane is at $z = 0$. The potential is labeled at points by the major contributors to the potential.

To calculate this number, the transmission function developed as a part of Stefan Groh's thesis[40] will be used. Equation 5.2.1, as previously shown in Section 2.4, is the transmission ratio as a function of an initial phase space density, $f(\theta_{pch}, E_e)$, where θ_{pch} is the initial pitch angle of the electrons and E_e is the initial energy of the electrons. For a given energy, θ_{max} is the limit of the pitch angle that is allowed to transmit as a function of the source magnetic field, B_S, analyzing magnetic field, B_A, and initial energy. This value, θ_{max}, is shown in Figure 5.4, and can be thought of as a weighting factor for energies which permit transmission above the analyzing potential, U_0.

$$T = \int_{U_0}^{\infty} \int_{0}^{\theta_{max}} f(E_e, \theta_{pch}) d\theta_{pch} dE_e \tag{5.2.1}$$

$$\theta_{max} = arcsin\left(\sqrt{(E_e - qU_0)/E_e \frac{B_{min}}{B_{max}}}\right) \tag{5.2.2}$$

In order to calculate the possible fraction of electrons that are reflected and then trapped, the reflection ratio must be calculated. The reflection ratio is the logical inverse of the transmission function, or the fraction of electrons with longitudinal energy below the analyzing potential. Equation 5.2.3 shows this reflection function. As the measurable in this case is the rate at the detector and the source of electrons may have some additional time dependency, the more useful function

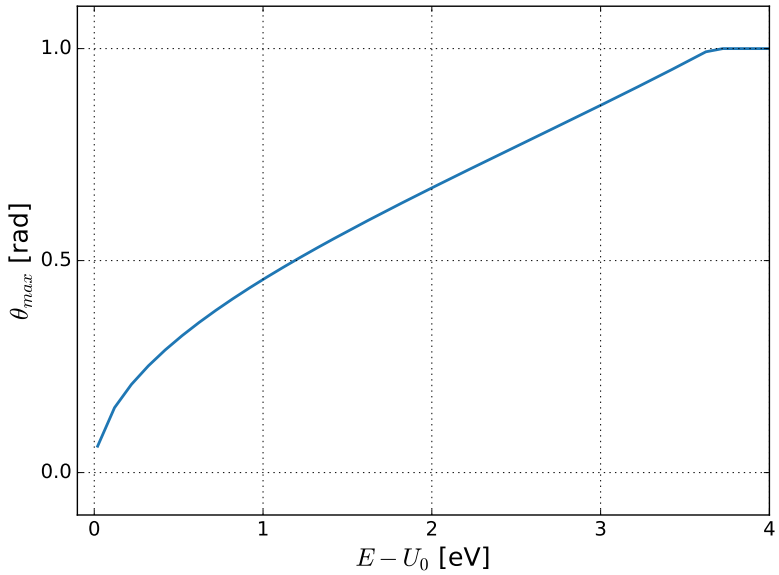

Figure 5.4: Maximum transmission angle as a function of initial energy.

would be a reflection *rate*.

$$R = \int_0^{U_0} \int_0^{\theta_{max}} f(E_e, \theta_{pch}) d\theta_{pch} dE_e \tag{5.2.3}$$

To express this as a rate, the time dependency needs to be included. The initial phase space, $f(\theta_{pch}, E_e)$ is the time-independent probability density function and can be related to the initial current density function, $c(E_e, \theta_{pch}, t)$ by integrating with respect to time. For the case of a totally time independent probability density function, the current density is the probability density multiplied by the input rate of electrons. As the integral is otherwise time-independent, differentiating the left hand side of the equation simply results in the reflected rate as expressed in Equation 5.2.4.

$$\Gamma_{refl}(t) = \int_0^{U_0} \int_0^{\theta_{max}} c(E_e, \theta_{pch}, t) d\theta_{pch} dE_e \tag{5.2.4}$$

Assuming all the electrons that are reflected become trapped, this figure, $\Gamma_{refl}(t)$ is also the trapping rate, $\Gamma_{trap}(t)$. For a sufficiently symmetric system, this is a valid assumption as no other mechanism exists for trapping or releasing electrons prior to the introduction of the dipole field later in this chapter.

If the backplate potential is changed, then the electrons' potential energy will also change. For a

potential change of ΔE, electrons with energy, $E+\Delta E > U_0$ are allowed to transmit to the detector. Therefore, in order to calculate the fraction of electrons from the rate in Equation 5.2.4 that can transmit in a subsequent measurement, one must calculate the probability that an electron is at a given potential, $p_{shift}(U)$. As the fields can be approximated to be periodic, then following classical mechanics for a simple harmonic oscillator[76], the probability density function of a particle being in a potential U is the function, $p_{shift}(U)$, is defined in Equation 5.2.5. This equation is also plotted in Figure 5.5.

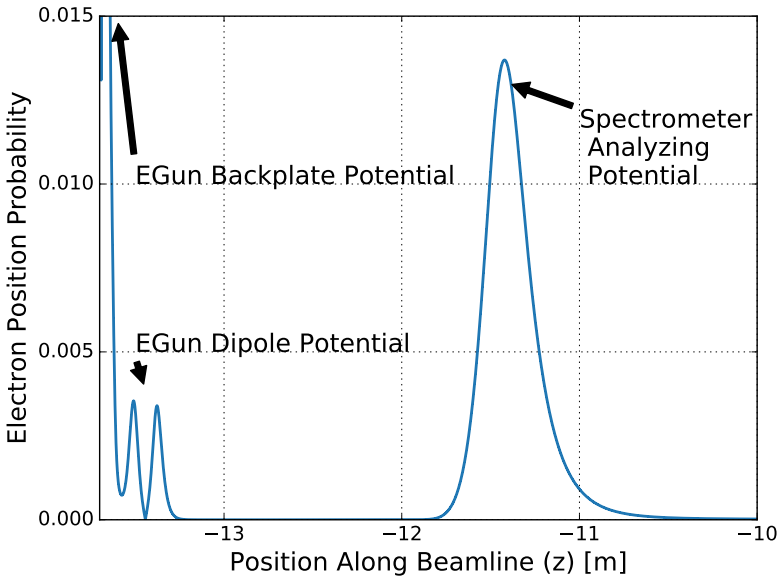

Figure 5.5: Trapping probability as a function of position for electrons generated between the EGun and Main Spectrometer potentials in the center ($r = 0$) of the beamline.

$$p_{shift}(U) = \sqrt{\frac{1}{U_0}}\frac{dU}{dz}z^{-1}(U) \tag{5.2.5}$$

The potential probability is characterized by depth, U_0, the first derivate of the potential along the beamline, dU/dz, and the functional inverse of the potential along the beamline, $z^{-1}(U) \equiv (U(z))^{-1}$. Therefore, when the backplate potential is changed by potential energy, ΔE, the probability that an electron is changed above the analyzing potential is the probability that an electron is at potential energy, E. Equation 5.2.6 shows this number as a release rate, $\Gamma_{release}$.

$$\Gamma_{release}(t, \Delta E) = \int_0^{U_0-\Delta E}\int_0^{\theta_{max}} c(E+\Delta E_e, \theta_{pch}, t)p_{shift}(E_e)d\theta_{pch}dE_e \tag{5.2.6}$$

This value can also be thought of as the initial rate of electrons trapped during point E_e in the

transmission function and subsequently released at point $E_e + \Delta E$ without any additional release mechanism. Since the trap is not an infinite number of electrons, this is only valid as the initial rate and can be expected to exponentially fall off as a function of time. For the standard measurement time of 10 s, this therefore requires that this rate is sufficiently large. Using Equation 2.7.2 and inserting the appropriate values for the region confined by the EGun and analyzing potentials, the maximum number of electrons in the trap is on the order of 10^{11} in the 0.01 m^3 region. For these measurements, the rate at which electrons are injected into the system is on the order of 10^6 *cps*. Therefore, for small measurement times, this requirement is valid. Similarly, this model will work best in the center of the beamline as the fields are more uniform in this region.

5.2.1 Dipole Electrode Effect

Adding in a dipole electrode causes the trap to empty, thereby reducing charge accumulation. The rate of reduction is described by the time constant in Equation 2.8.38. For simplicity's sake, the initial position and final dipole potential are assumed to 0, or $x_0 = 0\,m$, $U_0 = 0\,V$.

$$\tau = \frac{r^2 B\ cos(\theta_{pch})}{\gamma U_d} \tag{5.2.7}$$

To calculate the emptying rate, first consider the total number of electrons in the trap, $N_{trapped}$, which is obtained by integrating the rate up to some time, t'.

$$N_{trapped}(t') = \int_0^{\theta_{max}} \int_0^{U_0} \int_0^{t'} \left(c(\theta_{pch}, E_e, t)\right) d\theta_{pch} dE_e dt \tag{5.2.8}$$

The probability that an electron is in the trap is the probability that an electron falls in the trap and is not released by the dipole electrode. In other words,

$$N_{trapped}(t') \rightarrow N_{trapped}(t')(1 - e^{-t'/\tau}) \tag{5.2.9}$$

In other words, the number of electrons impacting the side of the beamline should be proportional to the number of electrons in the beamline and thus follows a decay law. Differentiating the previous equation with respect to time results in the following:

$$\Gamma_{trapped}(t) = \int_0^{\theta_{max}} \int_0^{U_0} \left[(1 - e^{-t/\tau})c(\theta_{pch}, E_e, t) - \frac{e^{-t/\tau}}{\tau} \int_0^t c(\theta_{pch}, E_e, t')dt'\right] d\theta_{pch} dE_e \tag{5.2.10}$$

An immediate consequence of the above equation is the characteristic filling time of the trap. Namely, during the time, t when $c(E,\theta,t) \approx e^{-t/\tau}/\tau$. Prior to the previous condition being satisfied, the trap fills faster than the dipole electrode can empty it. Naturally when the dipole electrode exceeds this condition, the trap is emptying at the same rate or faster than it is filling. Once again, this is expected to drop off exponentially as a function of time.

Now consider that the trap has sufficient time to fill. Following the prescription for calculating the probability density for electrons over a given energy, the rate of electrons that are released into the beamline is:

$$\Gamma_{released}(t,\Delta E) = \int_0^{\theta_{max}} \int_0^{U_0-\Delta E} p_{shift}(E) \Big[(1-e^{-t/\tau})c(\theta_{pch}, E_e+\Delta E, t) - \frac{e^{-t/\tau}}{\tau}\int_0^t c(\theta_{pch}, E_e+\Delta E, t')dt'\Big] d\theta_{pch} dE_e \quad (5.2.11)$$

Equation 5.2.11 is the rate at which electrons exit the trap due to raising the backplate potential with the dipole electrode added. Electrons exiting the trap discharge towards the lower potential. For raising the EGun potential relative to the analyzing potential, the electrons are expected to impact the detector. Similarly, lowering the potential is expected to discharge the electrons away from the detector. This is congruent with the observation that over the course of the run schedule, the EGun surface was seen to degrade [73]. The direction of emission from the trap also means that the hysteresis in the transmission function is almost entirely contained in the transmission functions taken in the "up" direction, while the "down" direction should have none of the effects.

To fully consider the effects of measuring up or down the transmission function, the sequence of voltages and times needs to be considered. If the sequence is parameterized by the index i, then U_i is the EGun backplate potential for measuring point i on the transmission function. Similarly, t_i is the time at which the ith measurement begins, and for convenience $t_1 \equiv 0$. The final term in Equation 5.2.11 can then be broken into segments to account for charge accumulation from all previous measurements for measurement j,

$$\Gamma_{released,j}(t,\Delta E) = \int_0^{\theta_{max}} \int_0^{U_0-\Delta E} p_{shift}(E) \Big[(1-e^{-t/\tau})c(\theta_{pch}, E_e+\Delta E, t) - \sum_{i<j}\frac{e^{-(t-t_i)/\tau}}{\tau}\int_{t_i}^{t_{i+1}} c(\theta_{pch}, E_e+i\Delta E, t')dt'\Big] d\theta_{pch} dE_e \quad (5.2.12)$$

Equation 5.2.12 is the rate excess produced by the trap when measuring up the transmission function. This model can be tested against the data from SDS phase-I by taking the rate difference at U_0 where the rate is roughly $10\,kHz$ as shown in Figure 5.1. Assuming a field inhomogeneity on the order of 0.01%, and an isotropic source Equation 5.2.12 provides a rate excess of roughly 1 kHz, which agrees with the rate excess shown to within an order of magnitude.

For more rigorous testing, this model can be used to fit against transmission function excess as a function of dipole electrode strength. The dipole electrode potential can then be optimized for systematic error in the neutrino mass measurements.

5.2.2 Analytic Model Evaluation

Given that Equation 5.2.12 describes the rate excess analytically for simple situations, this equation can be used to evaluate what is expected in the simulations and measurements. Thus, a sanity check can be performed on the SDS Phase-I data. This provides the guiding method for testing the model against the SDS Phase-II data.

In order to use the model, an initial current density function needs to be defined. For this calculation, Stefan Groh's model[40] was used with a Gaussian energy spread and isotropic spread of electrons.

$$c(E_e, \mu, t) = \Gamma_{ave} Norm(E_e - \mu, \sigma_e) cos(\theta) \tag{5.2.13}$$

Here, Γ_{ave} is the average rate produced by the EGun. For this model, μ and σ are the mean energy and the full width at half maximum of the initial distribution of electrons. This choice of current density function has the advantage that it simplifies the time dependence in Equation 5.2.12. Since the current density function is independent of time, the number of electrons released is dominated by the dipole reduction term and thus results in Equation 5.2.14. As the integrals cannot be evaluated analytically, in order to use this model, $\Gamma_{released}$ must be evaluated using numerical integration techniques.

$$\Gamma_{released}(t) \approx \int_0^{\theta_{max}} \int_0^{U_0 - \Delta E} p_{shift}(E) e^{-t/\tau} c(\theta_{pch}, E_e + \Delta E, t) dE_e, d\theta_{pch} \tag{5.2.14}$$

The blue curve in Figure 5.6 shows the analytic transmission function without charge accumulation effects. Due to the directionality of the discharge of electrons from the trap, this is expected to correspond to transmission functions taken in the down mode. For the up mode transmission functions, the values with charge accumulation are plotted for three separate dipole voltages. The

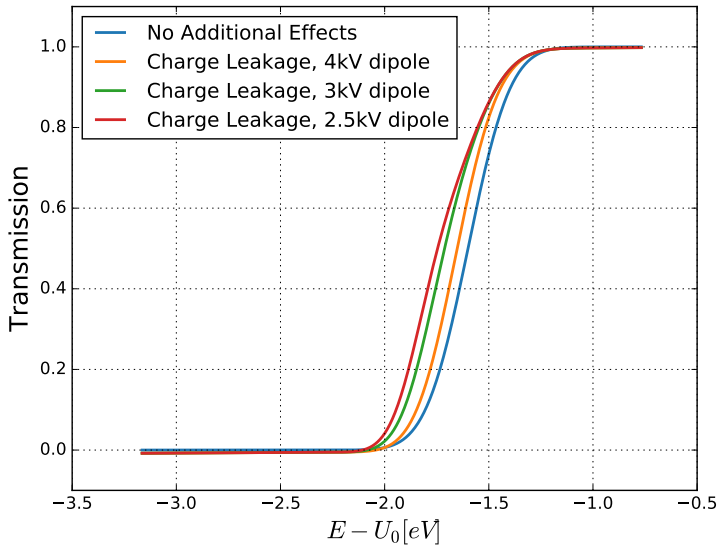

Figure 5.6: Analytic Transmission Function. In Blue is the case of no charge leakage. This also corresponds to electrons hitting the backplate on the EGun. The other curves show the transmission functions for charge accumulation at various dipole voltages

value for the time constant for dipole reduction was taken from the simulations in Section 5.4. In addition, the field values used in the integrand are taken from slow controls readback for the later measurements.

Data from SDS Phase-I can be used as a preliminary validation for the model. The shape of the deviation between transmission functions agrees with the data from SDS Phase-I. Therefore, it's possible for this model to explain the data, but in order to elucidate the dipole electrode's reduction on the deviation, further measurements will be described later in this chapter.

The contribution of charge accumulation to the rate at a single point in the transmission function can be computed as the difference between the up and down mode transmission functions. As the down mode transmission function is simply the transmission function without charge accumulation, the rate from accumulated charge is the rate difference, or *residual*, between the up mode transmission function and the charge accumulation-less transmission function. Figure 5.7 shows the residuals for each of the dipole voltages in Figure 5.6. The effect of the dipole electrode is visible in the change in amplitude of each residual "bump." Residuals will be acquired in simulations and measurements and fit to this functional shape to quantify the detected rate from charge accumulation and subsequent dipole reduction.

Since the functional form of Equation 5.2.12 will be used to fit both data and simulations, illustrating the impact of each parameter in this equation helps to justify the shape of the fits.

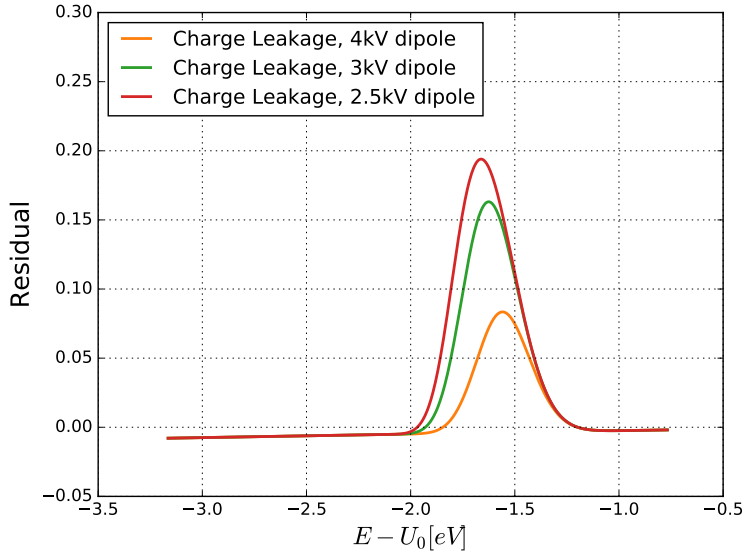

Figure 5.7: Analytic transmission function excess for several dipole voltages. Each point is calculated as the difference in transmission functions for charge accumulated and non charge accumulated models.

The simplest of these parameters is the mean rate, Γ_{ave} in equation 5.2.13. Figure 5.8 shows three separate transmission function residuals for the nominal dipole voltage setting. The major change between the curves in this figure are the amplitudes of the residuals. In comparison to Figure 5.7, this parameter has a greater impact on the transmission function rate than the dipole reduction for an order of magnitude change in input rate. Therefore, in the measurement, it will be important to ensure a constant input rate.

The mean energy of the EGun is introduced in the charge density function in Equation 5.2.13, and is used as a fit parameter. Figure 5.9 shows that this shifts the location of the peak of the residual. Since the mean energy of the electrons is a fit parameter, the variance is a fit parameter as well. Figure 5.9 shows that this introduces a skew in the transmission function residual. This skew is due to the transmission function truncating the tail of the current distribution function and thus the direction of the skew is also dependent on the mean initial energy.

A prominent feature of these curves is the apparent covariance between parameters in the model. This is seen in Figure 5.9 where both the mean and width of the initial distribution shift the centroid of the residual. The reason for this is the width of the initial distribution increasing to outside of the integration window. Thus, care will have to be taken in the fits to ensure that the parameters are being fit properly.

To summarize the charge accumulation and dipole emptying model, the following assumptions

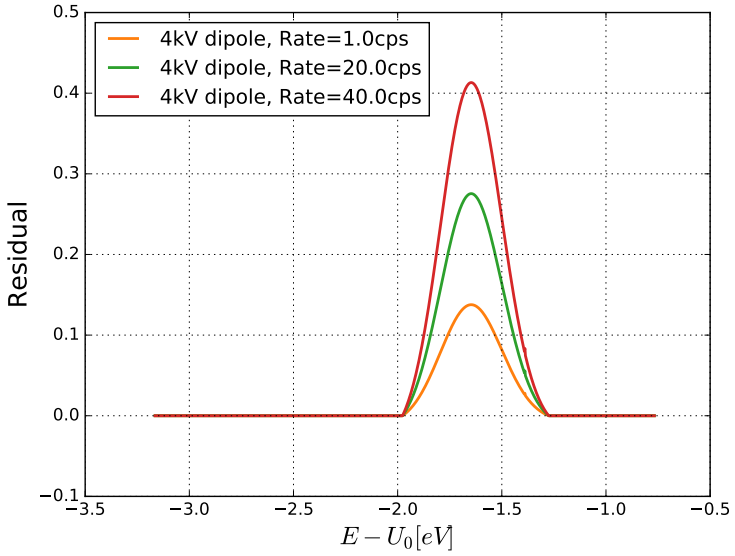

Figure 5.8: Mean rate impact on transmission function electron excess rates. The nominal dipole voltage value of 4 kV was used to create plots as a function of input rate. Equation 5.2.12 shows that the mean rate should increase the amplitude of the residual on each point of the transmission function identically. This makes the mean rate covariant with the dipole electrode parameter, and they can be differentiated by the change in skewness of the plot.

have been made:

1. All electrons that are reflected are trapped.

2. The trap emptying time is much longer than the measurement time.

3. Electrons are either ejected from the trap by the dipole electrode or are transmitted to the detector.

    - The mean free path for an electron is on the order of 1 km for KATRIN, and thus this is a valid approximation.

4. Electrons are trapped by potentials approximately equivalent to the potential well in the center of the beamline.

    - The EGun produces electrons with Larmor radius on the order of 1 μm when held on axis. The difference in analyzing potential between the center of the beamline and this radius is on the order of 0.1 μV. Thus, this is a valid argument for the EGun aimed on axis. However, off axis this assumption loses validity and so the EGun will be kept on axis for the transmission function measurements.

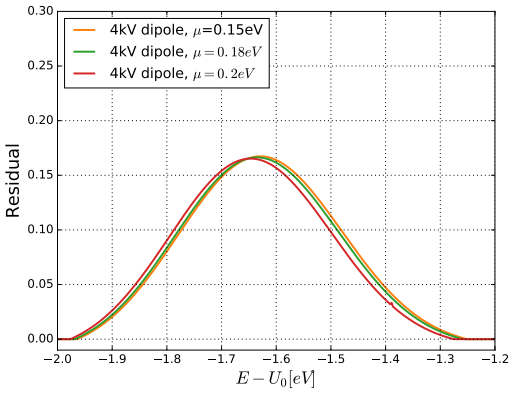

(A)

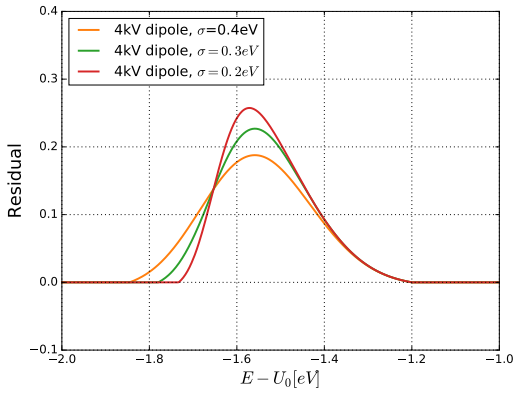

(B)

Figure 5.9: Energy distribution impact on residual fits. The nominal dipole voltage value of $4\,kV$ was used to create plots as a function of energy. (A) The transmission function residuals as a function of mean electron energy. (B) The transmission function residuals as a function of EGun line width. The skewness is due to a portion of the electron initial energy spectrum being truncated by the integration limits in Equation 5.2.14. The change in position makes these parameters covariant. In addition, the change in skewness due to the width of the transmission function is covariant with the dipole parameter. These can be differentiated by the change in amplitude and position without skew.

5. The mechanism for electrons from one point in the transmission function measurement to introduce rate into another measurement point is dominated by shifting electron energies with the backplate potential.

    - Once again, the validity of this argument is tenable as the analyzing potential is not uniform across the radius of the spectrometer. This necessitates using on-axis measurements with the understanding that some error will be introduced by electrons changing radii due to the dipole electrode and therefore a different analyzing potential.

The physical interpretation of the dipole effect on the shape of the transmission function is that deviation from a "normal" transmission function is due to charges released by changing a trapping potential. In the non-transmitting region, the shape is not expected to deviate since changing the trapping potential from one non-transmitting potential another non-transmitting potential does not produce transmitting electrons. Similarly, in the high transmission region, the deviation from the normal transmissions function should be negligible due to lack of reflecting electrons. In the lower side of the transmission region (say, below 50% transmission, for example), deviations should be due to the rate reflected from the previous point. Inversely, in the higher side of the transmission function, increased rate should be from accumulated charge from many of the lower points. Changing the dipole electrode should therefore change the deviation from the lower side of the transmission

function to the higher side.

Interpreting the shape of the residuals can be broken into the same pieces. In both the non-transmission and full-transmission regions of the transmission function, the residuals should be constrained to 0 *cps*. As the transmission function increases above the no-transmission point, the model over-predicts the transmission function by a factor corresponding to the reflection from the previous point. At some point in the transmission function, the number of electrons becoming trapped and those released towards the detector becomes equal[1]. Above this point, the model still over-predicts the rate due to accumulated charge, but this tails off as the number of reflected electrons decreases with increasing transmission. The location of the equilibrium point depends on the competing trapping and release rates, and should shift to a higher point with increasing dipole voltage. This is due to the impact the dipole voltage has on trapped electrons and not the trapping rate. The exact width of the residuals should be dependent on the width of the initial distribution and the electromagnetic field strengths. Thus the shape of the residuals should be a skewed Gaussian with a width fixed by the apparatus and peak position and skew due to the mechanics of the trap.

5.3 Measurement of Charge Accumulation

In the second SDS commissioning phase, this model was tested by obtaining transmission functions for a pre-defined set of dipole voltages. In order to fully utilize Equation 5.2.12, a full transmission function measurement was taken in "up" mode and another in "down" mode for each dipole voltage. To investigate error in this measurement, a third data set was taken in "Pseudo-Random" mode, which was intended to test the hypothesis against random points.

5.3.1 Method

Using the KATRIN run numbering system, the dipole voltages chosen in this study and the corresponding run numbers are detailed in Table 5.1. The dipole voltages were chosen to span a "safe" range defined by the dipole electrode power supply and observed Penning discharge. The dipole electrode is limited by the power supply to 4kV maximum and as Penning discharges were observed previously below 100V, the runs were limited between these two values. While more dipole voltage settings are desirable in order to find more comparisons, this dissertation was also limited to 6 hours of data taking time allocated with the KATRIN apparatus.

To investigate the Penning trap model, the transmission function measurements were repeated

[1] It should be noted that electrons that are trapped but not emitted towards the detector are incident on the walls of the spectrometer.

for a number of dipole voltages. For each dipole voltage three data sets were taken. Similar to the previous measurement, one data set per direction (up and down) was taken. In addition, a third data set taken with measurements with quasi-random steps instead of definite direction. The data from the quasi-random runs is omitted from this study as the noise in the slow controls data rendered these runs not useful. This is detailed in Table 5.1.

Dipole Voltage[kV]	Up Data Run	Down Data Run	Quasi-Random Runs
4.0	23408	23409	23411
3.5	23403	23404	23406
3.0	23393	23398	23400
2.5	23414	23415	23421
0.5	24104	24105	24107
0.1	24110	24108	24111

Table 5.1: Run numbers for the Penning trap data taking runs.

Within each data set, the backplate voltages were stepped over the transmission range with the analyzing potential kept at $18.6kV$. Table 5.2 shows the backplate voltages used in this measurement. These values were identified by running a binary search algorithm to determine the 50% level in the transmission function, then choosing 9 points in either direction. These values are kept static between runs to aid in comparing data sets. The 50% level corresponds to point 11. Points 12-20 correspond to the higher transmission region with points 2-10 corresponding to low transmission.

An additional data point was taken at index 1 for normalizing the transmission function by dividing each value in the transmission function measurement by this additional value. However, the high rate effects shown later this chapter show that using this point as a normalizing value is invalid. Therefore, for the measurements shown in this chapter, this point will not be used.

The EGun was kept positioned as close to the center of the beamline as possible with close to zero pitch angle. This will make validating the model easier due to the fact that the model assumes symmetric fields which is valid in the center of the beamline.

5.3.2 Rate Acquisition

For the rate measurement, a single pixel on the detector was chosen to study this effect as the EGun angular distribution is small enough to cover a fraction of one pixel when aimed down the center of the beamline. The pixel of choice was pixel # 4 on the detector. This corresponds to the upper right quadrant of the center of the detector.

Backplate voltage is measured using the multimeter mentioned in Section 4.2.1. Values are

Index	Backplate voltage[V]
1	-3.16
2	-2.56
3	-2.46
4	-2.36
5	-2.26
6	-2.17
7	-2.07
8	-1.96
9	-1.86
10	-1.76
11	-1.67
12	-1.57
13	-1.46
14	-1.36
15	-1.26
16	-1.17
17	-1.07
18	-0.96
19	-0.87
20	-0.77

Table 5.2: Backplate voltages used in Penning trap study.

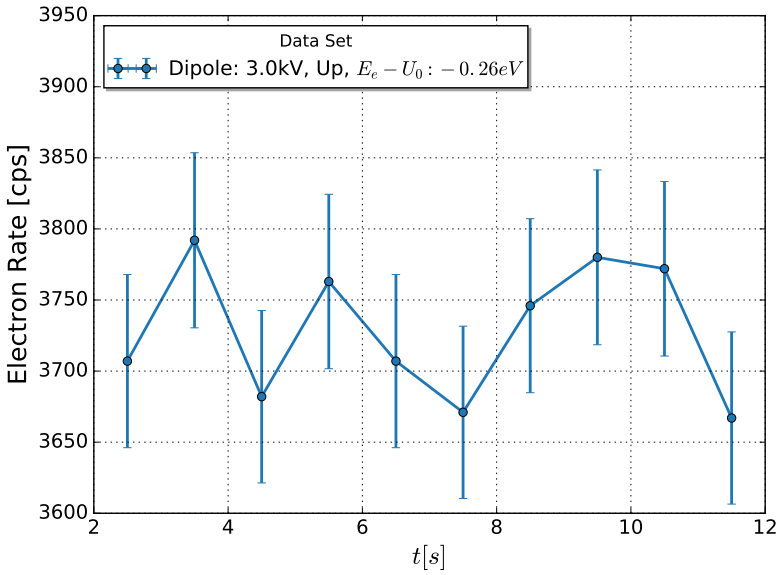

Figure 5.10: An example of a rate measurement for a dipole voltage of 3.0 kV at the $E_e - U_0 = -0.26\,kV$ transmission point.

reported from the EGun system to the KATRIN slow controls database[77]. In the analysis for this measurement, the values are computed as the algebraic mean of the available values with the error in each as the linear variance.

Similar to the analytic model, in the measurements one can assume that the rate as a function of time is constant. This was tested by calculating the mean and variance for each of the data points. If the rate is constant, then the errors should follow Poisson statistics and be equivalent to the square root of the rate. This test was performed on each of the data points and showed that the rate is constant. Figure 5.10 shows the rate over the 10 s measurement period. Each point represents 1s worth of data and the associated variance of the rate during that time. As the mean rate does not significantly change and the variance follows Poisson statistics the approximation that the rate is constant over the 10 s measurement period is valid.

Rate Pileup

Due to the high electron rate at the detector, pileup in the electronics needs to be addressed. Sanshiro Enomoto[64] showed that if two electrons are coincident within the filtering time window, the energy is adjusted into a higher region of interest. Therefore the true rate at the detector is calculated by double counting the region of interest for double electron pile up, triple counting for three electron groups, etc. This calculation is reflected in Equation 5.3.1, where N_{true} is the true

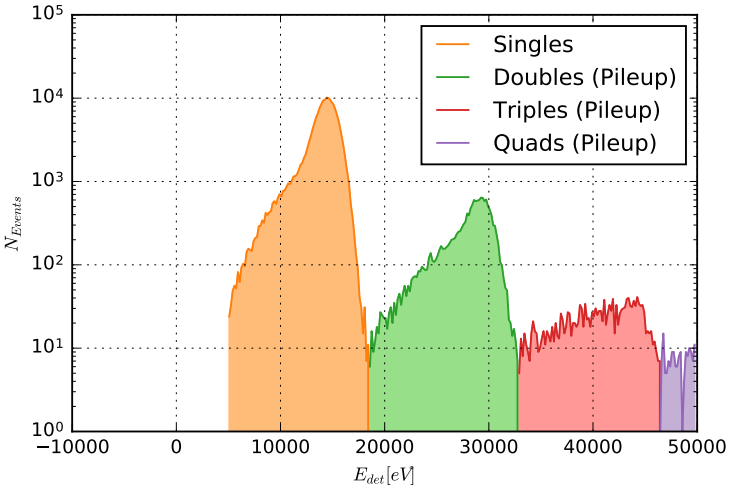

Figure 5.11: Energy spectrum of electrons on the detector. This is subdivided into pileup regions. Each region corresponds to an integer number of electrons coincident on the detector. The total rate at each point in the transmission function is calculated as the total number of electrons weighted by the number in each pileup group.

rate, i is the number of coincident electrons and N_i is the number of counts is the electron peak that corresponds to i. Figure 5.11 shows the different regions and the adjustment factor for each, where the single electron peak is at $10\,kV$ due to the setting on the post acceleration electrode.

$$N_{true} = \sum_i i \cdot N_i \tag{5.3.1}$$

The pileup at the detector is of critical importance as the charge leakage effect at $0.1\,kV$ dipole voltage corresponds to a 10% effect while the pileup effect corresponds to a 1% effect at the higher rate values in the transmission function.

For the remainder of this study, the $0.1\,kV$ measurement mentioned previously will be excluded. This was the last measurement in the scan and the rate was observed to have been much higher and unstable than the other measurements and lacking in the shape that defines the transmission function.

5.3.3 Measured Transmission Function

For the measurements of the electron rate, the transmission functions are defined as the electron rate on the detector as a function of backplate voltage. An example is shown in Figure 5.12A where the estimated EGun output rate was roughly $15000\,cps$. These data points were taken at $0.5\,kV$ on the dipole electrode and the rate difference is visible on the order of 10%.

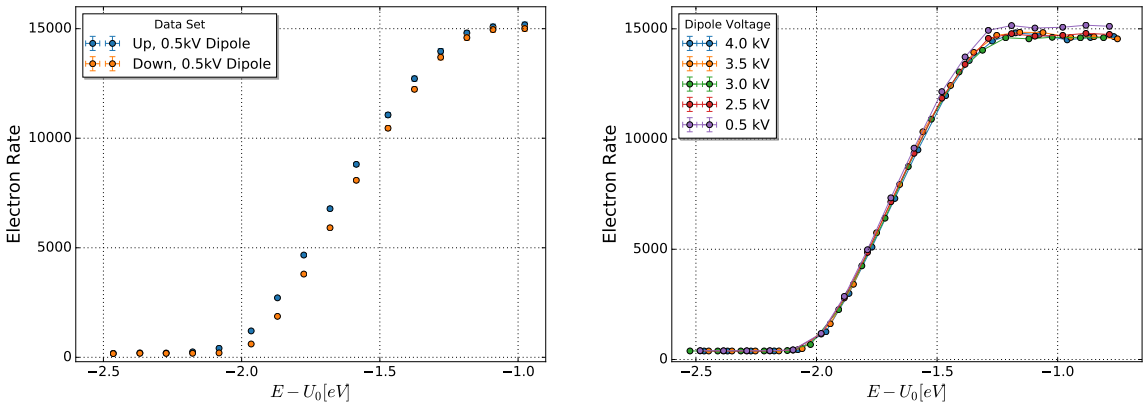

(A) (B)

Figure 5.12: (A)Example Transmission function for $0.5kV$ on the dipole electrode. The orange points are measured in increasing the backplate voltage and the blue points are measured by decreasing the backplate voltage. (B) The down mode transmission functions for each of the dipole voltages used in the measurement. Note that the $0.1\,kV$ measurement is not shown on this plot. This is due to a much higher input rate.

The reason for choosing to represent these values as raw rates instead of as transmission ratios is error treatment. Calculating the transmission ratios requires the mean rate and variance for both input rate and detected rate. While the detected rate statistic is simple to compute, the input rate requires a value for the error in the input rate, which was not obtained. As the goal is to fit the model of charge accumulation, the transmission ratio is not necessary and therefore the raw rates will be used. For the case of Figure 5.12A, the size of the error bars is much smaller than the radius of the point markers representing the data.

One of the immediate consequences of Figure 5.12B is the uniformity of the down data sets. The fact that there is very little deviation between the data sets shows that the cause of the hysteresis must arise in the up mode data sets only. This verifies the prediction in the model that electrons emitted from the trap are detected only in the up direction.

5.3.4 Residual Rate Calculation

Following the same procedure as the analytic calculations, the differences, or residuals, between up and down data sets were taken. Figure 5.13 shows the residual rate at each point in the transmission function labeled by dipole electrode potential.

Errors in these points are calculated by propagating the uncertainty from the detected rates. For a single point, the uncertainty in the residual, σ_r is calculated as follows, for the uncertainty in the up data point, σ_{up}, the uncertainty in the down data point, σ_{down}, and the covariance, $\sigma_{up,down}$.

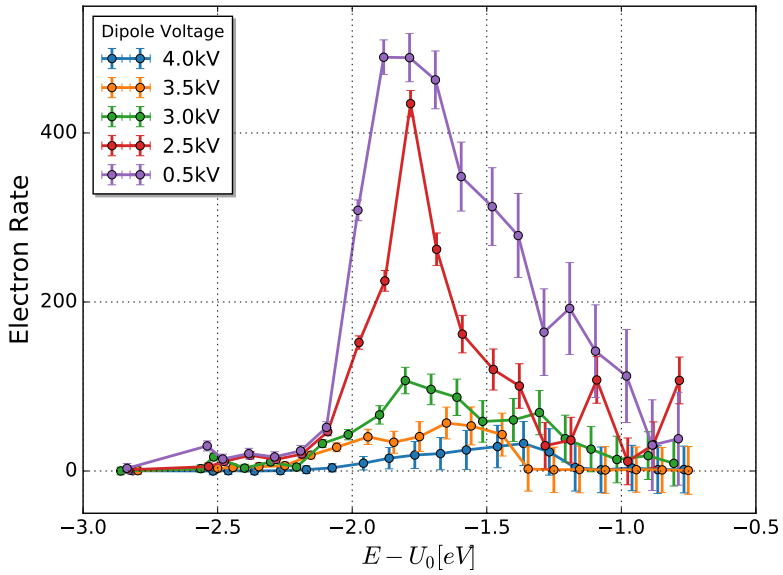

Figure 5.13: Dipole measurement residuals. Each data set is colored by dipole voltage used. Points represent the difference between the corresponding points on the "up" and "down" data sets.

$$\sigma_r^2 = \sigma_{up}^2 + \sigma_{down}^2 - 2\sigma_{up,down} \tag{5.3.2}$$

While Figure 5.13 shows a similar functional form to the analytic model, there are a few discrepancies. In the $E - U_0 > -1.4\,eV$ region, the errors increase in size and the rates no longer follow the dipole voltage as a trend. This could indicate that the trapping time is becoming competitive with the ejection time.

In order to further investigate these discrepancies, the model will also need to be compared against the simulation.

5.3.5 Fitting Rate Excess

The next step in measuring the effect of charge accumulation is to fit the data to the model. The model in question is Equation 5.2.12 and the goal of fitting is to find the dependence on the dipole electrode constant, τ. Since τ depends on the initial pitch angle, an angularly averaged time constant is used instead as shown in Equation 5.3.3.

$$\overline{\tau} = \frac{r^2 B}{\gamma U_d} = \tau / cos(\theta) \tag{5.3.3}$$

As stated previously, the model must be evaluated numerically. Therefore, the function that

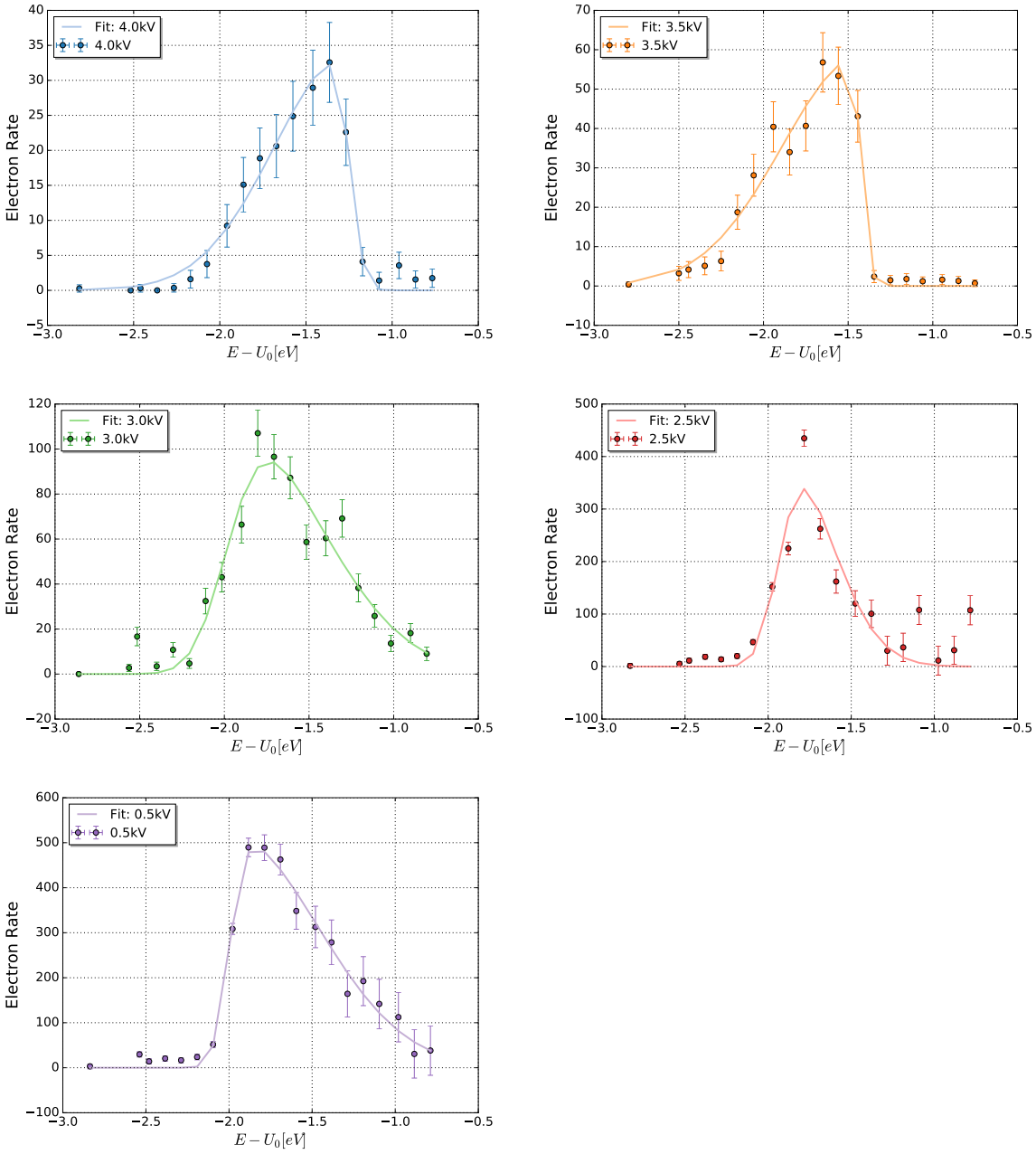

Figure 5.14: Individual Measured Transmission Function Residuals. Here the transmission functions are colored and labeled by dipole voltage. Note that the y-axis for each plot is different due to the difference in amplitude in each residual.

is fit is the numerical evaluation of Equation 5.2.12 as a function of $\bar{\tau}$ and additional variables. The additional variables in question are the mean rate, Γ_{ave}, the mean initial energy, E_e, and the variance in initial energy, σ_e. The mean rate was chosen as a fit parameter since although the rate was observed to be constant within a single data set, using rate as a fit parameter allows for change between data sets. Likewise, the mean initial energy and variance were chosen due to the observation that some of the skew in the model is evident in the residuals. The physical mean energy and variance are not expected to vary significantly over the course of the measurement, so the expectation is that additional effects on the transmission function a function of dipole voltage can be parameterized by these values. Therefore, this allows the model fits to probe the dependence of the measurements on observed initial energy and variance.

Since the measurements were taken in $10\,s$ intervals, the time step variables are set to this value, $t_1 = t_2 = 10\,s$. Mis-estimation in this parameter will be reflected in the error of the fit of the mean rate, Γ, due to identical form in the fit function. This is acceptable as the mean rate is not the desired fit parameter.

For this study, a Levenberg-Marquardt algorithm[78] was used in the scipy *curvefit* package[79]. The resulting fits are shown in Figure 5.15.

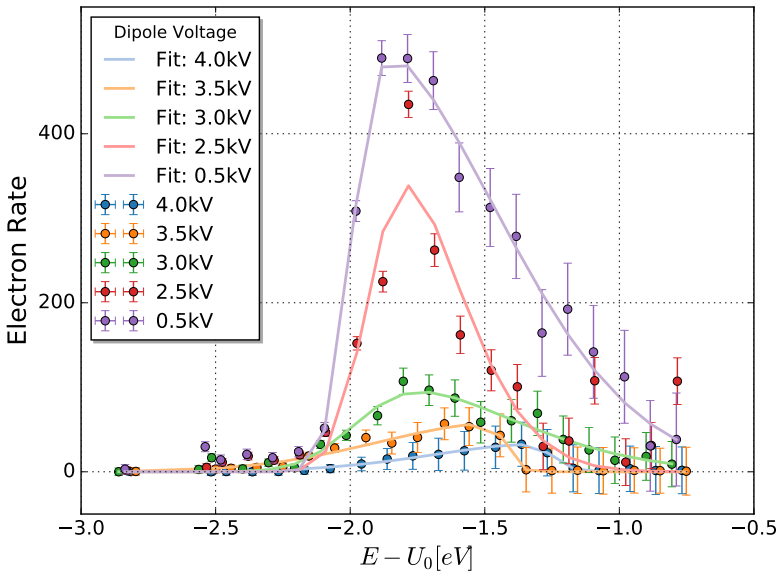

Figure 5.15: The data from the dipole measurements represented in points with the fitted values displayed with lines.

Table 5.3 shows the results of fitting these points to the model. From this table, one can conclude that the fitted model becomes a better descriptor at high dipole voltage values. This conclusion is

U_d[kV]	χ^2	P-Value	$\Gamma_{ave}[kcps]$	$E_e[eV]$	$\sigma_e[eV]$	$\overline{\tau}[s]$
0.5	25.99	0.08	16.70 ± 5.22	1.99 ± 0.01	0.18 ± 0.01	(0.13 ± 0.07)
2.5	31.02	0.02	15.24 ± 6.77	1.63 ± 0.04	0.22 ± 0.01	$(1.36 \pm 0.42) \times 10^{-2}$
3.0	19.11	0.26	14.75 ± 5.13	1.58 ± 0.04	0.26 ± 0.04	$(1.36 \pm 0.26) \times 10^{-2}$
3.5	13.65	0.68	14.79 ± 5.01	1.42 ± 0.01	0.28 ± 0.01	$(1.19 \pm 0.01) \times 10^{-2}$
4.0	10.86	0.87	14.88 ± 4.23	1.24 ± 0.01	0.27 ± 0.01	$(5.62 \pm 0.31) \times 10^{-3}$

Table 5.3: Fit results for measured data. Each row represents a single data set corresponding to a dipole voltage. The χ^2 value at each row is for a fit of 21 points with 4 variables for a total of 17 degrees of freedom. The mean and variance values for electron energies for the EGun are detailed in columns E_e and σ_e respectively. The dipole reduction is detailed in the column denoted by the time constant.

drawn from the decreasing χ^2 value as a function of the dipole voltage. The cause for this trend in the data is likely due to increasing error in the estimation of the dipole field at lower voltages. Since the magnetron drift induced by the dipole electrode pushes electrons to a higher radius, a significantly lower dipole voltage allows electrons to drift more slowly to an outer radius before exiting. Therefore, since the dipole potential was assumed to be identical for each pass of the electron across the dipole region, then for each pass, the mis-estimation increases. As this effect is not included in the model, this should produce worse fits as is observed in the data.

Of particular interest in the fit results table is the change of the mean over $0.07\,eV$ and variance over $0.1\,eV$ of the electron energies as a function of dipole voltage. In addition, the skew in the plots changes drastically as a function of dipole voltage. While the variance of the initial distribution is correlated with skew, the dipole constant is as well. One may assume that since the mean rate, Γ is shown to be fit to a constant value for the length of the data set, then the rest of the amplitude is correctly fit by the dipole constant and thus the remaining change in skew is due to the change in variance. Simulation will be needed to explain why this is the case.

The dipole constant, $\overline{\tau}$, will be compared against the both the simulations and the analytic model later in this chapter. A cursory inspection shows that this roughly follows a $1/U_d$ trend, which is to be expected from the model. The errors show that this parameter does not sufficiently describe the data and therefore will necessitate simulations to explore possible sources of error or shortcomings of the model assumptions.

5.4 Simulation of Trapped Particles

The expectation in developing the simulations is that while the model developed in Section 2.8 and Section 5.3 should be able to describe the data in full, the assumptions made in developing

the model might not be valid and therefore necessitate simulations. Namely, Penning discharges unmeasured backgrounds, 3D effects and electromagnetic field imperfections can cause differences in the measured transmission functions from the analytical model. Therefore, the simulations developed in Section 4.4 will be used to compare the measured data to the model.

5.4.1 Simulation Construction

The geometry and field calculations used for this measurement are identical to those used in Section 4.4. To generate particles from the EGun, a gaussian shape is used as in Equation 5.4.1,for the energy spectrum. The mean energy, μ is used to represent the excess energy imparted by the photons minus the work function of the surface material. Similarly, a cosine is used, as in Equation 5.4.2 for the angular distribution up to a maximum angle to represent a spherically symmetric distribution. This is expected at the EGun since thin film surfaces mask the angular dependence of work functions in metals.

$$f(E,\mu,\sigma) = \frac{e^{-(E-\mu)^2/(2\sigma)^2}}{\sqrt{2\pi}\sigma} \tag{5.4.1}$$

$$w(\theta) = cos(\theta) \tag{5.4.2}$$

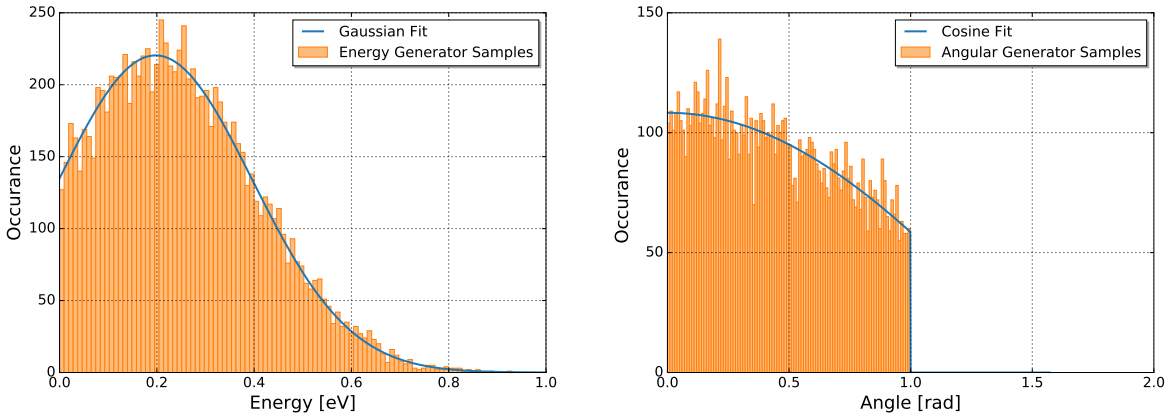

(A) (B)

Figure 5.16: The initial distribution of electrons in the charge accumulation simulation. (A) The initial energy distribution for 10000 particles in orange with a fit line for comparison in blue. For an initial energy of $0.2\,eV$, fitting the peak results in a value of $0.199 \pm 1.96 \times 10^{-3}\ eV$ with a χ^2 value of 81.54 for 96 degrees of freedom. (B) The angular distribution for 10000 particles in orange with a fit line in blue. Similar to the energy distribution fit, this fit has a χ^2 value of 95.76 for 101 degrees of freedom. In both plots the fits are to the initial distribution in Equation 5.2.13 using the same algorithm as the main function fits.

Tracks are stopped or *terminated* when they are considered no longer useful for the immediate simulation. The most commonly used terminator is the surface terminator, which stops a particle when the particle's projected motion passes through a surface. For simulations involving the dipole, this is useful as this terminator is used when the dipole ejects an electron out of the beamline. This is also used when a particle comes in contact with the detector, the main spectrometer or the EGun apparatus. Also of use to this simulation is the *trapping terminator*. This device calculates when the dot product between the momentum and magnetic field changes sign. That is, when a change in direction relative to the magnetic field is detected for step i, $sign(\vec{B}_i \cdot \vec{p}_i) != sign(\vec{B}_{i-1} \cdot \vec{p}_{i-1})$. For these simulations, this condition is relaxed to 100 iterations. This number of iterations was chosen because the dipole electrode should be able to push electrons out of the beamline before this number is reached and thus if a particle reaches 100 iterations, it is considered permanently trapped.

This terminator is utilized between runs to simulate the electron rate from each point in the simulation which effects the subsequent point. This is done for both up and down modes in the transmission function. Terminated tracks at one point in the transmission function are used in the simulation output to restart tracks in the next point. This should provide an accurate measure of the effect trapped particles have on the transmission function independent from Equation 5.2.14. Therefore, for a single transmission function point, the total rate of electrons is the rate generated by the EGun plus the rate coming from the trapped particles.

Figure 5.17 shows the number of electrons from an initial 10000 tracks which get carried over to the next point in the transmission function. The interesting point is that for the low transmission points, almost all of the tracks are terminated by the trapping terminator. For high transmission, the dipole effect is elucidated and the high rate effects can be seen as the dipole eliminates almost all trapped particles. This explains a possible discrepancy between the model and simulations as the model will always predict a positive number of electrons carried over to the subsequent point.

Once electrons are carried over to the next point in the transmission function, they are restarted with the same initial conditions except for electric potential. This way, the electric potential of the backplate electrode can be used to manipulate the electrons and produce the rate excess seen in the measurements. Effectively, this changes the electron total energy at the analyzing plane by modifying the electron potential energy at the EGun.

Since the goal of this simulation is to elucidate the effect of small variations on the guiding center of electrons, as shown in Section 2.8, tracking simulated electrons must be as precise as possible. To achieve this goal, a form of the adaptive Runge-Kutta method is used to track electrons through the EGun geometry. In particular the Dormand-Prince variation on Runge-Kutta was used and is

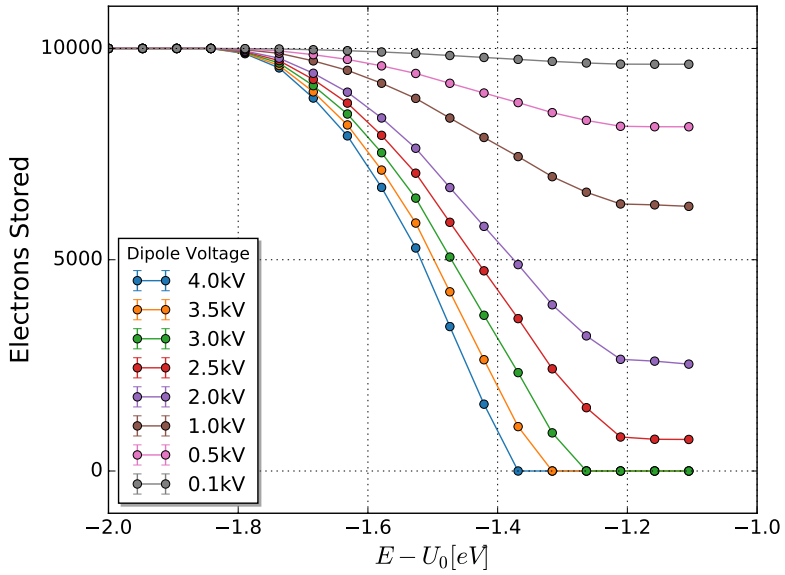

Figure 5.17: Simulated number of electron trapped at each point in the transmission function. At the end of each simulation the total number of electrons that are to be used in the next simulation are counted and displayed here. Some additional intermediate points were added in to probe dipole voltages not included in the measurements.

known for high stability in low variation calculations[80].

Slow controls data from the KATRIN slow controls database were directly injected into the simulations to recreate the data to as high precision as possible. This was accomplished by linking the simulation framework directly to the data analysis framework, and inputting the run configurations from Table 5.1. As simulations are not constrained by beamline time, additional points were chosen to increase statistics. Each of the simulations that were run used 10000 particles. The limiting factor here is the amount of time spent on the cluster.

5.4.2 Results of Simulations

At each of the points in the transmission functions, the transmission ratio was calculated. Unlike the measurements, the exact number of input particles is known and therefore the transmission ratio can be used. Transmission is defined as,

$$T = \frac{k}{n} \tag{5.4.3}$$

Where k is the number of particles that pass the detector plane and n is the number of particles generated. Here, the errors are calculated following Ullrich et al.[81]. The error per point is therefore,

$$\sigma_T^2 = \frac{(k+1)(k+2)}{(n+2)(n+3)} - \frac{(k+1)^2}{(n+2)^2} \tag{5.4.4}$$

Without Charge Accumulation

Initially, the simulations were run with the EGun generator only. The separates out any effect that the dipole electrode has on the transmission function from the effects of charge accumulation. Figure 5.18 shows the resulting transmission ratios as a function of excess energy and dipole voltage.

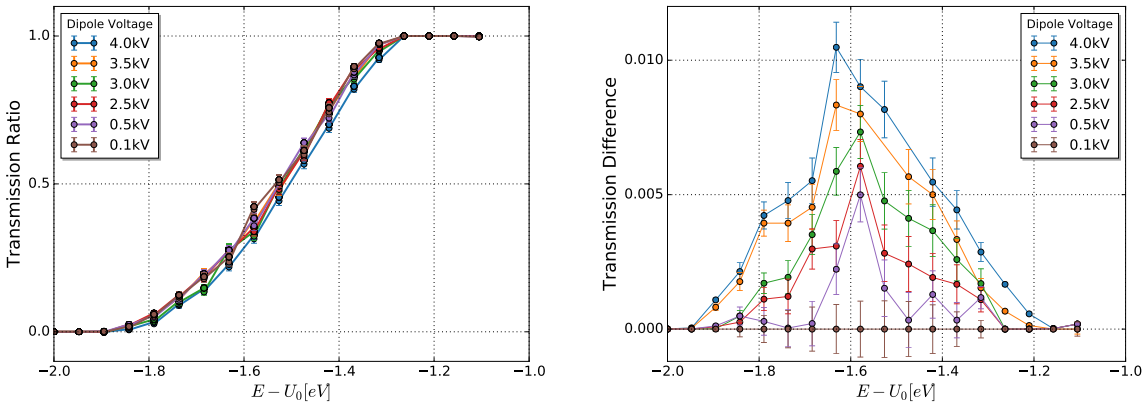

(A) (B)

Figure 5.18: (A)The dipole effect on simulated transmission functions without charge accumulation. Here each of the transmission functions is displayed colored by dipole voltage. For these simulations, the dipole voltage was adjusted without any charge accumulation. Clearly a broadening of the function can be seen. (B) The difference between each dipole voltage simulation and the 0.1kV measurement is shown. This elucidates the difference the dipole voltage has on the transmission function.

Immediately one can see that even without charge accumulation effects that there is some shape change in the transmission function. This will be investigated further in Section 5.5 via comparing both measured data and simulated data. However, the immediate conclusion is that the dipole has a broadening effect, however slight on the transmission function. The model attributes this to an actual broadening in the initial distribution. However, as it will be explained later, this can be due to additional transverse momentum imparted by the dipole electrode.

With Charge Accumulation

To further explain the charge accumulation runs, each point in a single transmission function is calculated using the data from the previous point. The first point in each direction is the non-accumulated run for each electromagnetic setting. Trapped charges are then introduced using the

data from the electromagnetic setting previous to the point being used. In other words, for an "up" run, the first point is the lowest in energy, and for a "down" run, the first point is the highest in energy. Reduced data is then re-introduced to the simulation as old particles in new electromagnetic settings. This process is iterated through the transmission function simulation such that a single particle with near-zero probability can survive the entire run set. The number of electrons detected is therefore the sum of normally transmitted electrons and those that transmit after trapping.

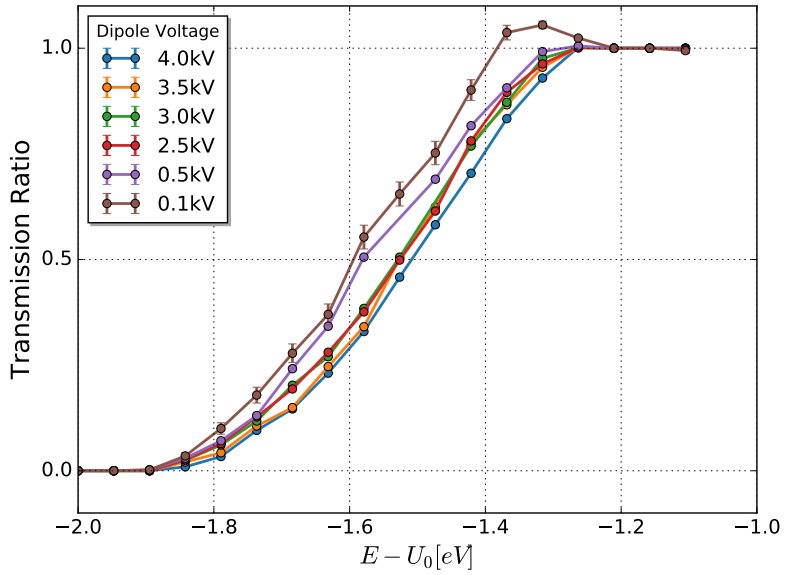

Figure 5.19: Dipole measurement transmission functions. Each data set is colored by dipole voltage used.

The feature in the simulated plots of the transmission function which is not reflected in the measured data is the bump in the 0.1 kV data set. Since the measured data does not have the 0.1 kV data set, this can't be directly compared, but the other data sets do have this feature. The simulations do not lose electrons between runs due to the measurement times, $t_1, t_2, ...$ in order to avoid circular dependence on τ. Therefore, the simulations will include more electrons at higher energies.

Figure 5.19 shows the results of the "up" runs, while the "down" runs are similar in shape to Figure 5.18. The ratio of electrons that survive long enough to be "shared" between bins follows an exponential trend, and is related to the survival time, as will be shown in Section 5.6.

Residual Computation

Residuals were computed in the same manner as the measured and analytic sections. Figure 5.20 shows the results. Error bars in this plot are generated through error propagation from the previous

plot. Here, as corresponding points are strongly correlated through the transmission function, the error must be reduced via,

$$2 * cov(up, down) = 2 * \sigma_{T,prev} \tag{5.4.5}$$

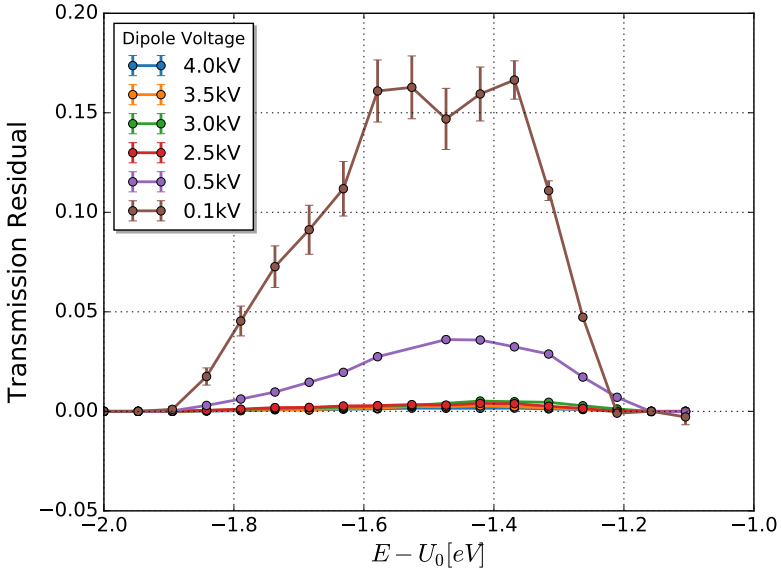

Figure 5.20: Simulated transmission function residuals. The color of the lines correspond to the dipole voltage used in each measurement. The lines themselves only serve to connect the data points for easier visualization.

Simulation Fits

Following the analytic and measurement sections, the simulated data were fit in an identical manner with the exception of rate. As the simulated transmission functions are constrained by the initial number of particles, the rate is a fixed quantity, 1.0. The results are shown in Figure 5.21.

Earlier it was assumed that the dependencies in the measured data were due to Penning discharge and background effects. The simulated data supports that assertion due to the fact that these effects are not in the simulation and the model fits the data better. The resulting fit parameters are shown in Table 5.4.

Once again the model fits better for higher dipole voltages. Other items of note are the change in mean distribution energy and spread. This will be addressed in the following section. In addition, similar to Section 5.3.5, the time constants will be discussed in the next section.

Additionally, as with the measurements section, the mean and variance change with dipole

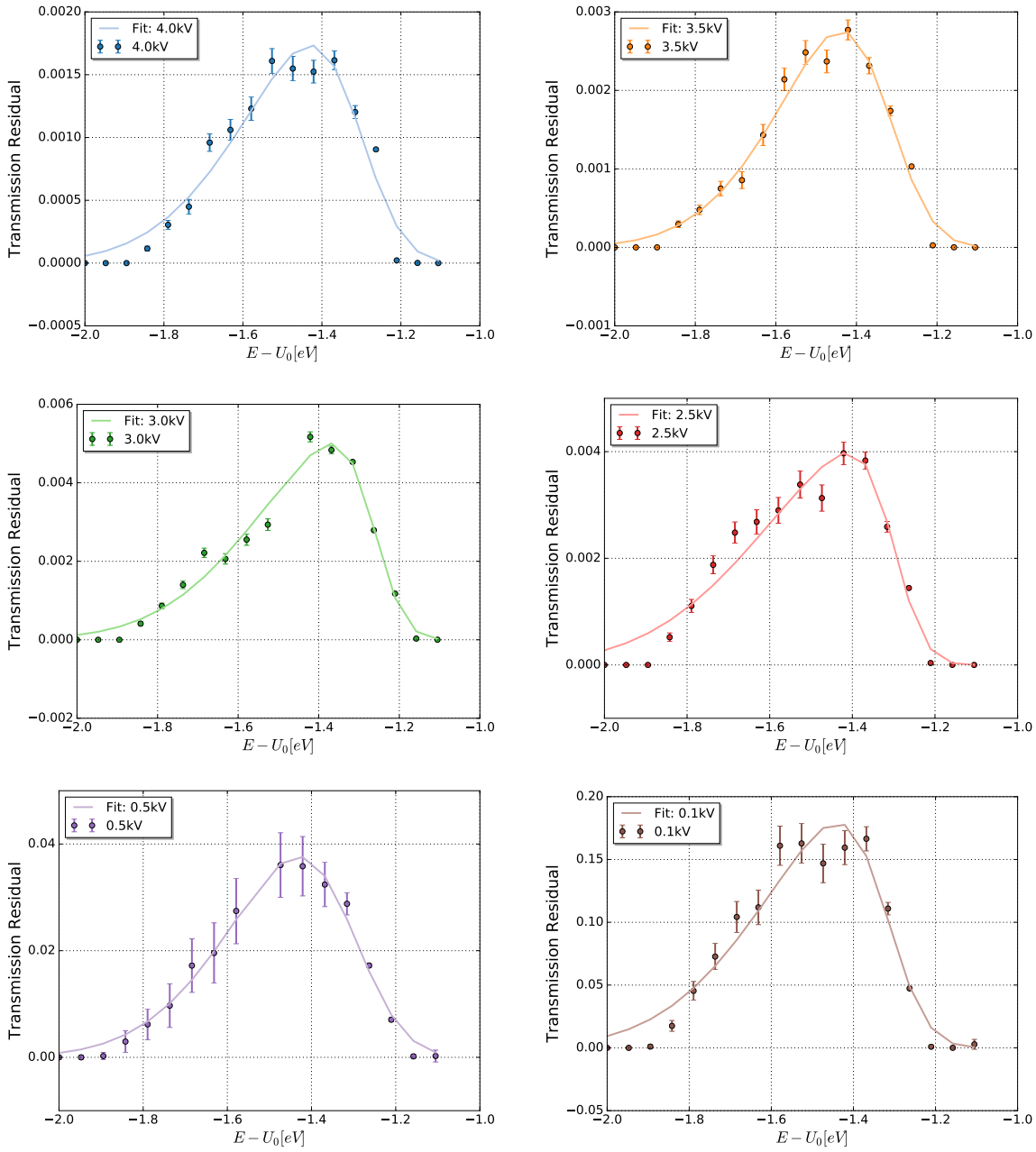

Figure 5.21: Individual Simulated Transmission Function Residuals. Each data set is colored by dipole voltage used in the simulation and represented by points. The fits are shaded in lighter colors and represented by lines. Note that each plot is scaled to the individual residual and therefore the y-axis scaling is different for each plot. Also of note in these plots are a few missing points. These points are missing due to crashes in the simulations software which made reproducing a single data set difficult.

$U_d[kV]$	χ^2	P-value	E_e	σ_e	$\overline{\tau}$
0.1	20.26	0.21	1.68±0.01	0.47±0.01	0.34 ± 0.19
0.5	18.04	0.31	1.55±0.01	0.48±0.01	$(6.79 \pm 0.40) \times 10^{-2}$
2.5	16.59	0.41	1.48±0.01	0.59±0.01	$(1.42 \pm 0.11) \times 10^{-2}$
3.0	15.72	0.47	1.49±0.01	0.61±0.01	$(1.29 \pm 0.12) \times 10^{-2}$
3.5	16.98	0.40	1.51±0.01	0.63±0.01	$(1.18 \pm 0.98) \times 10^{-2}$
4.0	13.13	0.62	1.47±0.01	0.67±0.01	$(3.01 \pm 0.05) \times 10^{-3}$

Table 5.4: Fit results for simulated charge accumulation data. For each dipole voltage, a fit was computed using the charge accumulation model. This shows the reduced chi-square value for the fit and the output fit parameters. The chi-squared values are shown for 16 degrees of freedom.

voltage. While it may seem that the fits are implying that the source mean energy and variance are changing with dipole voltage, that is only sufficient, but not necessary. The calculations used the magnetic field at it's maximal point and minimal point. Therefore, if the phase space changed between the source and the point in the beamline where the magnetic field is maximal, then this will be reflected in the fits. The following section will attempt to show that this is the case.

5.5 Comparison of Simulations and Analysis Results

During the previous sections, a few differences were noted between the simulations, the measurements and the analytic model. Namely, the mean electron energy and spread for the initial current distribution as calculated by the fits is different between simulations and measurements. Figure 5.22 shows the initial energy mean and spread obtained from the residuals fits as a function of dipole voltage. These values were fit to linear functions to show the change with dipole voltage. Since the dipole electrode introduces additional transverse energy into the electrons' cyclotron motion, the shift in energy can be explained by the adiabatic transformation of this additional energy into longitudinal energy at the analyzing plane. The accompanying change in the energy spread is due to the magnification of the transverse energy at the analyzing plane. This effect is not included in the model.

A prominent difference between the data sets is the skewness in the fit shape. Equation 5.2.14 shows that the limits of the integral are inclusive of the entire initial distribution function. Therefore, the skewness reflects the portion of the initial distribution function that is not integrated over. Physically, this represents the shift in energy introduced by the dipole electrode, but as yet does not show the source. The fit results are displayed in Table 5.5.

Differences between the simulations and measurements can arise from two known sources. The first is mis-estimation in the alignment parameters of the apparatus. While these parameters are

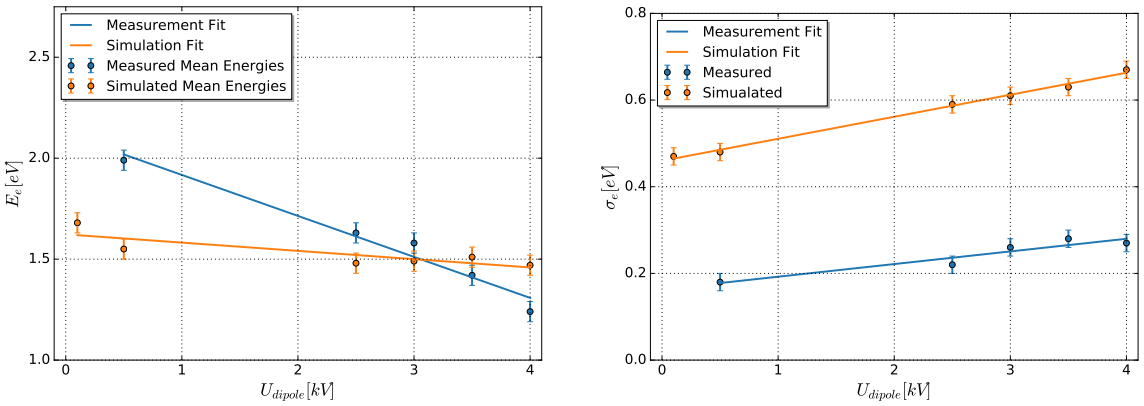

(A) (B)

Figure 5.22: (A) Mean energy of fits as a function of dipole voltage. (B) Energy spread as a function of dipole voltage. These values and errors were calculated from the fits in Tables 5.3 and 5.4.

Param	Measured E_e	Simulated E_e	Measured σ_e	Simulated σ_e
Offset	2.23 ± 0.11	1.62 ± 0.06	0.46 ± 0.01	0.16 ± 0.02
Slope	-0.26 ± 0.04	-0.25 ± 0.03	0.05 ± 0.01	0.03 ± 0.01
χ^2	0.41	0.21	0.31	0.11
P-Value	0.93	0.99	0.96	0.98
DoF	3	4	3	4

Table 5.5: Values from fitting the change in initial mean energy values and the spread in initial energy values. These are linear fits with 2 free parameters on 5 and 6 points.

known, it has been shown in previous theses that uncertainty in these parameters leads to miscalculations in transverse momentum [40]. The second difference is change in the work function at the surface of the EGun over the entire commissioning phase. At the beginning of the measurement phase, the work function quoted in the previous chapter was measured, but this may have changed over the course of the experiment. This work function was monitored over SDS Phase-I, and was found to change significantly over the measurement phase [55]. However, a Penning discharge at the conclusion of SDS Phase-II made monitoring the work function impossible. Therefore, uncertainty in the work function leads to a static offset in the mean and width whereas the alignment leads to a dipole voltage-dependent change in the statistics.

Since electron rate excess is not apparent in the down mode data from the measurements, this effect must be correlated to accumulated charge. This is reasonable since trapped electrons spend more time in the beamline and therefore experience a larger change in energy than transmitting electrons.

To further investigate why broadening occurs, the amount of time electrons spend in the main

spectrometer during simulations was calculated. Figure 5.23A shows the amount of time spent in the main spectrometer for untrapped or transmitting-only electrons. A total of roughly 28 points were obtained using a separate set of simulations. Points on this plot are calculated as the median arrival time for electrons that impact the detector. The error bar on either side of the point is the standard deviation for arrival time. A separate deviation is plotted for prior arrival and post arrival to elucidate the skew in arrival times. From this plot, one may deduce that with the initial phase space spread of electrons there is an increasing variance in the arrival time for particles at the detector. With increasing dipole voltage some transverse momentum is imparted to electrons which increases that spread. This concurs with the description of the momentum relation in Section 2.8.

In other words, the dipole electrode introduces some transverse momentum into the electrons. The shift in transverse momentum at the pre-spectrometer magnet translates to a shift in longitudinal energy at the analyzing plane. This shifts the mean of the fit. Since the transverse momentum introduced by the dipole electrode is dependent on the phase of the particle as it passes the magnet's focal plane, this introduces a shift in the variance. Therefore, the fits' shift in mean and variance in the initial phase space can be explained by transverse momentum imparted by the dipole electrode.

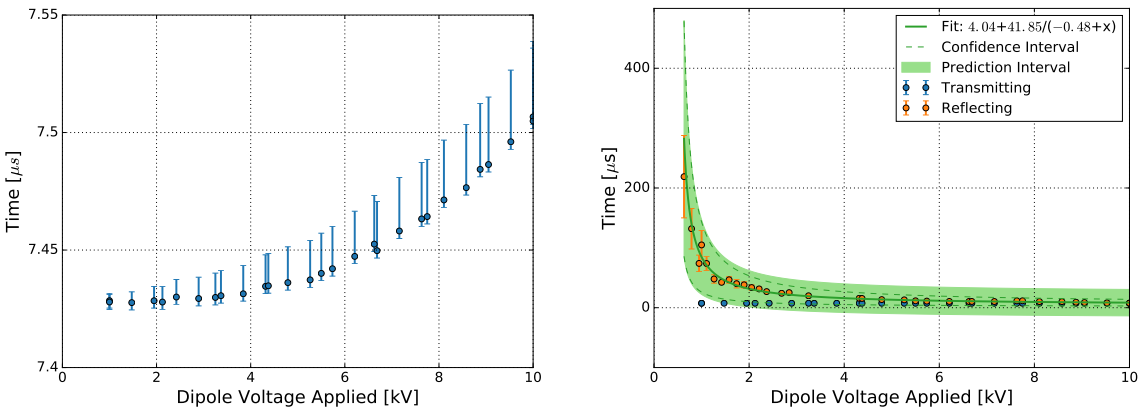

(A) (B)

Figure 5.23: (A) Simulated inter-arrival times for particles impacting the detector. Points are calculated as the median time difference between when the particle is created and when the particle impact the detector.(B) Simulated event lifetimes for reflecting and transmitting event. Transmitting events are defined by those impacting the detector. The fit was performed for $\bar{\tau}$ as a function of U_d. The fit line is for a $\chi^2/DoF = 31/27$. The prediction interval is for the 90% level using the T-distribution. The confidence interval was similarly calculated for the 90% level.

Since the model does not predict the change in initial mean energy and width, this will be treated as a separate effect from charge accumulation. To show that the dipole electrode model functions otherwise, further analysis is required.

5.6 Dipole Electrode Model Analysis

A valid model of the dipole electrode impact on charge accumulation means the dipole constant from Equation 2.8.38 predicts the trend of charge accumulation in the measurements. In the previous section, Figure 5.23 showed that the model accurately predicts the trend of the event lifetime within the spectrometer. For this figure, the time constant from the fit is computed to be $5.97 \pm 1.31\ \mu s$ with the fit prediction interval and confidence interval showing good agreement with the simulated data. Inputting values into the analytic model, the calculated value is $9.8\ \mu s$. This shows that the model isn't exact in the prediction of the trend. Discrepancies in the simulations come from geometric effects and thus this difference may be due to assumptions made regarding the uniformity of the fields.

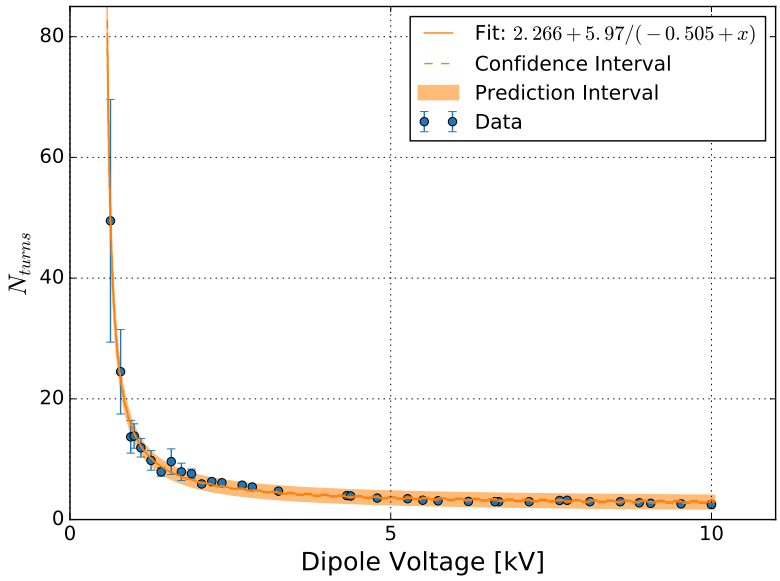

Figure 5.24: Number of times trapped particles reflect in the main spectrometer as a function of dipole voltage. Similar to Figure 5.23, this is a verification of the dipole electrode impact on the amount of time trapped particles spend in the beamline. The fit is to a simple $1/(a + x)$ model with $\chi^2/DoF = 24/27$. This shows that the dipole electrode description describes the number of times electrons reflect more accurately than the amount of time reflected. The prediction interval and confidence interval were calculated similar to Figure 5.23.

To better elucidate the dipole electrode's effect on trapped particles, the dipole electrode simulations can be used to simulate the number of reflections an electron undergoes before termination. Figure 5.24 shows the results as a function of dipole voltage. This simulation was run with energy excess, $E_e - U_0 = -1.2\,eV$. Figure 5.17 shows that this allows for higher sensitivity to the reduction parameter. As this was a value used in the previous simulations, this particular setting was chosen for convenience as any backplate voltage which produced a similar number of reflected electrons

would have sufficed.

What may be confusing about Figure 5.24 in the context of Figure 5.17 is that it shows a significant number of electrons trapped above the centroid region ($\geq -1.5\,eV$) for most of the dipole voltages. This seems to conflict with Figures 5.18 and 5.15 which show that the number of electrons detected decreases above this region. The reason for this being the case is that the number of electrons initially trapped decreases with increasing transmission. Thus Figure 5.17 shows only the simulated electrons entering the trap, and not those leaving the trap.

In these simulations several terminators were used. Namely, since the simulation takes up a large amount of memory tracks had to be killed for more than 100 reflections. The other terminator used was the surface interaction terminator. This terminator showed that the vast majority of electrons that impact a surface impact at the electron gun faceplate. This indicates that model assertion of directionality is correct.

Dipole Reduction Constant

Since the effect of the dipole on the lifetime of particles in the main spectrometer is now understood, the dipole constants from measurements, simulations and the analytic model can be compared against the analytic model. Figure 5.25 shows the fit values for the dipole reduction constant as a function of applied dipole voltage. These in turn are fit to the definition of $\overline{\tau}$ as a function of dipole voltage, U_d. In this plot, the green line shows the model prediction using the values defined for KATRIN.

Discrepancies between the model and data can arise from mis-evaluation of the electrostatic and magnetostatic fields. The model initially assumed that the field was uniform and equivalent to the field in the center of the beamline. For the measurements, this assumption is violated by mis-alignments in the system which cause the beamline to be misaligned with the center of the fields. In the simulations, the maximum deviation for a particle is on the order of 1 cm, which results in a magnetic field deviation of 4 μT and a dipole field deviation of 20 V. These deviations in the worst case scenario account for a factor of 8 difference in the dipole constant. Therefore, it is reasonable to assume that these misalignments are responsible for the discrepancy between model and data.

5.7 Null Hypothesis Testing

In an attempt to explore the possibility that the rate excess is caused by something other than the model in this thesis, an extensive correlation search was performed between the detector rate

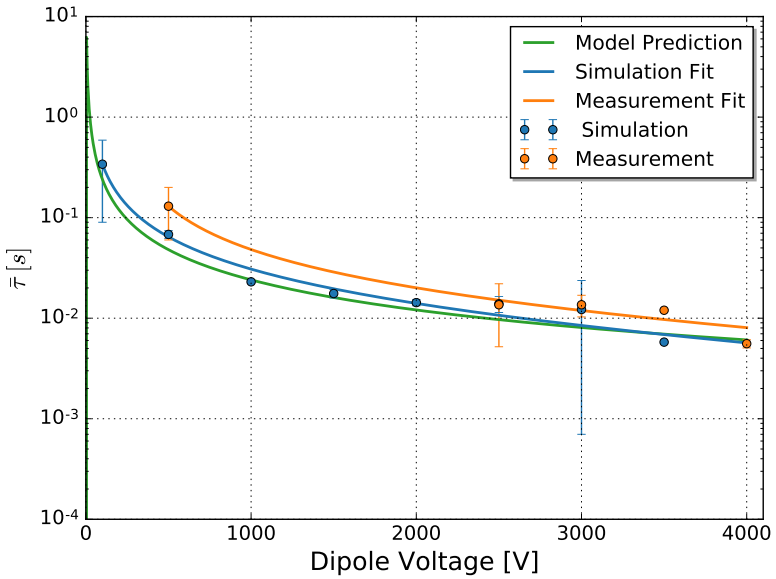

Figure 5.25: Dipole reduction constant for both simulations and measurements. This value is calculated from the fitting algorithm used in this study.

and each of the 270 slow controls channels in the KATRIN database. The results of this study are detailed in Appendix B. Nothing of particular significance was found, therefore reinforcing the assertion that electron rates on the detector must be from the intended source, the EGun.

5.8 Neutrino Mass Impact

This study shows that the model can describe the electron rate excess from trapped particles and the reduction on this rate due to the dipole electrode to some degree of accuracy. For the neutrino mass study, this model can be used to determine what the effect is on the measurement and the subsequent systematic errors from effects in this study. These effects are:

1. Energy distribution broadening from the dipole electrode.

2. Charge accumulation between measurements.

Energy distribution broadening comes from Section 5.6 where the EGun line width appeared to broaden in the fits of the simulations. In the measurements, the broadening was not as apparent, but was still observable in the fits and will therefore be included. Mis-estimating the resolution of the spectrometer causes electrons from lower energies to be counted with higher energy electrons.

The effect on the neutrino mass measurement can be estimated by using the energy spectrum from Equation 1.4.1. This spectrum will be used in Equation 5.2.12 as the current density function,

and the resulting spectrum will be the sum of Equations 1.4.1and 5.2.12. By neglecting other effect such as the final state uncertainties, the systematic error from charge accumulations can then be identified independently. For this simulation, the value of $\bar{\tau}$ will be taken from Figure 5.25 as function of dipole voltage. The voltage steps will be the width of the transmission function, $\sim 0.19\,eV$, and instead of manipulating the EGun backplate potential, the analyzing potential will be manipulated. The amount of time spent in each interval will be kept constant and this toy simulation will be re-worked for a couple of different measurement times.

This simulation will be run using a simple Monte Carlo. The goal of this study is to fit the resulting tritium spectrum to Equation 1.4.1 as function of dipole voltage and measurement time. The difference in fitted neutrino mass squared will be the estimated systematic error.

Using the approach outlined here assumes that the dipole electrode in the EGun and the dipole electrode between the spectrometers behave identically. As the physical design is similar, this is a reasonable assumption. Using the full simulation beamline, which does not exist at this point in time, this study will need to be repeated to account for the geometric differences between the EGun dipole electrode and "production" dipole electrode.

Figure 5.26 shows the results of this study for measurement times of 10, 20, and 30 minutes. Evidently, increasing the measurement time allows for the dipole electrode to empty the trap before subsequent measurements. The shape of the expected systematic error also follows the expected trend. In the low dipole regime of less than $\sim 1500\,V$, the shape is linear on the semi-log plot, which displays the dominant effect of charge accumulation. At higher dipole electrode voltages, the transmission width broadening becomes the dominant effect.

A conclusion that can be drawn directly from these plots is the suggested dipole voltage that should be applied. Each plot shows a minimum which corresponds to the point where charge accumulation and resolution broadening become competitive. For the 10 minute measurement this corresponds to $2566\,V$, $2358\,V$ for the 20 minute measurement, and 2034 for the 30 minute measurement. As the amount of time that will be spent at each point in the production measurement is as yet undecided, this procedure should be repeated to determine the dipole electrode voltage for the final tritium measurement.

Additionally, other strategies an be applied to mitigate the effect of charge accumulation. In the measurements, the broadening was only witnessed in the up mode data sets. Therefore, one can conclude that the tritium measurements be run in a single direction. However, this is undesirable as this limits the available configurations in which the system may be run.

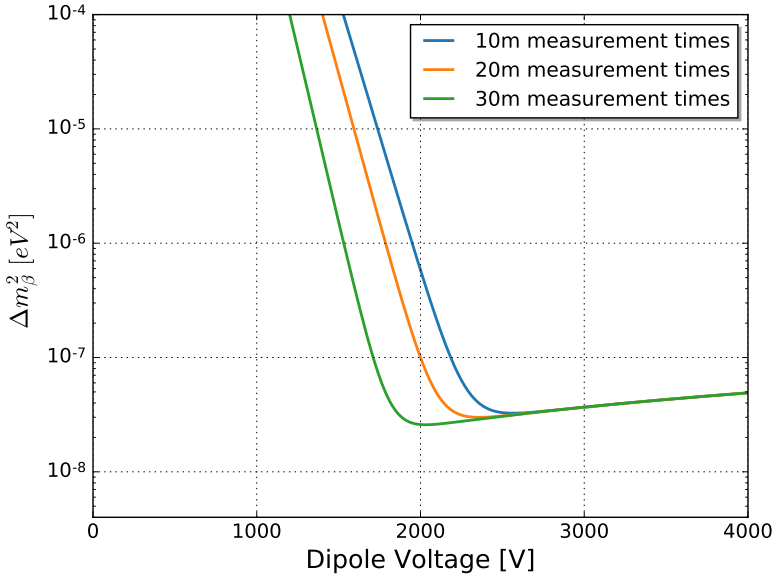

Figure 5.26: Impact on squared neutrino mass. The systematic error from each of the effects as evaluated as a function of dipole voltage and measurement time. These values were calculated using toy Monte Carlo with a simple tritium spectrum, the model of charge accumulation and dipole reduction. Each line represents roughly 100 calculations of the mass difference squared.

CHAPTER 6: CONCLUSION

6.1 Summary of Results

Prior to this investigation, the modifications of the transmission function due to charge accumulation and the dipole electrode were unquantified. This thesis provides a method for measuring these effects with an emphasis on the commissioning phase for the KATRIN spectrometer and detector sections. In addition, the systematic error associated with these effects on the neutrino mass measurement was quantified. This thesis shows that using a dipole electrode is necessary, but utilizing too high of a dipole potential can induce additional systematic errors in the neutrino mass measurement. Given that a dipole electrode will be used in the neutrino mass measurements, the dipole electrode model in this thesis provides a method for quantifying the systematic error associated with charge accumulation and the dipole electrode on the neutrino mass measurement.

6.1.1 Dipole Electrode Model

The model of beamline mechanics in KATRIN was improved by deriving a new dipole electrode model as shown in Section 2.8. From this model, modifications on electron position, momentum and energy can be derived. These were used in the charge accumulation model to quantitatively describe an effect on reflected electrons. As a similar electrode will be placed between the pre-spectrometer and main spectrometer, this model can be used to describe trapped particles between the spectrometers.

The effectiveness of the dipole electrode was validated against data measured during KATRIN main spectrometer commissioning. These measurements were checked against simulations and the dipole electrode was found to broaden the transmission function by roughly $30 - 50\,meV$.

6.1.2 Electron Gun Simulation

An electron gun simulation was developed for this study. This simulation was used to show the effect the dipole electrode has on transmitting and reflecting electrons. From this simulation, a broadening of the line width was observed on the order of 10%.

This simulation should provide further utility in KATRIN when the high intensity electron gun

is brought on-line in the rear section of the source. Much of the same code will need to be used and the methods used when deploying the simulation can also be recycled.

6.1.3 Charge Accumulation Model

A model describing how transmission functions in KATRIN are modified by charge accumulating in the Penning trap created by the main spectrometer was derived. This model functions under a number of reasonable assumptions, but is valid for dipole ranges of $500 - 3000\,V$ and electron rates below $15\,kcps$. This description uses the dipole electrode model to describe how a dipole potential can be used to reduce this effect. Measurements were made to validate this model and infer the parameters introduced in the model.

6.1.4 Neutrino Mass Impact

Using the results from the EGun simulations and charge sharing model, the impact on the neutrino mass from the dipole electrode and charge sharing was estimated. As these effects are competitive, a relative minimum was found for a variety of measurement times. For the measurement intervals, 10 minutes to 30 minutes, the minimum dipole voltages, of $2566 - 2034\,V$ produce errors of $\Delta m_\beta^2 = (6.51 - 5.16) \times 10^{-8}\,eV^2$. This provides an optimal operating voltage for the dipole electrode, as well as the quantitative assessment of the systematic error.

6.2 Moving Forward

As KATRIN expects to measure the neutrino mass to a sensitivity of 0.2 eV, systematic errors such as the one evaluated in this thesis must be accounted for. Table 6.1 shows the systematic errors produced by not accounting for various effects in the KATRIN experiment. This thesis shows that the dipole electrode potential must be optimized to produce a value as low as $O(10^{-8})\,eV^2$. Mis-underestimating this potential can lead to much higher systematic errors, and overestimation can also lead to an effect as high as $O(10^{-7})\,eV^2$. While, this effect is much smaller than the other effects, this will need to measured and optimized in the final neutrino mass measurement apparatus.

Given the method presented in this thesis, the rear section EGun will have to be used to replicate this study with the appropriate values for the source section. The simulation software developed in this thesis can be used to develop the simulation of the rear section EGun and source section. Then, the transmission function measurements can be repeated to quantify the source broadening effects and charge accumulation reduction measured in this thesis Finally, the systematic error induced by

Effect	Δm_β^2 $[eV^2]$
WGTS Axial Magnetic Field Inhomogeneity	$-(3.5\ -\ 0.1) \times 10^{-3}$
WGTS Field Offset	$(-33.0\ -\ 30.6) \times 10^{-3}$
Relativistic Corrections	-7.6×10^{-3}
Synchrotron Radiation	-24.1×10^{-3}
Angular Dependence on Scattering	11.9×10^{-3}
Angular Shift from Scattering	$O(10^{-4})$
Energy Loss from Scattering	2.1×10^{-3}
Dipole Electrode Modification and Charge Accumulation	6.58×10^{-8}

Table 6.1: Summary of KATRIN systematics. The entry for the dipole electrode and charge accumulation were produced by this thesis. All other values are summarized from Stefan Groh's thesis [40]. For the value produced by this thesis, it was assumed that optimal measurement time and dipole electrode potential would be chosen. For the value of systematic error due to unaccounted for angular shift from scattering, the value quoted is of order 10^{-4} eV and thus is not fully quantified in the source material for this summary.

charge accumulation and the final dipole electrode can quantified following the method of this thesis.

6.3 Outlook

Starting in 2017, the KATRIN experiment will begin data taking for measuring the neutrino mass. KATRIN is currently investigating measurement strategies and analyzing potential distributions for achieving the design sensitivity. Several other future measurements will come online to perform similar measurements. Between these measurements, the next generation of neutrino mass experiments will provide a result or limit that will shed insight into future neutrino physics. Complimentary physics from neutrinoless double beta decay experiment, atmospheric neutrino oscillation experiments and cosmology will answer the open questions in neutrino physics.

APPENDIX A: THOROUGH DERIVATION OF MAC-E FILTERING

A challenge faced by designers of electronic spectrometers is the ability to precisely filter electrons below a specified level without reducing luminosity. A possible solution is magnetic adiabatic collimation and electrostatic (MAC-E) filtering, which uses magnetic guiding fields to collimate electrons into an axially symmetric beamline before filtering with an electrostatic potential. This section will prove that this technique is possible under a few restrictions following the derivation of Beamson, Porter and Turner[37].

Since electrons near the tritium endpoint have a Lorentz factor of

$$\gamma = \frac{1}{1 - v^2/c^2} \approx 1.04$$

A non-relativistic calculation will be used.

A high magnetic field is used at the electron source to induce cyclotron motion. This motion is described by the procession frequency as a function of electric charge, e, electron mass, m_e and the magnetic field along the axis of symmetry, $B_\parallel$. The procession frequency can also be written in terms of the initial momentum perpendicular to the axis of symmetry, $p_\perp$, and the radius of the cyclotron motion, r_c

$$\omega_c = \frac{e}{m_e} B_\parallel = \frac{p_\perp}{m_e r_c}$$

In the frame of the electron axial motion, cyclotron motion generates a magnetic moment, μ.[1] This can be written in terms of the kinetic energy perpendicular to the axis of symmetry, $T_\perp$.

$$\mu = \frac{-p_\perp}{2m_e B_\parallel} = \frac{-e}{2m_e} p_\perp r_c = \frac{T}{B_\parallel}$$

As magnetic fields are conservative, the total kinetic energy, E is conserved,

[1] For a relativisitic calculation, $\gamma\mu$ should be used.

$$\frac{dE}{dt} = -\frac{d(E_\perp + T_\parallel)}{dt} = 0 \tag{A.0.1}$$

$$\implies \frac{dE_\parallel}{dt} = -\frac{dE_\perp}{dt} = \frac{d\mu B_\parallel}{dt} \tag{A.0.2}$$

The important restriction here is that if the magnetic flux lines converge or diverge smoothly, then $dB_\perp/dz \approx d\vec{B}/dz$ is roughly constant. This is equivalent to saying that the surface transcribed by both cyclotron and axial motion will contain the magnetic flux lines if and only if the flux lines converge or diverge smoothly. Newton's law can then be applied to the Lorentz force law, where B_r is the magnetic field in the radial direction

$$\frac{dp_\perp}{dt} = \frac{e}{m} p_\perp B_r$$

where,

$$B_r = -\frac{1}{2} r_c \frac{\partial B_\parallel}{\partial z}$$

Multiplying both sides by $p_\perp = mdz/dt$ yields:

$$\frac{dp_\parallel}{dt} p_\parallel = (-\frac{1}{2} e r_c p_\perp) \frac{\partial B_\parallel}{dz} \frac{dz}{dt}$$

$$\implies \frac{d}{dt} \frac{p_\parallel^2}{2m_e} = [-(e/m_e)\frac{1}{2} p_\perp r_c] \frac{dB_\parallel}{dt}$$

This can be written in terms of the kinetic energy,

$$\frac{d}{dt} E_\parallel = \frac{d}{dt} \mu B_\parallel \tag{A.0.3}$$

Combining (A.0.2) and (A.0.3) yields:

$$\mu \frac{dB_\parallel}{dt} = \frac{d(\mu B_\parallel)}{dt}$$

Therefore, the magnetic moment is invariant over consecutive cyclotron motions around smoothly diverging/converging field lines. The consequence of this invariance is that the quantity $p_\perp^2/B$ is also invariant. For two different cyclotron motions, labeled (a) and (b), the following holds true:

$$p_\perp^2(a)/B(a) = p_\perp^2(b)/B(b)$$
$$|p|^2 = p_\parallel^2(a) + p_\perp^2(a) = p_\parallel^2(b) + p_\perp^2(b)$$

Where the second equation is just decomposition of momentum into perpendicular and parallel components. Combining these yields:

$$p_\parallel^2(b) = |p|^2 - p_\perp^2 = (|p|^2 - p_\perp^2)\frac{|B(b)^2|}{|B(a)^2|}$$

In other words, between two different cyclotron motions, an increase in magnetic field causes the perpendicular momentum to be adiabatically transferred to parallel momentum.

The flux enclosed by this helical orbit, Φ is,

$$\Phi = \pi r_c^2 |B|$$

In terms of the magnetic moment,

$$\Phi = (-2\pi m/e^2)\mu \tag{A.0.4}$$

Since μ is invariant, Φ is also invariant. This verifies electrons move along the surface of a constant flux tube. In addition, flux can never be brought to a true value of 0, and therefore the perpendicular momentum can only be reduced, and not eliminated.

MAC-E filtering is traditionally parameterized in terms of the magnetic field maximum at the source, B_S, the minimum field which it is brought to, B_{min}, and an electrostatic potential maximum U_0. The electrostatic potential, known as the analyzing potential is at a maximum where $B = B_{min}$, a plane known as the *analyzing plane*. At the analyzing plane, electrons with energy $E < qU_0$ will be reflected. Some of the electrons with energy over qU_0 will be transmitted across the spectrometer, where the magnetic field will adiabatically guide the electrons to a detector. The conditions in which electrons are transmitted will be derived following Picard's calculation[38].

Suppose an electron is emitted with pitch angle, θ_{pch}, the angle between the initial momentum and the axis of symmetry. The momentum can be rewritten,

$$p_{\perp} = |p| sin(\theta_{pch})$$
$$p_{\parallel} = |p| cos(\theta_{pch})$$

After the electron traverses to the analyzing plane, the perpendicular momentum will be reduced as,

$$\frac{p_{\perp}(start)^2}{B_s} = \frac{p_{\perp}(analyzing)^2}{B_{min}}$$
$$p_{\perp}(analyzing)^2 = p_{\perp}(start)^2 \frac{B_s}{B_{min}}$$

The second restriction for Mac-E filtering is the electrostatic potential needs to increase slowly in order for the adiabatic condition to be met. At the analyzing plane, the electrostatic plane will filter based on the following condition,

$$p_{\parallel}^2/2m_e \leq qU_0$$

Which in terms of the pitch angle can be rewritten as a definition of the maximum angle θ_{max} that can transmit at a given start energy, E.

$$\theta_{pitch} \leq \theta_{max} := arcsin\left(1 - \sqrt{\frac{(E - qU_0)}{E}\frac{B_{min}}{B_{max}}}\right)$$

Since the source is confined to the axial symmetry, a beam tube with solid angle 2π can be defined. The ratio of θ_{pch} to the solid angle can be written where the limiting cases of $\theta_{pch} > 2\pi$ and $\theta_{pch} \leq 0$ are used to piecewise define a function known as the *transmission function*, $T(E)$.

$$T(E) = \begin{cases} 0 & \rightarrow\ E \leq qU_0 \\ 1 - \sqrt{1 - \frac{E-qU}{E}\frac{B_{min}}{B_S}} & \rightarrow\ qU_0 \leq E \leq qU_0\frac{B_{min}}{B_S} \\ 1 & \rightarrow\ qU_0\frac{B_{min}}{B_S} \leq E \end{cases} \tag{A.0.5}$$

A way of interpreting this is as the transmission probability for an electron produced by an isotopic source with some momentum in the direction of the spectrometer. Since all transmitted electrons are treated equally at the detector, the limiting case for a maximum transmitting pitch angle can be used to bound the resolution of the spectrometer.

$$\frac{\Delta E}{B_S} = \frac{E}{B_{min}}$$
$$\Delta E = E\frac{B_{min}}{B_S}$$

For KATRIN, this implies that at the tritium endpoint energy, $18.6keV$, and with fields, $B_s \approx 6T$ and $B_{min} \approx 3.8G$, the resolution of the spectrometer is roughly $0.93eV$

This also defines a critical angle at which electrons will be reflected at:

$$\theta_{mirror} = arcsin\sqrt{\frac{B_{source}}{B_{max}}} \approx 50.77^\circ \tag{A.0.6}$$

APPENDIX B: CORRELATION CHECKING THE DATA AGAINST SLOW CONTROLS VALUES

B.1 Correlation Searches

While the model is sufficient to describe rate excess, it has not been proven to be necessary. To check for other rate sources, a correlation search can be run between the detector rate and the slow controls channels.

KATRIN stores data in 237 channels in a slow controls database known as the Advanced Data Extraction Infrastructure (ADEI)[82]. These can be queried for values within a timeframe. Therefore, for each of the channels and runs in the measurement phase, a correlation search can be run.

B.1.1 Binning

The slow controls database reports values at either the reporting rate for the sensor or the polling rate for the database. The sensor reporting rate is determined by the sensor and can vary widely. For values polled by the database, the polling rate is usually roughly $1 - 10$Hz. In either case, these values are polled much slower than the detector rate.

To makeup for the difference in rate a uniform time binning strategy was used to bin both the detector rate and slow controls value. From these bins, the sample mean and variance are calculated. These values will be used in the correlation search.

B.1.2 Correlation Strategies

Correlation can be established numerically via several strategies that will be outlined in this section. Each has strengths and weaknesses that can be used to validate the data. As the data comes from heterogeneous sources, a combination of these strategies can be used to determine meaningful correlation between samples.

Kendell's Tau

The analysis structure thus far has been built on Python's Numpy[83] and SciPy[84] modules. Naturally, the built-in module for point correlation was used[85]. Kendell's tau measures the number of corresponding ordinal rankings between 2 data sets.

The strength in this algorithm is the easy association of rankings for values in transmission functions. For each "up" data set, the ordinal ranking are always increasing and vice-versa for

"down" data sets. For the slow controls values, Kendell's tau becomes a measure of how frequently slow controls sensor values increase with the runs and vice versa.

By contrast, this algorithm presents a very binary description of correlation. As there is expected to be a strong correlation in the control variables for the EGun, weak correlations whose ordinals match up the same would be treated identically. This suffers a reduction for continuous variables, but for bivariate variables such as switches turning on and off, this can help eliminate false positives.

Pearson's First Correlation Coefficient

One of the most commonly used methods in correlation detection is Pearon's First Correlation Coefficient[86]. For two sample sets, X and Y, this is defined below as as ρ, where cov is the covariance of the data sets, σ the single variable variance and E the expectation value.

$$\rho_{X,Y} = \frac{cov(X,Y)}{\sigma_X \sigma_Y} = \frac{E[(X - E[X])(Y - E[Y])]}{\sigma_X \sigma_Y} \tag{B.1.1}$$

Generally, Pearson's correlation coefficient is used for large or continuous data sets. As the EGun data consists of 20 points per run, the statistics are low and therefore this test is only valid if the data sets follow normal statistics individually and the covariance is also normally distributed. Hence, a second strategy is to determine either dependence or distribution.

Sample Correlation Coefficient

Sample correlation coefficients are used in sparse data sets when the individual data sets are not assumed to follow independent normal distributions. The equation below defines this strategy as the identical numerator, but with a non-coherent sum in the denominator.

$$\rho_{sample} = \frac{\sum_{i=1}^{n}(x_i - \bar{x})(y_i - \bar{y})}{\sqrt{\sum_{i=0}^{n}(x_i - \bar{x})^2 (y_i - \bar{y})^2}} \tag{B.1.2}$$

Generally speaking, if the sample correlation coefficient coincides with Pearson's, then the two variables are normally distributed independent data sets. By negation, non-coincidence implies either a common source or poorly estimated normal distributions.

B.1.3 Correlation Testing

In addition to coefficient calculation, a test can be built on top of the coefficients to indicate the meaningfulness of the calculation. If the two sample distributions show a true correlation, the the significance, defined below as t will be much smaller than the coefficient itself[86].

$$t = \frac{r}{\sqrt{\frac{1-\rho^2}{N-2}}} \tag{B.1.3}$$

B.1.4 Testing Algorithm

Using these tools, a strategy was developed for finding meaningful correlations. The following list details the algorithm:

- For each set of data all of the coefficients and corresponding test values were computed
- Data sets were "thrown out" for poor t values on all of the coefficients
- If a data set is sparse, the algorithm defaults to the sample coefficient
- If a data set is bivariate, the algorithm defaults to using Kendell's Tau
- Otherwise, Pearson's coefficient is used
- Values outside of $[-1.0, 1.0]$ are thrown out

Below, Table B.1.4 shows the surviving values and the corresponding coefficients. The KATRIN Number is an internal serial number and the column denoted "Description" is a database name for the channel. These are separated by run to show which run has the highest correlation. Repeat values were omitted from the table due to redundancy.

Immediately, one can see that the strongest correlations are from the channels associated with the EGun. Some additional rate seems to come from the temperature and pressure in the experiment, though this is to be expected. While this approach works well for single runs, what is needed is an explanation for hysteresis.

B.1.5 Correlation Difference

To see if there is any dependence on either "up" or "down" directions, multiple data sets can be used to calculate a correlation coefficient difference. For the case of Pearson's coefficient, this is calculated below.

$$r_{diff} = r_{up} - r_{down} \tag{B.1.4}$$

$$r_{diff} = \frac{cov(X_{up}, Y_{up})}{\sigma_{X,up}\sigma_{Y,up}} - \frac{cov(X_{down}, Y_{down})}{\sigma_{X,down}\sigma_{Y,down}} \tag{B.1.5}$$

Run Number	KATRIN Number	Description	Sample Correlation
23408	452-REU-3-0004-0001	e-gun	1.0
23408	452-REU-3-0004-0111	range	1.0
23415	452-EHV-3-0003-0001	rear electrode	-1.0
23415	452-EHV-3-0003-0101	voltage rear electrode	-1.0
23415	452-EHV-3-0003-0103	difference voltage	-1.0
23403	523-PCR-6-1100-0001	HVac cryopump temperature	-0.93
23393	522-PCR-3-1100-0001	XHV cryopump temperature	0.89
23398	535-RTY-0-1010-0001	Temperature on detector platform	-0.86
24104	535-RMY-0-1015-0001	Relative humidity on detector platform	0.82
24110	411-REI-1-2110-0001	PS2 Current	0.65
24110	411-REI-1-2110-0030	PS2 Status	0.65
23403	521-HEE-0-2245-0001	Detector-magnet heater power	0.64
23393	535-HEE-0-1101-0001	Temperature reading for PID loop 1	-0.63
23403	521-RPY-0-1240-0001	Pinch magnet absolute pressure	-0.61
23408	535-HEE-0-1104-0001	Temperature reading for PID loop 4	0.61
23414	527-ELV-0-1601-0101	12-V-supply (FET) current readback	-0.60
23414	535-RTY-0-1010-0001	Temperature on detector platform	-0.60

Table B.1: Linear Correlation with slow controls parameters

Dipole [kV]	KATRIN Number	Description	Difference
2.5	523-PCR-6-1100-0001	HVac cryopump temperature	-1.62e-9
4.0	452-EHV-3-0003-0001	rear electrode	-7.90e-06
3.5	452-EHV-3-0003-0001	rear electrode	4.93e-06
2.5	452-REU-3-0004-0001	e-gun	0.0
2.5	452-REU-3-0004-0111	range	0.0

Table B.2: Correlation differences between up runs and down runs.

Which assuming linear independence of the individual variances, such that $\sigma_{X,up} = \sigma_{X,down} = \sigma_X$, is calculated as,

$$r_{diff} = \frac{cov(X,Y)_{up} - cov(X,Y)_{down}}{\sigma_X \sigma_Y} \tag{B.1.6}$$

The result of this study is shown in Table B.1.5 as a function of dipole voltage Here, the dependence on the EGun difference voltage shows some additional error in the study for high dipole voltage. This might explain the model descrepency.

For comparison, some background runs were analyzed for the same correlation coefficients. Table B.1.5 shows the results of this study. Here, each of the correlations coefficients is shown to illustrate the difference in values for the sensor sources.

KATRIN Number	Description	Kendell	Pearson's	Sample
522-RPP-3-1250-0001	XHV chamber pressure (CC)	2.31e-05	1.04e-05	0.47
535-RPY-0-1005-0001	Atmospheric pressure on detector platform	7.06e5	8.74e-06	0.39
535-RTY-0-1010-0001	Temperature on detector platform	8.23e5	7.94e-06	0.36
535-RMY-0-1015-0001	Relative humidity on detector platform	2.367e5	6.39e-06	0.29
535-HEE-0-1101-0001	Temperature reading for PID loop 1	7.79e-5	5.71e-06	0.26
522-VAO-3-1010-0300	Beamline gate valve is closed	6.86e-3	4.92e-06	0.22
535-HEE-0-1102-0001	Temperature reading for PID loop 2	6.09e-5	4.92e-06	0.22
522-PCR-3-1100-0001	XHV cryopump temperature	5.56e-5	4.12e-06	0.19
525-EHV-0-1050-0211	PAE voltage-ramp step size	4.46e-3	3.01e-06	0.14
527-ELV-0-1601-0002	8-V-supply voltage readback	3.89e-5	1.75e-06	0.079
527-ELV-0-1604-0001	120-V-supply (bias) voltage readback	5.81e-5	8.98e-07	0.04
527-ELV-0-1603-0001	+6-V-supply (preamp) voltage readback	2.91e-5	5.32e-07	0.02
527-ELV-0-1603-0002	-6-V-supply (preamp) voltage readback	2.91e-4	4.38e-07	0.02
523-PCR-6-1100-0001	HVac cryopump temperature	1.41e-7	2.84e-07	0.012
527-ELV-0-1604-0101	120-V-supply (bias) current readback	0.26	2.41e-07	0.01

Table B.3: Correlation coefficients for background runs.

The only values that show a linear correlation with the e-gun voltage applied are the cryopump temperatures. This would seem to indicate that at least some of the rate at the detector is coming from the cryopumps. Given that the baffles were cooled during the measurement phase, this is unlikely. The readback values also show small differences. This was taken into account in the calculation of the error bars in the voltage values in the original study. I'm hoping that this means we have a measurement of the hysteresis in the E-Gun power supplies, and that it's minimal in it's effect on transmission.

APPENDIX C: THE FPD COSMIC RAY VETO

The veto system was designed at the Massachusetts Institute for Technology (MIT). It consists of a passive 3cm lead and copper shield, and an active layer of Bicron-408 plastic scintillator panels. Copper was chosen to line the interior of the lead shield due to the relative radio-purity and therefore the ability to absorb lead X-rays, reducing the intrinsic background in the shield. The scintillator panels are formed into a cylinder around the FPD in order to cover the maximum geometric acceptance angle to the detector. Figure C.1 shows how the panels are split into 4 long panels which form the barrel, and 2 panels which form the end cap.

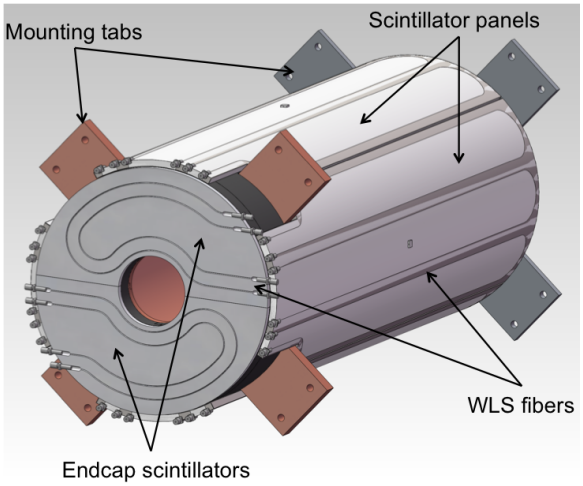

Figure C.1: Schematic Drawing of the KATRIN veto

Each of the long panels is read out by six St. Gobain wavelength shifting (WLS) fibers while the end caps are read out by four fibers. The scintillator panels output light at 425 nm, and the WLS fibers shift the light up to 493 nm into the sensitive region which was chosen based off the detector design [87]. Fibers were designed to be read out in tandem by looping single fibers to dual outputs. This allows for coincidence between fiber pairs to be used to detect potential events in the panels.

Figure C.2: The St. Gobain fibers used to read out the scintillator panels.

In order to function in the high electromagnetic fields, the detectors chosen to read out the wavelength shifting fibers were Hamamatsu Multi-Pixel Photon Counters (MPPCs).[88]. These are solid state detectors that function in high magnetic fields and have a high quantum efficiency. MPPCs consist of a pixelated array of avalanche photo diodes operated in the gieger regime with a common quenching mechanism. Coincidental photons incident on the face of the detector cause the output voltage to increase multiplicatively. The result is highly discretized voltage outputs representing the number of simultaneously firing pixels. For historical reasons, these are called photoelectron (P.E.) peaks, as pictured in Figure C.3. With 4 long panels of 6 fibers and 2 end caps of 4 fibers, this makes for an array of 32 detectors.

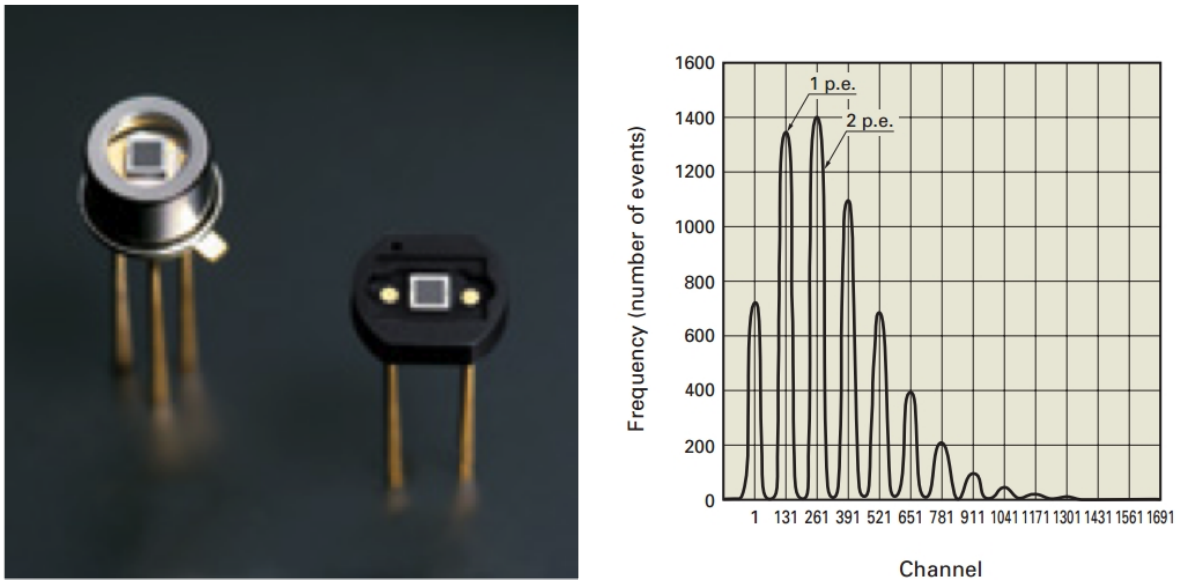

(A) (B)

Figure C.3: (A) A sample photo of MPPC devices .[88]. (B) A histogram of digitized MPPC voltage pulse heights .[88].

Electronics were designed at the Karlsruhe Institute of Technology (KIT) for biasing and amplification of the MPPCs [89]. Optimal bias for the MPPCs is chosen to maximize the signal separation of the P.E. peaks without causing surface currents due to over biasing.

A "veto event" is defined as at least n_f coincident channels and the analogue sum channel triggering in the time window, t_f. The values of n_f and t_f are user controlled variables. Each event, when digitized contains information on panel number, number of fibers triggering, timing and pulse height for each fiber channel and the sum channel.

Construction of the KATRIN FPD Veto

Construction of the KATRIN FPD Veto occurred in several stages. The system was initially constructed at MIT and delivered to UW. However, the system was electronically unstable and difficult to operate, so the system was upgraded and delivered to UNC. After characterization at UNC, the system was delivered to KIT where several additional issues were found during testing and commissioning. These problems were addressed and solved, as will be enumerated below.

The long panels were constructed out of flat scintillator with grooves cut for the fiber inlays. Heat molding onto PVC formed the shape of the panels. Gore ePTFE and Tyvek were then wrapped around the panels in order to increase photon collection efficiency.

(A) (B)

Figure C.4: (A) The long panels layer out side by side. (B) The end caps layer on top of test scintillator panels.

Fibers were glued and inserted into the panels. To transport light to the MPPCs, external fibers are connected, as shown in Figure C.5. The other end of the external fiber is then connected to the MPPCs.

Implementation of the MPPCs

At room temperature, the MPPCs were found to have an intrinsic dark rate on the order of MHz. The FPGAs in the Mark IV electronics are only designed to handle triggered events at a maximum rate of ∼100kHz. Therefore, cooling is necessary in order to reduce the dark rates. At -18°C, the rate is reduced down to ∼10kHz, and therefore the FPGAs can manage these rates. However, at this temperature, the MPPCs need to be contained in a low-humidity environment in order to reduce leakage currents that can arise because of condensation on the detectors. Therefore, the MPPCs were contained in a nearly hermetically sealed box, with an externally supplied flow of dry nitrogen.

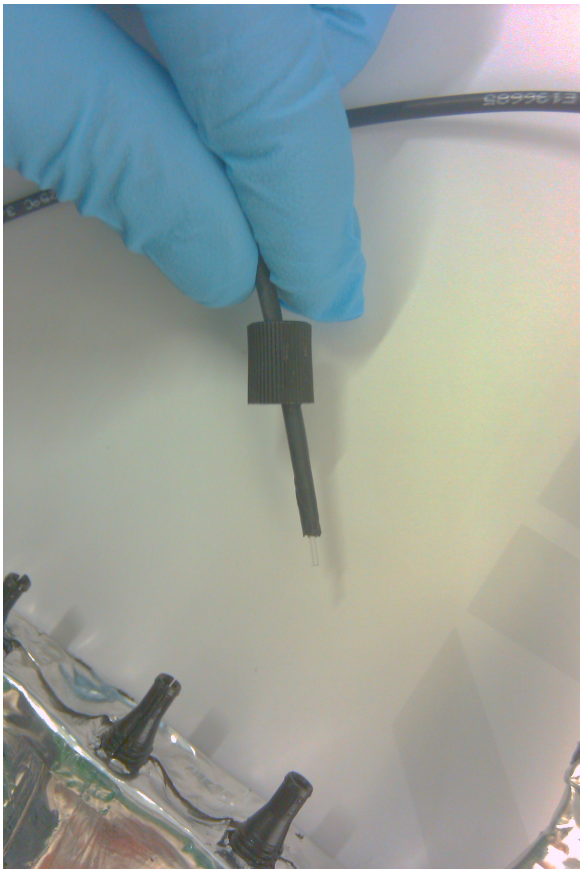

Figure C.5: A close up of the fiber connections to the external fibers.

Construction of the Electronics Enclosure

The improvements described in the previous section proved to be unstable however, as the cooling of the dry-nitrogen atmosphere causes air currents to form in the enclosures. In addition, the biasing electronics could not be adjusted as they were contained in the MPPC environment. The new design improvements also had a grounding scheme that induced noise in the outputs of the MPPCs. The digitization electronics could not filter the noise, and therefore the system needed redesign again.

Revisions Made at UNC

The redesigned system now contains two enclosures. One enclosure houses the MPPC units. The MPPCs are mounted on a large aluminum bar that is also connected to two Peltier cooling devices. Water cooling is provided to the Peltier devices in order to increase cooling efficiency. This chamber is filled with dry nitrogen, and therefore is not meant to be opened after the system is setup. The second enclosure houses the electronics, which is allowed to be opened in order to adjust

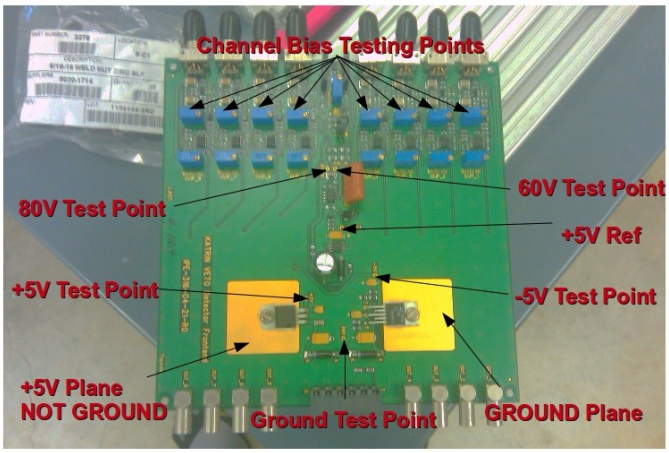

Figure C.6: The IPE biasing and amplification electronics. Note that the bias is adjusted on the boards.

the biases.

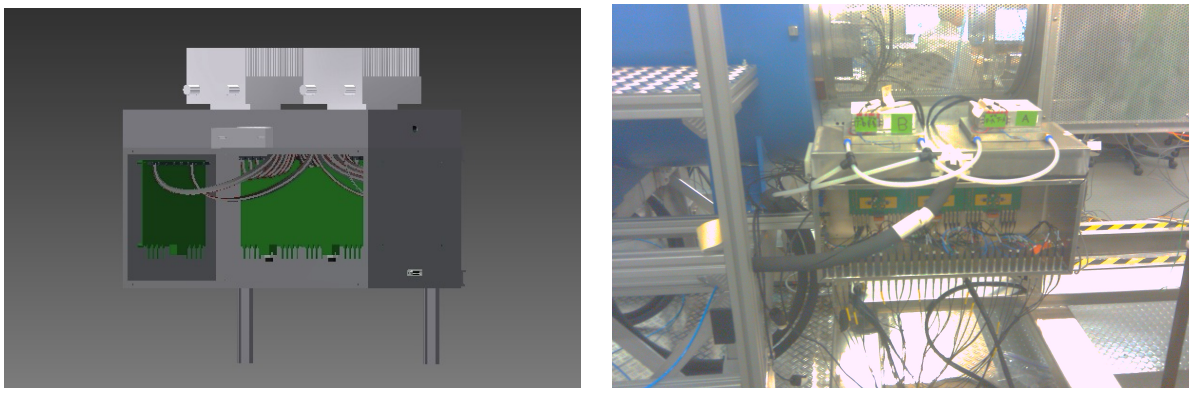

(A) (B)

Figure C.7: (A) CAD drawing of new veto enclosure. (B) Fully implemented veto enclosure.

Revisions Made at KIT

The system was delivered to KIT to implemented with the rest of the experiment, as pictured in Figure C.7 and Figure C.8. During evaluation at KIT, however, it was confirmed that the data acquisition electronics were not optimal for characterization of the system [1].

With the stable system at KIT, the Mark IV electronics were again analyzed for performance with the veto system. The Mark IV crate is clocked at 20 Mhz, or in 50ns intervals between ADC latches. Signals from the veto are characterized as a voltage pulse with a characteristic width of 50 ns. The Nyquist theorem therefore states that in order to accurately calculate the voltage of the

[1] Due to earlier measurements at UW and UNC, it was found, but not fully elucidated that the default FPGA code was not optimized for the veto

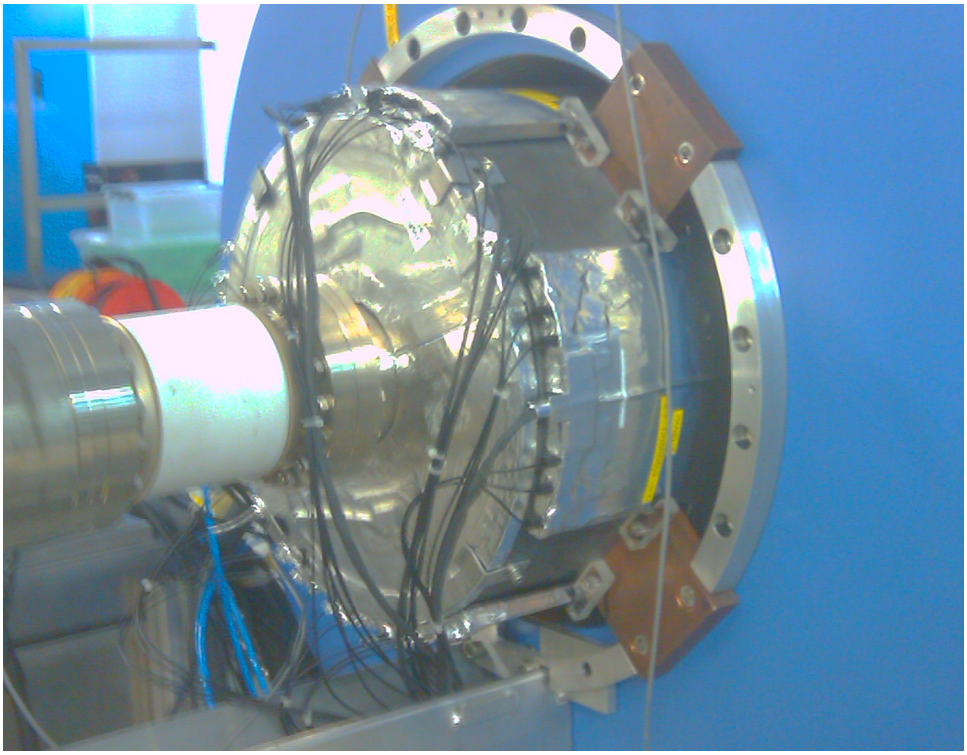

Figure C.8: The veto panels in position at KIT.

pulse, a minimum of 2 ADC values must be used in the calculation.

The original input filter for the Mark IV crate used the difference between two points on an ADC trace to calculate the energy, which is below the Nyquist limit. Therefore, the Mark IV crate FPGA routines were upgraded to integrate over multiple points in the trace and therefore collects sufficient information. P.E. peak resolution was improved from the original value of 0.7 in the region of interest to 3.2, as calculated by peak height divided by full-width at half maximum.

With these improvements made, the veto hardware required further characterization before it would be considered commissioned and ready for use with the focal plane detector system.

Evaluation of the KATRIN Veto

In order to use the veto, one must show that it can be reliably operated over long periods of time meaning that the system is stable and the rates agree with Poisson statistics. Additionally, the veto's efficiency must meet the performance goals.

Stability

To demonstrate stability, both triggering rate stability and spectral stability were used. The reason for using rate stability is that this demonstrates temperature stability in the MPPC enclosure

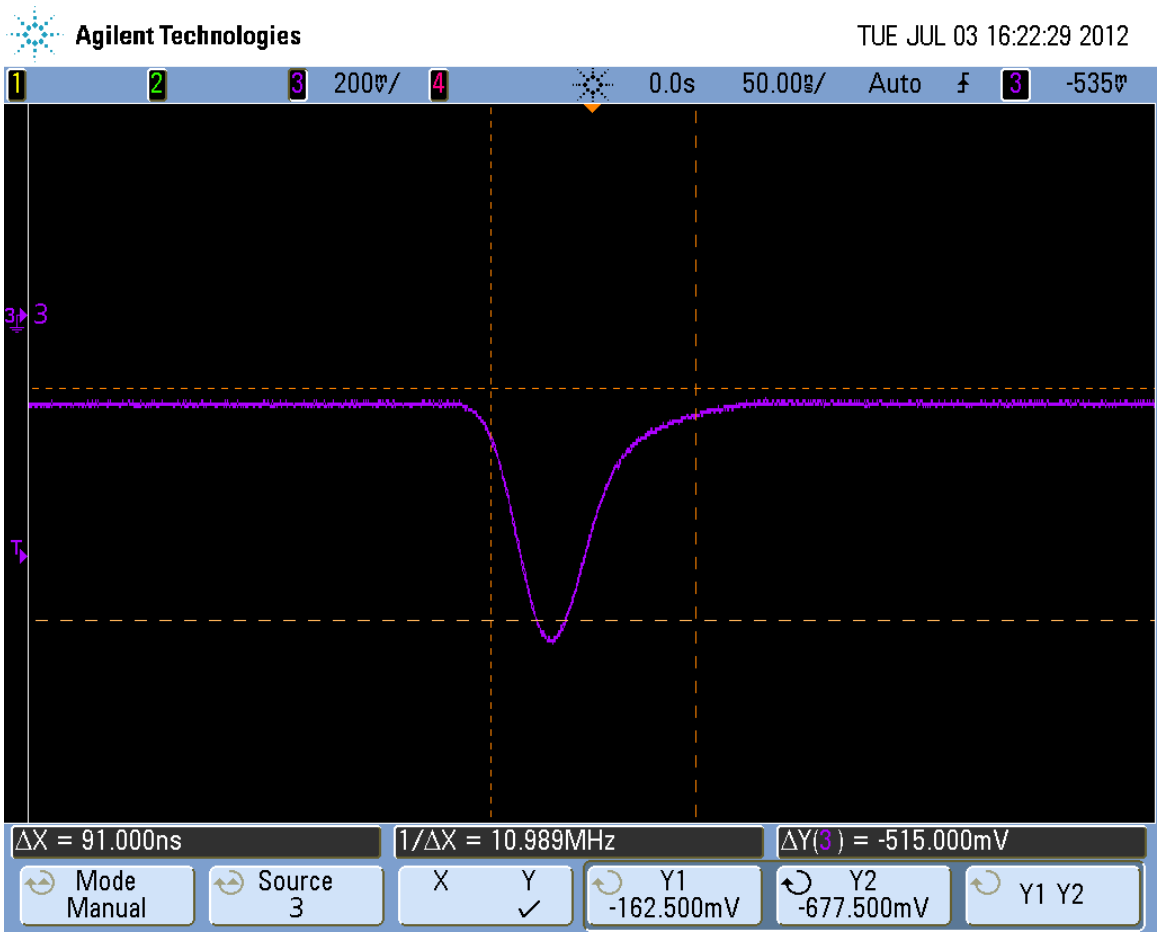

Figure C.9: A sample voltage pulse from the MPPCs

and can provide reliable statistics. The dark rates can vary for a single MPPC by several kHz/K. Spectral stability is used because of it's sensitivity to the peak resolution at the bias voltage. Therefore, bias voltage stability can also be established. Optimal bias is also dependent on temperature, so a secondary check on temperature can be established.

Rate Stability Results

The FPGAs were set to require n_f =2 and t_f =150ns. The triggering rate of each fiber channel and sum channel was then recorded and logged with the results presented in Figure C.12. Each point represents a fiber channel and sum channel where the value is the mean trigger rate over the course of an hour. The error bars represent RMS error for each value (y) and the run length (x).

Statistics demand that since the sum channels for each of the panels trigger each time a fiber coincidence causes a trigger, the sum channel rates are higher. Therefore, the sum channel rate, R_{sum} can be calculated as a function of the channel rates, R_{MPPC}, n_f and t_f.

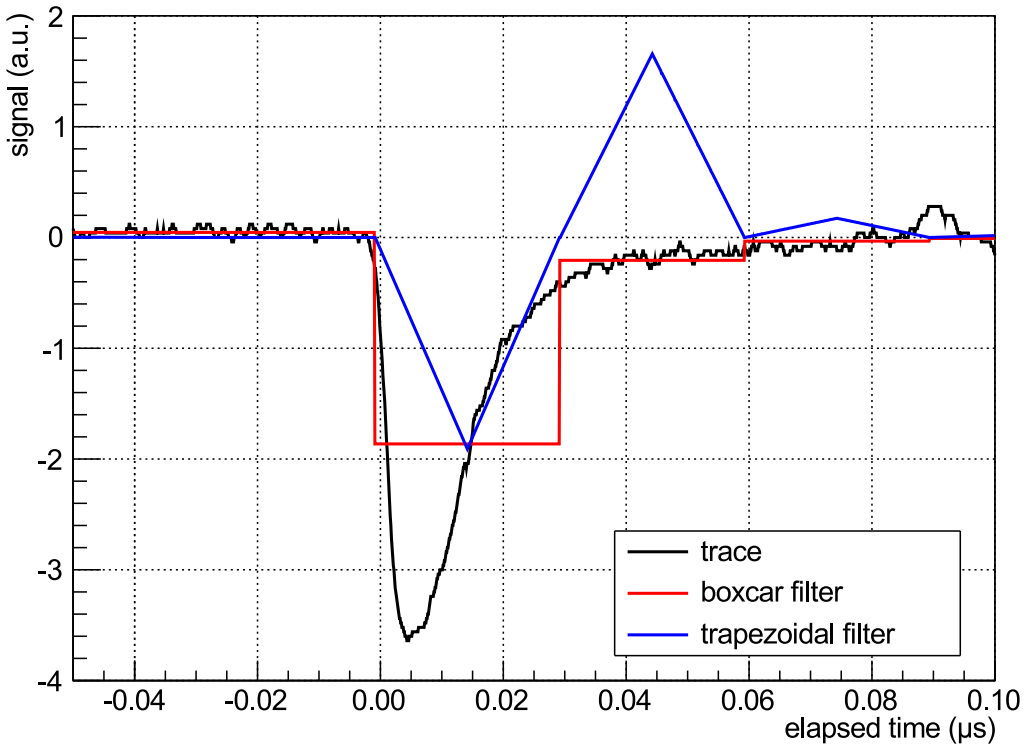

Figure C.10: A simulated veto signal going into the Mark IV crate, the old trapezoidal filter(blue) and the new boxcar filter (red). Image courtesy of [70].

$$R_{sum} = \frac{1}{t_f} \sum_{(i=n_f)}^{6} \sum_{MPPCs} \left[\prod_{(MPPC\ in\ set)} R_{MPPC} * t_f \right] \left[\prod_{(MPPCs\ not\ in\ set)} (1 - R_{MPPC} * t_f) \right] \quad \text{(C.0.1)}$$

Each of the panels is consistent with Poisson statistics showing good stability.

Spectral Stability Results

From the same data that produced the rate stability results, the spectral stability was also analyzed. This was accomplished by histogramming the ADC values for each of the hour long data sets and finding the peak values for each p.e. peak. The peak values are then tracked for each channel as shown in figure C.14.

For channels connected with the long panels, this results in a stable peak values as shown in figure C.14. However, for channels connected to the end-cap panels, the dark rate was too low to provide sufficient events for the analysis software to perform reliably.

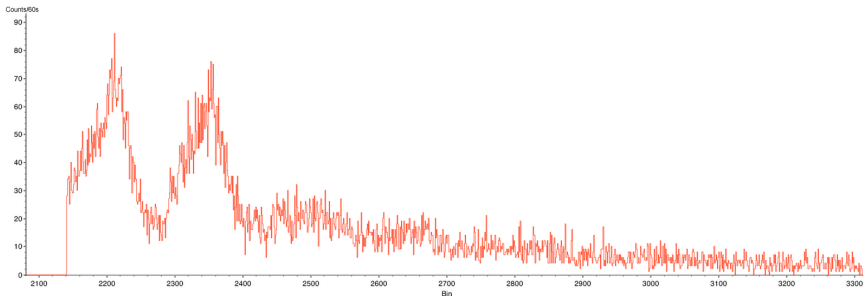

(A)

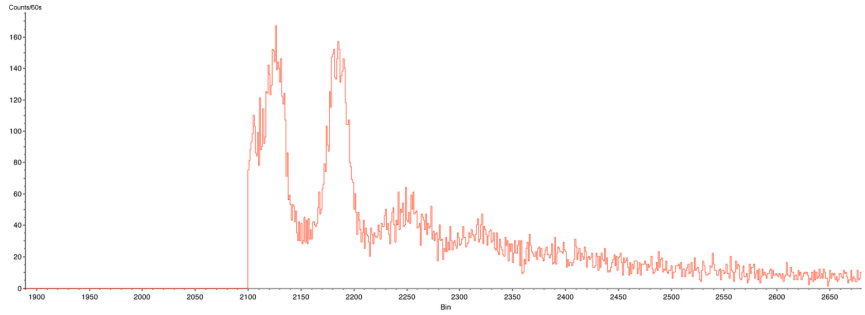

(B)

Figure C.11: The digitized peaks in the old filter (A) and the new filter (B). This shows the difference in peak resolution.

Therefore, reliable operation is demonstrated in rates for all channels and spectral stability for channels connected to the long panels. This approach was to continually check the system for performance during commissioning measurements.

Efficiency

With the system built and tested for reliability, the efficiency needed to be measured in order to show that performance goals were met.

The hardware setup used in the efficiency test was a hodoscope configuration. Panel were stacked vertically, as shown in figure C.15. This allows for cosmically-generated particles to hit multiple panels and produce coincident signals between panels that were used to calculate efficiency.

Given that a signal is defined in a panel as a coincidence between fibers in that panel, then coincidences between at least two panels can be used to trigger on cosmic muons (How signals are defined within a panel will be discussed below). Efficiency in a panel is therefore defined as the number of events the panel participates in detecting divided by the number of events that it does not participate in detecting. Since there are four long panels in the coincidence testing setup, then for a given panel, we can use the number of coincidence seen by all panels divided by the number of coincidence events seen by the other three panels. Similarly, subsets of three panels can also be used to generate efficiencies.

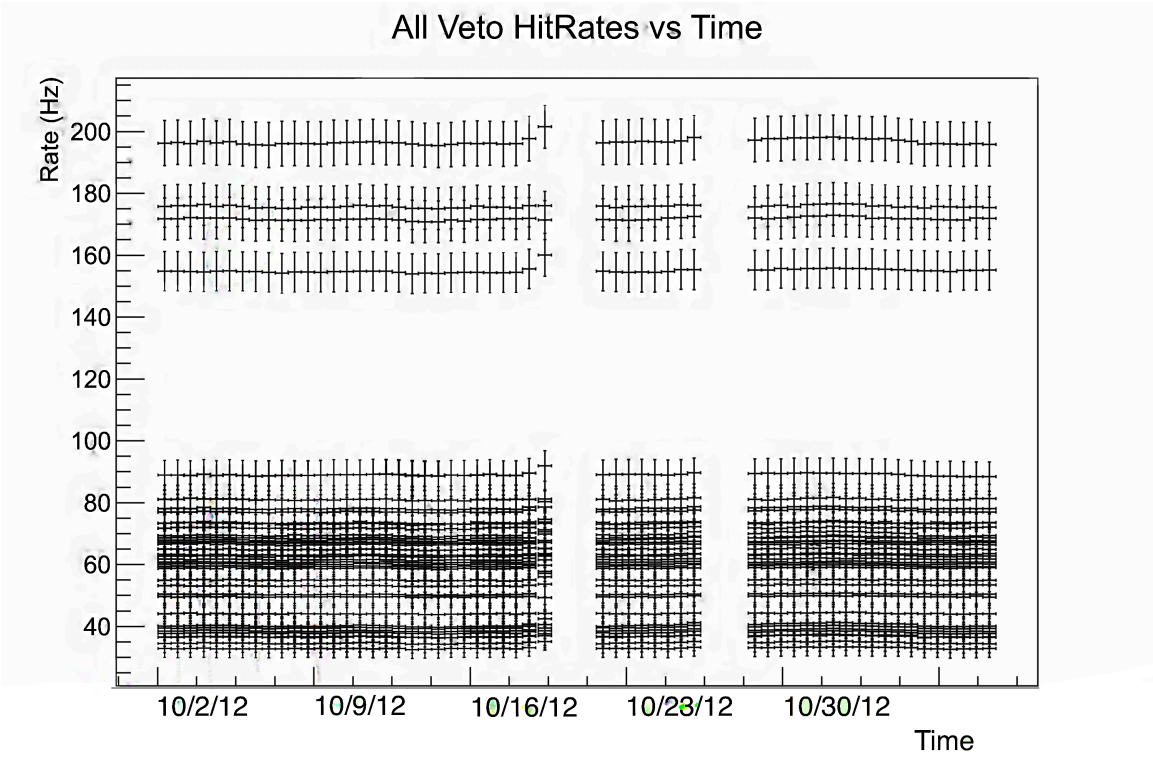

Figure C.12: FPGA triggering rates for each of the MPPCs and sum channels over the course of a month. There are two small breaks during which the system was being worked on. A high point was also visible during which the nitrogen feed had run dry. The four high rate traces are the sum channels for each of the panels. The lowest rate traces represent the end caps.

What is left is to define how a event is triggered in a single panel. As was discussed previously, the FPGAs allow the user to define n_f and t_f as well as triggering voltages for each fiber channel and sum channel. For this measurement, n_f and t_f were left as open parameters and data were taken at each possible permutation.

Data were taken for 6 hours at each possible configuration. The data were then analyzed for the types of coincidences described above. The last available parameter available for utilization is the coincidence window between panels, which will be called t_p. This generates a number for efficiency for each panel given n_f, t_f, t_p and the possible permutation of panels mentioned in the setup. A slice of the parameter space is shown in Figure C.16.

At this point accidental events were generated in a similar fashion by disconnecting the MPPCs from the panels. This generates a second data set which can be used to compare against the efficiency data set. In order to find optimal parameters for finding the efficiency, an optimization parameter was created as a function of the derivative of the efficiency and dark rate with respect to the each of the parameters used to generate them.

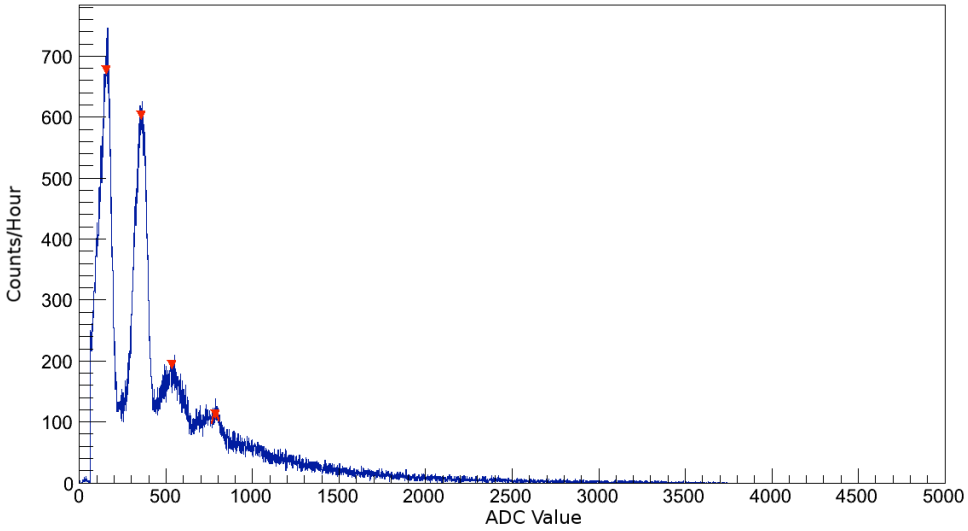

Figure C.13: MPPC pulse amplitude digitized and histogrammed over the course of an hour. Each P.E. peak is marked with a red arrow.

$$Optimizaton\ Parameter = \frac{\partial}{\partial n_f, t_f, t_p} Efficiency - \frac{\partial}{\partial n_f, t_f, t_p} Dark\ Rate \tag{C.0.2}$$

This test was repeated twice in order to measure the efficiency in 2 spare panels. The four panels with the highest efficiency were then used in the final apparatus.

For the end caps, a similar setup was used except with the three end caps where the 2 end caps with the highest efficiency were then used.

Efficiency Results

Panel Number (Type)	Efficiency (%)	Difference Between Studies (%)
6(Long)	91.80	0.49
7(Long)	71.79	1.36
1(Long)	84.21	1.09
2(Long)	96.45	3.01
8(Long)	94.57	2.66
3(Long)	65.19	0.21
5(End Cap)	97.61	0.02
8(End Cap)	98.10	0.01
6(End Cap)	98.75	0.0001

Table C.1: The individual efficiencies measured for each panel. Note that panel 3 was found to have a broken fiber accounting for it's low efficiency. In conjunction with the low errors found in the analysis, this would indicate that a likely suspect for low efficiencies, for example panel number 7, is light-transport related.

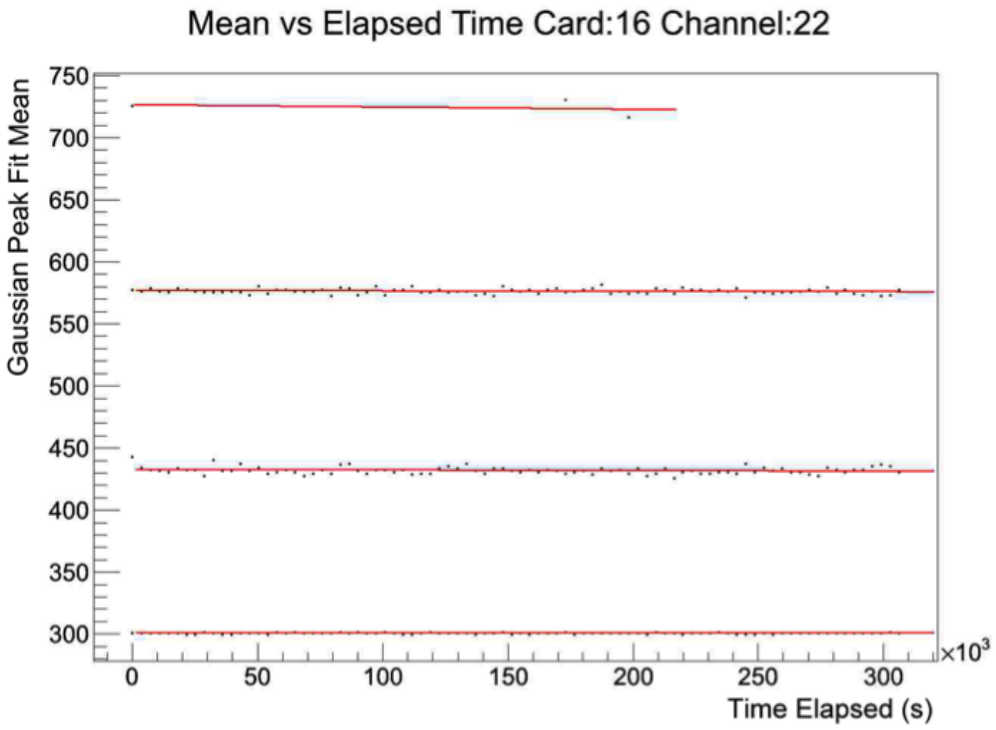

Figure C.14: P.E. peak means plotted over a period of time.

The results of this procedure is that the optimal parameters to run the system at are a fiber coincidence window of 150ns and a requirement of 2 coincident fibers to define an event. For these parameters, the efficiencies in Table C.1 were calculated. Given that each panel could be measured for efficiency using three different permutations of panels, the maximum difference between values generated for each study was also found. The projected total efficiency is the percentage of events detectable by the system, which can also be expressed in terms of the number of undetected events:

$$\epsilon_{tot} = \frac{N_{detected}}{N_{total}} = 1 - \frac{N_{undetected}}{N_{total}} \tag{C.0.3}$$

$$= 1 - (N_{into\ gap} + N_{undetected\ by\ 2\ panels} + N_{undetected\ by\ 1\ panel})/N_{total} \tag{C.0.4}$$

Every event can only be incident on 0, 1, or 2 panels. The fraction of events incident on no panels, denoted as $f_{gap} = N_{into\ gap}/N_{total}$ represent the fraction of events which hit the detector, but are not incident on any panel. For the fraction of events that are incident on two panels, the fraction of the total acceptance angle, f_{ij}, that hit both, and the efficiency of each panel, ϵ_i give rise to the third term in equation C.0.5. Similarly, for events that go unseen through a single panel, the geometric acceptance of the panel and the gap is given by f_{ii}, gives rise to the last term. A monte

Figure C.15: The physical setup of the efficiency test.

carlo simulation was done at MIT [90] to estimate the geometric acceptance of each panel or set of two panels, the gap and the detector face in order to produce the total projected efficiency:

$$\epsilon_{tot} = 1 - f_{gap} - \sum_{i=1}^{6}\sum_{j<i}(1-\epsilon_i)(1-\epsilon_j)f_{ij} - \sum_{i=1}^{6}(1-\epsilon_i)f_{ii} \tag{C.0.5}$$

The projected total system efficiency was found to be 97.1%±0.88. It should be noted that the error on this value was calculated based off the measurement differences above and propagated through. This does not contain the error from the Monte Carlo calculations of geometric acceptance due to the absence of those values. This value does, however, meet the specifications of the system.

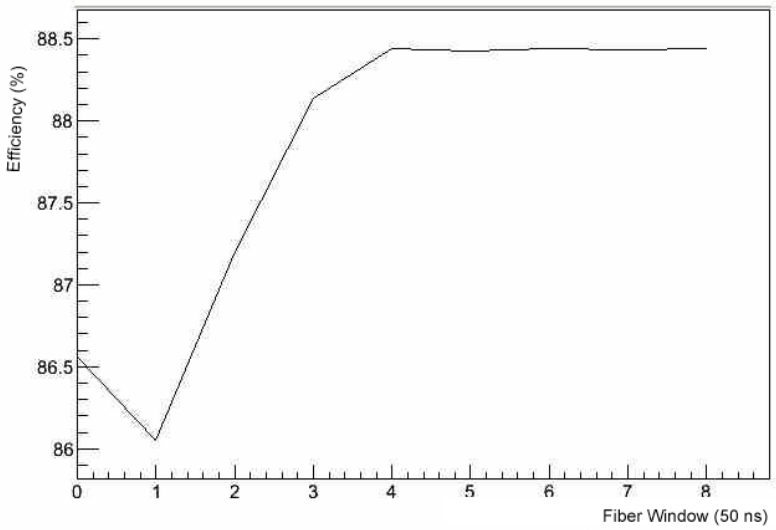

Figure C.16: Efficiencies for the panel with serial number 3 as a function of it's fiber coincidence window, given 200ns coincidence between panels, and using panels 6 and 7 to generate cosmic event triggers.

BIBLIOGRAPHY

[1] W. Pauli, "Letter to the Physical Institute of Federal Institute of Technology, Zürich", Dec. 1930.

[2] W. E. F. Pauli, R. Kronig, and V. F. Weisskopf, *Collected scientific papers* (Interscience, New York, NY, 1964).

[3] G. Danby, J.-M. Gaillard, K. Goulianos, L. M. Lederman, N. Mistry, M. Schwartz, and J. Steinberger, "Observation of High-Energy Neutrino Reactions and the Existence of Two Kinds of Neutrinos", Phys. Rev. Lett. **9**, 36–44 (1962).

[4] C. MARIANI, "Review of Reactor Neutrino Oscillation Experiments", Modern Physics Letters A **27**, 1230010 (2012).

[5] M. L. Perl, G. S. Abrams, A. M. Boyarski, M. Breidenbach, D. D. Briggs, F. Bulos, W. Chinowsky, J. T. Dakin, G. J. Feldman, C. E. Friedberg, D. Fryberger, G. Goldhaber, G. Hanson, F. B. Heile, B. Jean-Marie, J. A. Kadyk, R. R. Larsen, A. M. Litke, D. Lüke, B. A. Lulu, V. Lüth, D. Lyon, C. C. Morehouse, J. M. Paterson, F. M. Pierre, T. P. Pun, P. A. Rapidis, B. Richter, B. Sadoulet, R. F. Schwitters, W. Tanenbaum, G. H. Trilling, F. Vannucci, J. S. Whitaker, F. C. Winkelmann, and J. E. Wiss, "Evidence for Anomalous Lepton Production in ${e}^{+}-{e}^{-}$ Annihilation", Phys. Rev. Lett. **35**, 1489–1492 (1975).

[6] E. Fermi, "Versuch einer Theorie der β-Strahlen.", Zeitschrift für Physik **88**, 161–177 (1934).

[7] E. Henley, H. Frauenfelder, and A. García, *Subatomic physics.* 3rd ed. / (World Scientific, Hackensack, N.J., 2007).

[8] C. S. Wu, E. Ambler, R. W. Hayward, D. D. Hoppes, and R. P. Hudson, "Experimental Test of Parity Conservation in Beta Decay", Phys. Rev. **105**, 1413–1415 (1957).

[9] M. Goldhaber, L. Grodzins, and A. W. Sunyar, "Helicity of Neutrinos", Phys. Rev. **109**, 1015–1017 (1958).

[10] "The MicroBooNE Technical Design Report",

[11] C. Rubbia, M. Antonello, P. Aprili, B. Baibussinov, M. B. Ceolin, L. Barzè, P. Benetti, E. Calligarich, N. Canci, F. Carbonara, F. Cavanna, S. Centro, A. Cesana, K. Cieslik, D. B. Cline, A. G. Cocco, A. Dabrowska, D. Dequal, A. Dermenev, R. Dolfini, C. Farnese, A. Fava, A. Ferrari, G. Fiorillo, D. Gibin, A. G. Berzolari, S. Gninenko, T. Golan, A. Guglielmi, M. Haranczyk, J. Holeczek, P. Karbowniczek, M. Kirsanov, J. Kisiel, I. Kochanek, J. Lagoda, M. Lantz, S. Mania, G. Mannocchi, F. Mauri, A. Menegolli, G. Meng, C. Montanari, S. Muraro, S. Otwinowski, O. Palamara, T. J. Palczewski, L. Periale, A. Piazzoli, P. Picchi, F. Pietropaolo, P. Plonski, M. Prata, P. Przewlocki, A. Rappoldi, G. L. Raselli, M. Rossella, P. Sala, E. Scantamburlo, A. Scaramelli, E. Segreto, F. Sergiampietri, J. Sobczyk, D. Stefan, J. Stepaniak, R. Sulej, M. Szarska, M. Terrani, F. Varanini, S. Ventura, C. Vignoli, T. Wachala, H. Wang, X. Yang, A. Zalewska, K. Zaremba, J. Zmuda, F. H. et Al., C. Rubbia, S. A. et Al., A. A. et Al., S. A. et Al., P. B. et Al., P. C. et Al., F. A. et Al., F. A. et Al., T. L. B. Kegl, A. Krzyzak, K. Zeger, A. A. et al. ICARUS collaboration, S. A. et al. ICARUS collaboration, A. A. et Al., S. A. et Al., F. A. et Al., R. B. et Al., D. A. et Al., and B. B. et Al., "Underground operation of the ICARUS T600 LAr-TPC: first results", Journal of Instrumentation **6**, P07011–P07011 (2011).

[12] A. B. Sousa, "Long-Baseline Neutrino Oscillation Experiments",

[13] K. A. Olive, et al., "Review of Particle Physics", Chin. Phys. **C38**, 90001 (2014).

[14]M. Babutzka, *Untersuchung eines verfahrbaren Monitordetektors zur Überwachung der Aktivität des β-Zerfalls in der kryogenen Pumpstrecke des KATRIN-Experiments*, Diploma Thesis (2010).

[15] Abe, K. et al. (T2K Collaboration), "Observation of Electron Neutrino Appearance in a Muon Neutrino Beam", Physical Review Letters **112**, 061802 (2014).

[16]E. Majorana, "Teoria simmetrica dell'elettrone e del positrone", Il Nuovo Cimento **14**, 171–184 (1937).

[17]C. Iliadis, *Nuclear physics of stars (Second, revised and enlarged ed.)* (Weinheim, Germany: Wiley-VCH Verlag GmbH and Co. KGaA, 2015).

[18]P. Planck Collaboration, P. A. R. Ade, N. Aghanim, M. Arnaud, M. Ashdown, J. Aumont, C. Baccigalupi, A. J. Banday, R. B. Barreiro, J. G. Bartlett, N. Bartolo, E. Battaner, R. Battye, K. Benabed, A. Benoit, A. Benoit-Levy, J. .-.-P. Bernard, M. Bersanelli, P. Bielewicz, J. J. Bock, A. Bonaldi, L. Bonavera, J. R. Bond, J. Borrill, F. R. Bouchet, F. Boulanger, M. Bucher, C. Burigana, R. C. Butler, E. Calabrese, J. .-.-F. Cardoso, A. Catalano, A. Challinor, A. Chamballu, R. .-.-R. Chary, H. C. Chiang, J. Chluba, P. R. Christensen, S. Church, D. L. Clements, S. Colombi, L. P. L. Colombo, C. Combet, A. Coulais, B. P. Crill, A. Curto, F. Cuttaia, L. Danese, R. D. Davies, R. J. Davis, P. de Bernardis, A. de Rosa, G. de Zotti, J. Delabrouille, F. .-.-X. Desert, E. Di Valentino, C. Dickinson, J. M. Diego, K. Dolag, H. Dole, S. Donzelli, O. Dore, M. Douspis, A. Ducout, J. Dunkley, X. Dupac, G. Efstathiou, F. Elsner, T. A. Ensslin, H. K. Eriksen, M. Farhang, J. Fergusson, F. Finelli, O. Forni, M. Frailis, A. A. Fraisse, E. Franceschi, A. Frejsel, S. Galeotta, S. Galli, K. Ganga, C. Gauthier, M. Gerbino, T. Ghosh, M. Giard, Y. Giraud-Heraud, E. Giusarma, E. Gjerlow, J. Gonzalez-Nuevo, K. M. Gorski, S. Gratton, A. Gregorio, A. Gruppuso, J. E. Gudmundsson, J. Hamann, F. K. Hansen, D. Hanson, D. L. Harrison, G. Helou, S. Henrot-Versille, C. Hernandez-Monteagudo, D. Herranz, S. R. Hildebrandt, E. Hivon, M. Hobson, W. A. Holmes, A. Hornstrup, W. Hovest, Z. Huang, K. M. Huffenberger, G. Hurier, A. H. Jaffe, T. R. Jaffe, W. C. Jones, M. Juvela, E. Keihanen, R. Keskitalo, T. S. Kisner, R. Kneissl, J. Knoche, L. Knox, M. Kunz, H. Kurki-Suonio, G. Lagache, A. Lahteenmaki, J. .-.-M. Lamarre, A. Lasenby, M. Lattanzi, C. R. Lawrence, J. P. Leahy, R. Leonardi, J. Lesgourgues, F. Levrier, A. Lewis, M. Liguori, P. B. Lilje, M. Linden-Vornle, M. Lopez-Caniego, P. M. Lubin, J. F. Macias-Perez, G. Maggio, D. Maino, N. Mandolesi, A. Mangilli, A. Marchini, P. G. Martin, M. Martinelli, E. Martinez-Gonzalez, S. Masi, S. Matarrese, P. Mazzotta, P. McGehee, P. R. Meinhold, A. Melchiorri, J. .-.-B. Melin, L. Mendes, A. Mennella, M. Migliaccio, M. Millea, S. Mitra, M. .-.-A. Miville-Deschenes, A. Moneti, L. Montier, G. Morgante, D. Mortlock, A. Moss, D. Munshi, J. A. Murphy, P. Naselsky, F. Nati, P. Natoli, C. B. Netterfield, H. U. Norgaard-Nielsen, F. Noviello, D. Novikov, I. Novikov, C. A. Oxborrow, F. Paci, L. Pagano, F. Pajot, R. Paladini, D. Paoletti, B. Partridge, F. Pasian, G. Patanchon, T. J. Pearson, O. Perdereau, L. Perotto, F. Perrotta, V. Pettorino, F. Piacentini, M. Piat, E. Pierpaoli, D. Pietrobon, S. Plaszczynski, E. Pointecouteau, G. Polenta, L. Popa, G. W. Pratt, G. Prezeau, S. Prunet, J. .-.-L. Puget, J. P. Rachen, W. T. Reach, R. Rebolo, M. Reinecke, M. Remazeilles, C. Renault, A. Renzi, I. Ristorcelli, G. Rocha, C. Rosset, M. Rossetti, G. Roudier, B. R. D'Orfeuil, M. Rowan-Robinson, J. A. Rubino-Martin, B. Rusholme, N. Said, V. Salvatelli, L. Salvati, M. Sandri, D. Santos, M. Savelainen, G. Savini, D. Scott, M. D. Seiffert, P. Serra, E. P. S. Shellard, L. D. Spencer, M. Spinelli, V. Stolyarov, R. Stompor, R. Sudiwala, R. Sunyaev, D. Sutton, A. .-.-S. Suur-Uski, J. .-.-F. Sygnet, J. A. Tauber, L. Terenzi, L. Toffolatti, M. Tomasi, M. Tristram, T. Trombetti, M. Tucci, J. Tuovinen, M. Turler, G. Umana, L. Valenziano, J. Valiviita, B. Van Tent, P. Vielva, F. Villa, L. A. Wade, B. D. Wandelt, I. K. Wehus, M. White, S. D. M. White, A. Wilkinson, D. Yvon, A. Zacchei, and A. Zonca, "Planck 2015 results. XIII. Cosmological parameters", (2015).

[19]J. L. Pastor, and S., "Neutrino Mass from Cosmology," Adv. in High Energy Phys **2012** (2012).

[20]M. Goeppert-Mayer, "Double Beta-Disintegration", Physical Review **48**, 512–516 (1935).

[21] A. Giuliani, A. Poves, A. Giuliani, and A. Poves, "Neutrinoless Double-Beta Decay", Advances in High Energy Physics **2012**, 1–38 (2012).

[22] The EXO-200 Collaboration, "Search for Majorana neutrinos with the first two years of EXO-200 data", Nature **510**, 229–234 (2014).

[23] M. Agostini, M. Allardt, E. Andreotti, A. M. Bakalyarov, M. Balata, I. Barabanov, M. Barnabe Heider, N. Barros, L. Baudis, C. Bauer, N. Becerici-Schmidt, E. Bellotti, S. Belogurov, S. T. Belyaev, G. Benato, A. Bettini, L. Bezrukov, T. Bode, V. Brudanin, R. Brugnera, D. Budj, A. Caldwell, C. Cattadori, A. Chernogorov, F. Cossavella, E. V. Demidova, A. Domula, V. Egorov, R. Falkenstein, A. Ferella, K. Freund, N. Frodyma, A. Gangapshev, A. Garfagnini, C. Gotti, P. Grabmayr, V. Gurentsov, K. Gusev, K. K. Guthikonda, W. Hampel, A. Hegai, M. Heisel, S. Hemmer, G. Heusser, W. Hofmann, M. Hult, L. V. Inzhechik, L. Ioannucci, J. Janicsk Csthy, J. Jochum, M. Junker, T. Kihm, I. V. Kirpichnikov, A. Kirsch, A. Klimenko, K. T. Knpfle, O. Kochetov, V. N. Kornoukhov, V. V. Kuzminov, M. Laubenstein, A. Lazzaro, V. I. Lebedev, B. Lehnert, H. Y. Liao, M. Lindner, I. Lippi, X. Liu, A. Lubashevskiy, B. Lubsandorzhiev, G. Lutter, C. Macolino, A. A. Machado, B. Majorovits, W. Maneschg, M. Misiaszek, I. Nemchenok, S. Nisi, C. O'Shaughnessy, L. Pandola, K. Pelczar, G. Pessina, A. Pullia, S. Riboldi, N. Rumyantseva, C. Sada, M. Salathe, C. Schmitt, J. Schreiner, O. Schulz, B. Schwingenheuer, S. Schnert, E. Shevchik, M. Shirchenko, H. Simgen, A. Smolnikov, L. Stanco, H. Strecker, M. Tarka, C. A. Ur, A. A. Vasenko, O. Volynets, K. Von Sturm, V. Wagner, M. Walter, A. Wegmann, T. Wester, M. Wojcik, E. Yanovich, P. Zavarise, I. Zhitnikov, S. V. Zhukov, D. Zinatulina, K. Zuber, and G. Zuzel, "Results on Neutrinoless Double-\beta Decay of 76Ge from Phase I of the GERDA Experiment", Physical Review Letters **111**, 122503 (2013).

[24] R. L. Awasthi, M. Mitra, and A. Dasgupta, *Limiting the Effective Mass and New Physics Parameters from 0nubetabeta*, 2016.

[25] J. B. Albert, M. Auger, D. J. Auty, P. S. Barbeau, E. Beauchamp, D. Beck, V. Belov, C. Benitez-Medina, J. Bonatt, M. Breidenbach, T. Brunner, A. Burenkov, G. F. Cao, C. Chambers, J. Chaves, B. Cleveland, S. Cook, T. Daniels, M. Danilov, S. J. Daugherty, C. G. Davis, J. Davis, S. Delaquis, R. DeVoe, A. Dobi, M. J. Dolinski, A. Dolgolenko, M. Dunford, W. Fairbank, J. Farine, W. Feldmeier, P. Fierlinger, D. Franco, D. Fudenberg, G. Giroux, R. Gornea, K. Graham, G. Gratta, C. Hall, K. Hall, C. Hargrove, S. Herrin, M. Hughes, X. S. Jiang, A. Johnson, T. N. Johnson, S. Johnston, A. Karelin, L. J. Kaufman, R. Killick, S. Kravitz, A. Kuchenkov, K. S. Kumar, D. S. Leonard, F. Leonard, C. Licciardi, R. MacLellan, M. G. Marino, B. Mong, M. M. Díez, D. Moore, R. Nelson, A. Odian, I. Ostrovskiy, K. O'Sullivan, C. Ouellet, A. Piepke, A. Pocar, C. Y. Prescott, A. Rivas, P. C. Rowson, M. P. Rozo, J. J. Russell, A. Sabourov, D. Sinclair, K. Skarpaas, S. Slutsky, V. Stekhanov, V. Strickland, M. Tarka, T. Tolba, D. Tosi, K. Twelker, P. Vogel, J. .-.-L. Vuilleumier, A. Waite, J. Walton, T. Walton, M. Weber, L. J. Wen, U. Wichoski, J. Wodin, J. D. Wright, L. Yang, Y. .-.-R. Yen, O. Y. Zeldovich, and Y. B. Zhao, "An improved measurement of the 2\nu \beta \beta\ half-life of Xe-136 with EXO-200", (2013) 10.1103/PhysRevC.89.015502.

[26] G. Drexlin, V. Hannen, S. Mertens, and C. Weinheimer, "Current direct neutrino mass experiments", Advances in High Energy Physics **2013** (2013) 10.1155/2013/293986.

[27] V. N. Aseev, A. I. Belesev, A. I. Berlev, E. V. Geraskin, A. A. Golubev, N. A. Likhovid, V. M. Lobashev, A. A. Nozik, V. S. Pantuev, V. I. Parfenov, A. K. Skasyrskaya, F. V. Tkachov, and S. V. Zadorozhny, "Upper limit on the electron antineutrino mass from the Troitsk experiment", Physical Review D **84**, 112003 (2011).

[28] C. Kraus, B. Bornschein, L. Bornschein, J. Bonn, B. Flatt, A. Kovalik, B. Ostrick, E. W. Otten, J. P. Schall, T. Thümmler, and C. Weinheimer, "Final results from phase II of the Mainz neutrino

mass search in tritium β decay", The European Physical Journal C - Particles and Fields **40**, 447–468 (2005).

[29] A. Saenz, S. Jonsell, and P. Froelich, "Improved Molecular Final-State Distribution of HeT for the beta -Decay Process of T2", Physical Review Letters **84**, 242–245 (2000).

[30] A. Saenz, and P. Froelich, "Effect of final-state interactions in allowed β decays. {II}. {Reliability} of the β-decay spectrum for T2", Physical Review C **56**, 2162–2184 (1997).

[31] A. Saenz, S. Jonsell, and P. Froelich, "Improved Molecular Final-State Distribution of HeT+ for the β-Decay Process of T2", Physical Review Letters **84**, 242–245 (2000).

[32] L. I. Bodine, D. S. Parno, and R. G. H. Robertson, "Assessment of molecular effects on neutrino mass measurements from tritium β decay", Physical Review C **91**, 035505 (2015).

[33] B. Monreal, "The Project 8 Radiofrequency Tritium Neutrino Experiment", Physics procedia **61**, 274–277 (2015).

[34] A. Faessler, C. Enss, L. Gastaldo, and F. Šimkovic, "Determination of the neutrino mass by electron capture in Ho 163 and the role of the three-hole states in Dy 163", Physical review. C, Nuclear physics **91** (2015) 10.1103/PhysRevC.91.064302.

[35] R. G. H. Robertson, "Examination of the calorimetric spectrum to determine the neutrino mass in low-energy electron capture decay", Physical Review C **91**, 035504 (2015).

[36] The DOE/NSF Nuclear Science Advisory Committee, *Long Range Plan*, tech. rep. (DOE, NSF, Washington, DC, 2015).

[37] G. Beamson, H. Q. Porter, and D. W. Turner, "The collimating and magnifying properties of a superconducting field photoelectron spectrometer", Journal of Physics E: Scientific Instruments **13**, 64 (1980).

[38] A. Picard, H. Backe, H. Barth, J. Bonn, B. Degen, T. Edling, R. Haid, A. Hermanni, P. Leiderer, T. Loeken, A. Molz, R. B. Moore, A. Osipowicz, E. W. Otten, M. Przyrembel, M. Schrader, M. Steininger, and C. Weinheimer, "A solenoid retarding spectrometer with high resolution and transmission for keV electrons", Nuclear Instruments and Methods in Physics Research Section B: Beam Interactions with Materials and Atoms **63**, 345–358 (1992).

[39] KATRIN, "KATRIN Design Report", FZKA scientific report **7090** (2005).

[40] S. Groh, "Modeling of the response function and measurement of transmission properties of the KATRIN experiment", PhD thesis (Das Karlsruher Institut für Technologie, Karlsruhe, 2015).

[41] K. Valerius, "Spectrometer-related background processes and their suppression in the KATRIN experiment", PhD thesis (Universität Münster, 2009).

[42] M. Noe, R. Gehring, S. Grohmann, H. Neumann, O. Kazachenko, B. Bornschein, and J. Bonn, "The development of the KATRIN magnet system", Journal of Physics: Conference Series **43**, 710 (2006).

[43] F. Fränkle, "Erste Messungen der elektromagnetischen Eigenschaften des KATRIN Vorspektrometers", PhD thesis (Das Karlsruher Institut für Technologie, 2006).

[44]T. Thümmler, "Präzisionsüberwachung und Kalibration der Hochspannung für das KATRIN-Experiment", PhD thesis (2007).

[45]B. Müller, "Umbau des Mainzer Neutrinomassenexperiments und Untergrunduntersuchungen im Hinblick auf KATRIN", PhD thesis (2002).

[46]B. Flatt, "Designstudien für das KATRIN Experiment", PhD thesis (2001).

[47]M. Beck, K. Valerius, J. Bonn, K. Essig, F. Glück, H. W. Ortjohann, B. Ostrick, E. W. Otten, T. Thümmler, M. Zbořil, and C. Weinheimer, "Effect of a sweeping conductive wire on electrons stored in a Penning-like trap between the KATRIN spectrometers", The European Physical Journal A **44**, 499–511 (2010).

[48]M. Prall, "Aufbau und Test des Gaseinlasssystems für die kondensierte 83Kr-Kalibrationsquelle des KATRIN-Experimentes", PhD thesis (2005).

[49]B. Hillen, "Untersuchung von Methoden zur Unterdr{ü}ckung des Spektrometeruntergrunds beim KATRIN Experiment", PhD thesis (2011).

[50]K. Hugenberg, "Design of the electrode system of the KATRIN main spectrometer", PhD thesis (2008).

[51]F. M. Fränkle, F. Glück, K. Valerius, K. Bokeloh, A. Beglarian, J. Bonn, L. Bornschein, G. Drexlin, F. Habermehl, M. L. Leber, A. Osipowicz, E. W. Otten, M. Steidl, T. Thümmler, C. Weinheimer, J. F. Wilkerson, J. Wolf, and S. V. Zadorozhny, "Penning discharge in the KATRIN pre-spectrometer", Journal of Instrumentation **9**, P07028 (2014).

[52]A. Kriesch, *File:Penning Trap.svg*, 2006.

[53]J. D. Jackson, *Classical electrodynamics* (Wiley, 1999), p. 808.

[54]S. J. Freedman, and B. Kayser, "The Neutrino Matrix", arXiv:physics/0411216 **v2** (2004).

[55]J. Behrens, "Simulations of stored electrons in the Penning trap between the KATRIN spectrometers", Diploma Thesis (Universität Münster, 2012).

[56]D. Hilk, "Berechnung der elektronische Potenzialverschiebung in einem 2-Phasen Edelgas-Detektor", Diploma Thesis (KIT, 2012).

[57]N. Wandkowsky, "Design and Background Simulations for the KATRIN Main Spectrometer and Air Coil System", PhD thesis (Das Karlsruher Institut für Technologie, 2009).

[58]M. Babutzka, M. Bahr, J. Bonn, B. Bornschein, A. Dieter, G. Drexlin, K. Eitel, S. Fischer, F. Glück, S. Grohmann, M. Hötzel, T. M. James, W. Käfer, M. Leber, B. Monreal, F. Priester, M. Röllig, M. Schlösser, U. Schmitt, F. Sharipov, M. Steidl, M. Sturm, H. H. Telle, and N. Titov, "Monitoring of the operating parameters of the KATRIN Windowless Gaseous Tritium Source", New Journal of Physics **14**, 103046 (2012).

[59]M. Hötzel, *Berechnung von KATRIN Messspektren unter Einbeziehung der Eigenschaften der fensterlosen gasförmigen Tritiumquelle*, tech. rep. (KIT, 2009).

[60]S. Lukić, B. Bornschein, L. Bornschein, G. Drexlin, A. Kosmider, K. Schlösser, and A. Windberger, "Measurement of the gas-flow reduction factor of the KATRIN DPS2-F differential pumping section", Vacuum **86**, 1126–1133 (2012).

[61]W. Gil, J. Bonn, B. Bornschein, R. Gehring, O. Kazachenko, J. Kleinfeller, and S. Putselyk, "The Cryogenic Pumping Section of the KATRIN Experiment", IEEE Transactions on Applied Superconductivity **20**, 316–319 (2010).

[62]M. Zacher, "Electromagnetic design and field emission studies for the inner electrode system of the KATRIN main spectrometer", PhD thesis (2009).

[63]M. Arenz, M. Babutzka, M. Bahr, J. P. Barrett, S. Bauer, M. Beck, A. Beglarian, J. Behrens, T. Bergmann, U. Besserer, J. Blümer, L. I. Bodine, K. Bokeloh, J. Bonn, B. Bornschein, L. Bornschein, S. Büsch, T. H. Burritt, S. Chilingaryan, T. J. Corona, L. De Viveiros, P. J. Doe, O. Dragoun, G. Drexlin, S. Dyba, S. Ebenhöch, K. Eitel, E. Ellinger, S. Enomoto, M. Erhard, D. Eversheim, M. Fedkevych, A. Felden, S. Fischer, J. A. Formaggio, F. Fränkle, D. Furse, M. Ghilea, W. Gil, F. Glück, A. G. Urena, S. Görhardt, S. Groh, S. Grohmann, R. Grössle, R. Gumbsheimer, M. Hackenjos, V. Hannen, F. Harms, N. Hauÿmann, F. Heizmann, K. Helbing, W. Herz, S. Hickford, D. Hilk, B. Hillen, T. Höhn, B. Holzapfel, M. Hötzel, M. A. Howe, A. Huber, A. Jansen, N. Kernert, L. Kippenbrock, M. Kleesiek, M. Klein, A. Kopmann, A. Kosmider, A. Kovalík, B. Krasch, M. Kraus, H. Krause, M. Krause, L. Kuckert, B. Kuffner, L. La Cascio, O. Lebeda, B. Leiber, J. Letnev, V. M. Lobashev, A. Lokhov, E. Malcherek, M. Mark, E. L. Martin, S. Mertens, S. Mirz, B. Monreal, K. Müller, M. Neuberger, H. Neumann, S. Niemes, M. Noe, N. S. Oblath, A. Off, H. .-.-W. Ortjohann, A. Osipowicz, E. Otten, D. S. Parno, P. Plischke, A. W. P. Poon, M. Prall, F. Priester, P. C. .-.-O. Ranitzsch, J. Reich, O. Rest, R. G. H. Robertson, M. Röllig, S. Rosendahl, S. Rupp, M. Rysavy, K. Schlösser, M. Schlösser, K. Schönung, M. Schrank, J. Schwarz, W. Seiler, H. Seitz-Moskaliuk, J. Sentkerestiova, A. Skasyrskaya, M. Slezak, A. Spalek, M. Steidl, N. Steinbrink, M. Sturm, M. Suesser, H. H. Telle, T. Thümmler, N. Titov, I. Tkachev, N. Trost, A. Unru, K. Valerius, D. Venos, R. Vianden, S. Vöcking, B. L. Wall, N. Wandkowsky, M. Weber, C. Weinheimer, C. Weiss, S. Welte, J. Wendel, K. L. Wierman, J. F. Wilkerson, D. Winzen, J. Wolf, S. Wüstling, M. Zacher, S. Zadoroghny, and M. Zboril, "Commissioning of the vacuum system of the KATRIN Main Spectrometer", (2016) 10.1088/1748-0221/11/04/P04011.

[64]J. F. Amsbaugh, J. Barrett, A. Beglarian, T. Bergmann, H. Bichsel, L. I. Bodine, J. Bonn, N. M. Boyd, T. H. Burritt, Z. Chaoui, S. Chilingaryan, T. J. Corona, P. J. Doe, J. A. Dunmore, S. Enomoto, J. Fischer, J. A. Formaggio, F. M. Fränkle, D. Furse, H. Gemmeke, F. Glück, F. Harms, G. C. Harper, J. Hartmann, M. A. Howe, A. Kaboth, J. Kelsey, M. Knauer, A. Kopmann, M. L. Leber, E. L. Martin, K. J. Middleman, A. W. Myers, N. S. Oblath, D. S. Parno, D. A. Peterson, L. Petzold, D. G. P. II, P. Renschler, R. G. H. Robertson, J. Schwarz, M. Steidl, D. Tcherniakhovski, T. Thümmler, T. D. V. Wechel, B. A. VanDevender, S. Vöcking, B. L. Wall, K. L. Wierman, J. F. Wilkerson, S. Wüstling, D. Phillips, P. Renschler, R. G. H. Robertson, J. Schwarz, M. Steidl, D. Tcherniakhovski, T. Thümmler, T. Van Wechel, B. A. VanDevender, S. Vöcking, B. L. Wall, K. L. Wierman, J. F. Wilkerson, and S. Wüstling, "Focal-plane detector system for the KATRIN experiment", Nuclear Instruments and Methods in Physics Research Section A: Accelerators, Spectrometers, Detectors and Associated Equipment **778**, 40–60 (2014).

[65]B. L. Wall, J. F. Amsbaugh, A. Beglarian, T. Bergmann, H. C. Bichsel, L. I. Bodine, N. M. Boyd, T. H. Burritt, Z. Chaoui, T. J. Corona, P. J. Doe, S. Enomoto, F. Harms, G. C. Harper, M. A. Howe, E. L. Martin, D. S. Parno, D. A. Peterson, L. Petzold, P. Renschler, R. G. H. Robertson, J. Schwarz, M. Steidl, T. D. V. Wechel, B. A. VanDevender, S. Wüstling, K. J. Wierman, and J. F. Wilkerson, "Dead layer on silicon pâ€"iâ€"n diode charged-particle detectors", Nuclear Instruments and Methods in Physics Research Section A: Accelerators, Spectrometers, Detectors and Associated Equipment **744**, 73–79 (2014).

[66]M. L. Leber, "Monte Carlo Calculations of the Intrinsic Detector Backgrounds for the Karlsruhe Tritium Neutrino Experiment", PhD thesis (2010).

[67]M. Howe, and J. Wilkerson, *ORCA Data Aquisition System*.

[68]M. A. Schumaker, A. Boeltzig, T. H. Burritt, C. A. Duba, F. A. Duncan, J. Farine, A. Habig, A. Hime, M. A. Howe, A. Kielbik, C. Kraus, K. Nicholson, R. G. H. Robertson, K. Scholberg, J. Secrest, T. C. Shantz, C. J. Virtue, J. F. Wilkerson, S. Yen, and K. Zuber, "Data acquisition for the Helium and Lead Observatory", in Ieee nuclear science symposuim & medical imaging conference (Oct. 2010), pp. 1860–1865.

[69]M. A. Howe, G. A. Cox, P. J. Harvey, F. McGirt, K. Rielage, J. F. Wilkerson, and J. M. Wouters, "Sudbury neutrino observatory neutral current detector acquisition software overview", IEEE Transactions on Nuclear Science **51**, 878–883 (2004).

[70]J. S. Schwarz, "The Detector System of the KATRIN Experiment - Implementation and First Measurements with the Spectrometer", PhD thesis (Das Karlsruher Institut für Technologie, 2014).

[71]M. Kleesiek, "A Data-Analysis and Sensitivity-Optimization Framework for the KATRIN Experiment", Ph.D. (Karlsruhe Institute for Technologie, 2014).

[72]J. Behrens, V. Hannan, and C. Weinheimer, *Personal Correspondance*, Karlsruhe, 2014.

[73]V. Hannen, J. Behrens, S. Groh, N. Steinbrink, C. Weinheimer, M. Zacher, and M. Zboril, "M3 Report - E-gun Characteristics", 1–16 (2013).

[74]J. Barrett, J. Formaggio, D. Furse, N. Oblath, T. Corona, F. Glueck, W. Kaefer, B. Leiber, and S. Mertens, "KASSIOPEIA - the KATRIN MC simulation", Verhandlungen der Deutschen Physikalischen Gesellschaft (2011).

[75]T. J. Corona, "Tools for Electromagnetic Field Simulation in the KATRIN Experiment", PhD thesis (University of North Carolina at Chapel Hill, 2009).

[76]H. Goldstein, *Classical Mechanics*, 1st (Addison-wesley, 1951), p. 399.

[77]M. Erhard, S. Bauer, A. Beglarian, T. Bergmann, J. Bonn, G. Drexlin, J. Goullon, S. Groh, F. Glück, M. Kleesiek, N. H. Smann, T. Höhn, K. Johnston, M. Kraus, J. Reich, O. Rest, K. Schlösser, M. Schupp, M. Slezák, T. Thümmler, D. Vénos, C. Weinheimer, S. Wüstling, and M. Zbořil, "High-voltage monitoring with a solenoid retarding spectrometer at the KATRIN experiment", Journal of Instrumentation **9**, P06022 (2014).

[78]D. W. Marquardt, "An Algorithm for Least-Squares Estimation of Nonlinear Parameters", http://dx.doi.org/10.1137/01 (2006).

[79]*scipy.optimize.curve_fit — SciPy v0.18.0 Reference Guide.*

[80]J. Dormand, and P. Prince, "A family of embedded Runge-Kutta formulae", Journal of Computational and Applied Mathematics **6**, 19–26 (1980).

[81]T. Ullrich, and Z. Xu, *Treatment of Errors in Efficiency Calculations*, 2007.

[82]*KATRIN ADEI*, 2016.

[83]T. E. Oliphant, "Python for Scientific Computing", Computing in Science & Engineering **9**, 10–20 (2007).

[84]K. J. Millman, and M. Aivazis, "Python for Scientists and Engineers", Computing in Science & Engineering **13**, 9–12 (2011).

[85]D. Kornbrot, and D. Kornbrot, "Point Biserial Correlation", in *Wiley statsref: statistics reference online* (John Wiley & Sons, Ltd, Chichester, UK, Apr. 2014).

[86]H. E. SOPER, A. W. YOUNG, B. M. CAVE, A. LEE, and K. PEARSON, "ON THE DISTRIBUTION OF THE CORRELATION COEFFICIENT IN SMALL SAMPLES. APPENDIX II TO THE PAPERS OF "STUDENT" AND R. A. FISHER. A COOPERATIVE STUDY", Biometrika **11**, 328–413 (1917).

[87]J. A. Formaggio, *Test Plans for the KATRIN active and passive shield*, tech. rep. (Massachusetts Institute of Technology, 2009).

[88]A. Nassalski, "Multi Pixel Photon Counters (MPPC) as an Alternative to APD in PET Applications",

[89]W. Käfer, "Sensitivity studies of the KATRIN experiment", PhD Thesis (KIT, 2012).

[90]J. Formaggio, J. Barrett, and N. Oblath, *Personal Correspondance*, 2012.